The Pennsylvania State University

The Graduate School

Department of Mechanical Engineering

DETAILED MODELING OF SOOT FORMATION AND TURBULENCE–RADIATION INTERACTIONS IN TURBULENT JET FLAMES

A Dissertation in

Mechanical Engineering

by

Ranjan S. Mehta

Submitted in Partial Fulfillment
of the Requirements
for the Degree of

Doctor of Philosophy

December 2008

The dissertation of Ranjan S. Mehta was reviewed and approved* by the following:

Michael F. Modest
Distinguished Professor of Mechanical Engineering
Thesis Co-Adviser
Co-Chair of Committee

Daniel C. Haworth
Professor of Mechanical Engineering
Thesis Co-Adviser
Co-Chair of Committee

Stephen R. Turns
Professor of Mechanical Engineering

Padma Raghavan
Professor of Computer Science and Engineering

Karen Thole
Professor of Mechanical Engineering
Head of the Department of Mechanical and Nuclear Engineering

*Signatures are on file with the Graduate School.

Abstract

Detailed radiation modeling of turbulent sooting flames faces a number of challenges. Principal among these have been been a lack of good models for predicting soot formation and effective means to capture turbulence–chemistry interactions in soot subprocesses. Uncertainties in measurement and prediction of soot properties has also been a problem. Radiative heat transfer becomes important in combustion environments due to the very high temperatures encountered and has not yet been studied in sufficient detail in the case of luminous (i.e., sooting) flames. A comprehensive approach for modeling turbulent reacting flows, including detailed chemistry, radiation and soot models with detailed closures for turbulence–chemistry interactions (TCI) and turbulence–radiation interactions (TRI) is developed in this work. A review of up-to-date literature on turbulent combustion modeling, turbulence-radiation interactions and soot modeling is given. A transported probability density function (PDF) approach is used to model turbulence–chemistry interactions and extended to include soot formation. Nongray gas and soot radiation is modeled using a photon Monte Carlo (PMC) method coupled with the PDF method. Soot formation is modeled based on the method of moments (MOM) approach with interpolative closure.

Optimal soot submodel parameters are identified based on comparison of model predictions with experimental data from various laminar premixed and (opposed) diffusion flames. These parameters (including gas-phase chemistry) are applied to turbulent

flames without further "tuning." Six turbulent jet flames with Reynolds numbers varying from 6700 to 15000, varying fuel types – pure ethylene, 90% methane-10% ethylene blend and different oxygen concentrations in the oxidizer stream from 21%O_2 (air) to 55%O_2, are simulated. The predicted soot volume fractions, temperature and radiative wall fluxes (when available) are compared with experiments. All the simulations are carried out with a single set of parameters for all models involved, without specific adjustments. Very encouraging agreement is found for most of the quantities, representing a significant step forward in modeling turbulent sooting flames. A detailed analysis of the radiation characteristics of these flames is also undertaken. It is found that emission TRI was generally important for all the flames. In the laboratory scale flames, including TRI increases the radiative loss from the flame by up to 90%. Absorption TRI is found to be unimportant in laboratory-scale flames, but becomes important in the large (industrial scale) flame that was studied numerically.

Table of Contents

List of Tables

List of Figures

Acknowledgments

I would like to express my most sincere gratitude for my advisors Dr. Michael Modest and Dr. Daniel Haworth, for all the help and support they provided during my arduous six years while working towards my Ph.D. Most importantly the trust they showed in my abilities and helped me through frequent research roadblocks, was the reason I was able to finish this program successfully. Dr. Stephen Turns also provided valuable guidance throughout my Ph.D. work and helped me understand, mainly the perspective of experimentalists and importance of interpreting the data in a consistent manner. Many thanks to Dr. Padma Raghavan who taught me the basics of parallel computing, which turned out to be very important for timely completion of the work in the long run.

Reassuring words of advice and encouragement from my mother, Neeta, and father, Satish were also crucial in continuing the effort. They instilled in me, a passion for mathematics and physics which saw me carry through the entire ordeal. My brother Sameet, also provided some invaluable advise every now and then, helping me set my priorities right every few months. Finally, I would like to thank my dear wife Chaitali for her unwavering support and tremendous patience through these tumultuous years, whose staunch support helped get through some of the very rough patches during my research.

Chapter 1

Introduction

1.1 Background

Most practical combustion devices operate in turbulent flow conditions. Even in the absence of turbulence, combustion is an inherently complex process involving the release of chemical energy of the fuel as sensible energy, which is then used for a variety of applications. The release of energy is also accompanied by radiative heat transfer (due to high temperatures) [1] and pollutant emissions including NO_x and particulate carbonaceous matter like soot [2]. Increasing regulations on emissions from combustion devices and higher efficiency considerations have resulted in a need for accurate models for all aspects of combustion devices including gas turbines, I.C. engines and industrial furnaces. From this perspective, it is necessary to develop detailed models for various physical subprocesses involved in combustion to assess their performance by comparing model predictions to experimental measurements. The presence of turbulence complicates and increases the efforts required for modeling of combustion, due to highly nonlinear two-way coupling between turbulence and combustion [3].

Developments over the last few decades in turbulence modeling, combustion modeling and computing resources have resulted in more detailed models for various phenomena involved in turbulent combustion. In order to successfully model turbulent reacting flows, the following are needed: i) A turbulence model that will predict the turbulent

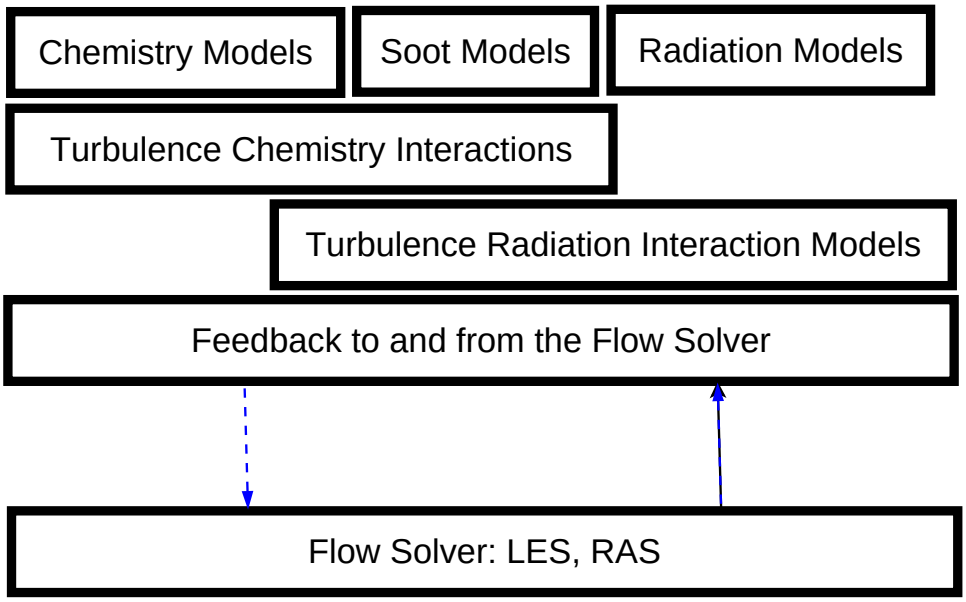

Figure. 1.1 Models needed in turbulent reacting flows.

flow field to a reasonable degree of accuracy; ii) a detailed chemistry model that accurately models the chemical reactions occuring during combustion; iii) a model of physical properties of the gas mixture including density, enthalpies, specific heats and transport coefficients; and iv) a radiation model that can account for the radiative heat losses from the reacting gas mixture at very high temperatures. Additional models to account for turbulence–chemistry interactions and turbulence–radiation interactions are also needed. The models needed for time-accurate solution of turbulent reacting flows are shown in Fig. 1.1.

Radiative emission has a fourth-power or higher dependence on temperature, making it a dominant source of heat transfer once the temperatures become very high (1000 K or higher) [1]. Radiation has been treated as independent of turbulence in most modeling studies to date; i.e., radiative calculations have been done while neglecting the fluctuations in radiative properties of the medium as well as the temperature. Experimental

results [4–6], however, show that radiative fluxes can be more than twice those predicted from numerical calculations that neglect turbulence–radiation interactions (TRI). A detailed review of TRI modeling has been given by Coelho [7]. Some researchers included TRI in their calculations using varying degrees of simplification, and have found better agreement with experimental data [8, 9]. This suggests that TRI are important when modeling turbulent reactive flows. Recently, Modest and coworkers [10–14] applied the probability density function (PDF) approach to model TRI in nonluminous flames. The most significant effect of accurate radiation modeling is on the temperature prediction; accounting for radiation can result in the peak temperature of the flame dropping by more than 150 K. This has implications for other important quantities that are highly sensitive to the predicted temperature field including unburned hydrocarbons, NO_x and soot. Modeling studies of sooting flames generally have treated radiation in a very crude and approximate manner, and very little research has been done in modeling TRI in sooting flames.

In the case of luminous (sooting) flames, the radiative emission from soot can be more than twice that from gases like CO_2 and H_2O in spite of the fact that soot volume fractions in typical flames are of the order of 1×10^{-8}–1×10^{-5}: i.e., only a few ppm. Therefore, accurate modeling of soot becomes very important in predicting radiative emission and absorption in a sooting flame. Soot modeling has been an area of active research for the past few decades [2], and has been gaining in importance due to concerns about emissions and stricter regulations. It is of interest then, to develop a comprehensive model for turbulent combustion that can account for turbulence–chemistry interactions, turbulence–radiation interactions and soot formation in a coupled and detailed manner

for canonical as well as complex configurations. A modeling study of TRI in sooting flames using detailed models is the principal aim of this work.

1.2 Objectives

The main objectives of this study are summarized as follows:

1. Develop a full three-dimensional approach for modeling turbulent reacting flows including soot formation with emphasis on turbulent nonpremixed jet flames.

2. Evaluate soot model parameters and develop recommendations for modeling soot in turbulent flames.

3. Incorporate in the turbulent reacting flow solver, a state-of-the-art soot model using a transported PDF approach to better account for turbulence–chemistry interactions in soot formation.

4. Integrate a photon Monte Carlo (PMC)-based radiative-transfer-equation (RTE) solver into the existing reacting flow solver, which enables treatment of nongray gases and soot in an effective manner, thereby allowing accurate modeling of emission and absorption TRI.

5. Study and quantify the effects of TRI on soot formation and its implications on modeling strategies.

6. Study the effects of TRI in sooting flames through variations of fuel type, Reynolds number (Re) and oxygen enhancement.

1.3 Outline of Thesis

- Chapter 2 summarizes the governing equations of reactive flows. Turbulent combustion modeling is briefly reviewed. The composition PDF method used to accurately account for turbulence–chemistry interactions is presented.

- Chapter 3 starts with a review of relevant work done on TRI modeling. This is followed by a brief review of radiative property models and the RTE solution methods used in the current study.

- Chapter 4 reviews the soot models. The method of moments is introduced, followed by a discussion of soot submodels used in the current study. Extension of the composition PDF method to include soot scalars in turbulent flame modeling is also discussed.

- Chapter 5 presents a detailed analysis of various aspects of soot submodels, along with validation of the soot models and gas-phase chemistry in laminar flames.

- In Chapter 6 a detailed validation of the soot and radiation models is undertaken. Extensive comparisons are made between model predictions and experimental data for several laboratory-scale turbulent jet flames.

- In Chapter 7 the hybrid FV/Monte Carlo method is applied to investigate radiation characteristics of the sooting flames. The importance of several individual contributions to radiation and TRI are investigated and quantified.

- Chapter 8 concludes the thesis by summarizing the important findings from this work followed by identification of research areas that may be important in the future.

Chapter 2

Turbulent Combustion Modeling

2.1 Turbulence Modeling

Most combustion processes of interest happen in a turbulent environment. Turbulent flow is generally characterized by wide fluctuations in local velocity and species concentrations. These fluctuations add to the difficulty of modeling turbulent reactive flows. A wide range of time scales and length scales are involved and the structure and description of turbulence still remains one of most challenging fundamental fields in classical physics.

Turbulence and combustion are intimately coupled. The effect of turbulence on chemical reactions takes place through large-scale motions of the turbulent flow field. This enhanced transport effectively enhances the transport rates of chemical species and heat. Turbulent fluctuations in temperature and composition substantially influence the mean chemical reaction rates, which occur at molecular scales. The effect of chemical reactions on turbulence takes place through large density changes brought about by the heat release due to combustion. Great success has been achieved in applying the governing conservation equations and detailed chemistry to laminar flames (for example [15]), indicating that the present knowledge of chemical kinetics and molecular transport processes is sufficient to make good predictions from first principles. However, turbulent

Table 2.1 Modeling approaches for turbulent flows

Approach	DNS	LES	RAS
Resolved Scales	All scales	Large scales	Only mean flow field
Required Models	None	Small subfilter scales	All Scales
Mesh Requirements	Very Fine	Fine to Medium	Coarse
Numerical Costs	Very High	Medium to High	Low
Engineering Applications	None, mainly a research tool	Gaining Importance	Widely used

reactive flows, characterized by a broad spectrum of length and time scales, are very difficult to model due to complex interactions between turbulence and other closely linked processes.

A variety of numerical methods have been developed to model and simulate turbulent combustion processes. Three categories can be distinguished: Direct Numerical Simulation (DNS), Large Eddy Simulation (LES) and Reynolds Averaged Simulation (RAS). The three approaches are summarized in Table 2.1.

DNS is the most straightforward approach to the solution of turbulent reactive flows. Theoretically, it solves the full, instantaneous, governing equations without any models or approximations: all turbulence length scales are explicitly determined and all spatial frequencies in the energy spectrum are resolved. However, DNS of the complete combustion processes is still out of reach in terms of computational resources and, accordingly, a variety of simplifications are generally introduced. These include assumptions such as constant density, low Mach number, constant molecular transport properties, infinitely fast or simplified multi-step chemistry. A major limitation of DNS is that most of the computational effort is spent on solving the smallest dissipative scales, which do

not contribute directly to the mean flow [16]. Since only the mean quantities are of interest in almost all practical applications, DNS remains a research tool generally used to calibrate models for other approaches [17, 18].

LES is based on the generally accepted notion that the scales of turbulence can be separated into two groups. The large turbulence scales are flow specific and strongly dependent on the flow geometry and Reynolds number under consideration, while the small scales tend to be more homogeneous and universal and less affected by the boundary conditions. Thus, in LES the instantaneous equations are spatially filtered so that they explicitly describe the space and time dependence of the resolved large turbulence scales, while effects of small structures are considered using subfilter-scale closure models. LES has been used extensively in many nonreacting flows and has provided reliable predictions in a variety of applications. Extension of LES to reacting flows is more problematic, because chemical reactions take place at very small scales which are not resolved directly in this approach. LES is still expensive for real engineering applications and a three-dimensional simulation is required for description of unsteady turbulent motions, even in the case of statistically one- or two-dimensional problems. LES is capable of dealing with high Reynolds numbers but requires physical models to account for the effects of subfilter-scale fluctuations, and these models determine the computation quality and accuracy [19–23].

Formally, by taking the probabilistic mean, RAS reduces the dynamic range of scales by averaging the instantaneous equations [24] (operationally, this could correspond to a time average in a statistically stationary flow, a spatial average in a statistically homogeneous flow, etc). It describes the evolution of averaged quantities and only resolves

the mean flow field. In case of a turbulent flame, RAS considers an average flame front that extends over a broad region that is much larger than the instantaneous flame thickness, so the mesh size can be much larger than in DNS or LES. RAS is extensively used in engineering simulations because it is less demanding computationally and it can be applied to complex configurations and operating conditions. RAS is used in the current study, which means that all the turbulence scales are modeled and only the mean flow properties are calculated directly.

2.2 RAS Equations

In RAS, the instantaneous balance equations for mass, momentum, chemical species and enthalpy are averaged to obtain the governing partial differential equations (PDE's) only for the averaged quantities. Two averaging methods are used: conventional Reynolds averaging is denoted by angled brackets $\langle\cdot\rangle$, and Favre averaging (a mass-weighted averaging) is denoted by the tilde $\widetilde{\cdot}$ operator. For any quantity Q, the relationship between the two averaging operators is: $\widetilde{Q} = \langle\rho Q\rangle \,/\, \langle\rho\rangle$. Fluctuations about the Favre–averaged mean are designated by double primes, i.e., $Q = \widetilde{Q} + Q''$. Averaging greatly reduces the number of degrees of freedom of the problem, but introduces unclosed terms that need to be modeled. These terms result from averaging nonlinear terms in the instantaneous governing equations. Deriving closures for these terms is the main goal of turbulent combustion modeling. The Favre averaged equations are generally preferred as they reduce the number of unclosed terms compared to conventional Reynolds averaging [3].

Using Cartesian tensor notation, the governing equations for mean quantities are expressed as follows [3]:

- Mass

$$\frac{\partial \langle\rho\rangle}{\partial t} + \frac{\partial}{\partial x_i}\left[\langle\rho\rangle \widetilde{u}_i\right] = 0. \tag{2.1}$$

- Momentum ($j = 1, 2, 3$)

$$\frac{\partial}{\partial t}\left[\langle\rho\rangle \widetilde{u}_j\right] + \frac{\partial}{\partial x_i}\left[\langle\rho\rangle \widetilde{u}_i\widetilde{u}_j\right] = -\frac{\partial}{\partial x_i}\left[\langle\rho\rangle \widetilde{u_i''u_j''}\right] + \frac{\partial \langle\tau_{ij}\rangle}{\partial x_i} - \frac{\partial \langle p\rangle}{\partial x_j} + \langle\rho g_j\rangle, \tag{2.2}$$

where $\langle\rho\rangle \widetilde{u_i''u_j''}$ is the unclosed Reynolds-stress tensor.

- Chemical species (for s species, $\alpha = 1, 2, \ldots, s$)

$$\frac{\partial \langle\rho\rangle \widetilde{Y_\alpha}}{\partial t} + \frac{\partial \langle\rho\rangle \widetilde{Y_\alpha}\widetilde{u_i}}{\partial x_i} = -\frac{\partial \langle\rho\rangle \widetilde{Y_\alpha''u_i''}}{\partial x_i} - \frac{\partial \langle J_i^\alpha\rangle}{\partial x_i} + \langle\rho\rangle \widetilde{S_\alpha}. \tag{2.3}$$

The terms $\langle\rho\rangle \widetilde{Y_\alpha''u_i''}$ represent the transport of the species due to turbulent fluctuations, and need to be modeled; this is generally done by the gradient diffusion hypothesis. The mean reaction rate $\widetilde{S_\alpha}$ also needs to be modeled due to the highly nonlinear dependence of S_α on the local composition.

- Absolute enthalpy

$$\frac{\partial \langle\rho\rangle \widetilde{h}}{\partial t} + \frac{\partial \langle\rho\rangle \widetilde{h}\widetilde{u_i}}{\partial x_i} = -\frac{\partial \langle\rho\rangle \widetilde{h''u_i''}}{\partial x_i} - \frac{\partial \left\langle J_i^h \right\rangle}{\partial x_i} + \frac{D \langle p\rangle}{Dt} + \left\langle \tau_{ij}\frac{\partial \widetilde{u_j}}{\partial x_i} \right\rangle + \langle S_{\text{radiation}}\rangle \tag{2.4}$$

where $\langle\rho\rangle\,\widetilde{h''u_i''}$ is the turbulent transport of the enthalpy and requires modeling. Because $S_{\text{radiation}}$(like S_α) is nonlinear, the mean radiative source term in the energy equation $\langle S_{\text{radiation}}\rangle$ also requires modeling (see Chapter 3)

Compared to constant-property systems, an additional set of species equations with chemical source terms representing the effects of chemical reactions is required. Chemical heat release produces high temperature in the flow field and hence variable density effects are pronounced. Radiation also becomes important due to high temperatures and the presence of radiatively participating gases such as CO_2 and H_2O and particulate matter including soot. These are a few of the complexities that compound the already difficult solutions of the Navier-Stokes equations in chemically reacting flows. Detailed discussions can be found in [3, 25–27].

2.2.1 Turbulent Closure and Diffusion Hypothesis

The turbulent fluxes $\langle\rho\rangle\,\widetilde{Y_\alpha''u_i''}$ and $\langle\rho\rangle\,\widetilde{h''u_i''}$ are generally modeled using a gradient-diffusion hypothesis; this requires information about local turbulence intensity (level of fluctuations) and is described in detail in the next section. Various strategies have been employed in estimating (modeling) the mean reaction rates $\widetilde{S_\alpha}$; this has been an area of active research over the past few decades. Similar work has been done for estimating the mean radiative source term $\langle S_{\text{radiation}}\rangle$; that is the subject of Chapter 3. All the terms in Equations 2.1–2.4 that require modeling and the models used in the current study are tabulated in Table 2.2. Each term is discussed further in the remainder of this chapter and in subsequent chapters. To determine mean quantities from these equations, models are required for the unclosed terms appearing on the right-hand sides. The Reynolds

Table 2.2 RAS models used in the current study.

Description	Unclosed Term	Model Used	Remark
Reynolds Stress Tensor	$\langle\rho\rangle \widetilde{u_i'' u_j''}$	$\mu_T \left(\frac{\partial \widetilde{u_i}}{\partial x_j} + \frac{\partial \widetilde{u_j}}{\partial x_i} - \frac{2}{3}\delta_{ij} \frac{\partial \widetilde{u_k}}{\partial x_k} \right) + \frac{2}{3} \langle\rho\rangle k \delta_{ij}$	k-ϵ Model
Turbulent Diffusion (Species)	$\langle\rho\rangle \widetilde{Y_\alpha'' u_i''}$	$-\frac{\mu_T}{Sc_{\alpha T}} \frac{\partial \widetilde{Y_\alpha}}{\partial x_i}$	Gradient diffusion with turbulent Schmidt number $Sc_{\alpha T}$
Turbulent Diffusion (Enthalpy)	$\langle\rho\rangle \widetilde{h'' u_i''}$	$-\frac{\mu_T}{Pr_{hT}} \frac{\partial \widetilde{h}}{\partial x_i}$	Gradient diffusion with turbulent Prandtl number Pr_{hT}
Chemical Source Term	$\langle\rho\rangle \widetilde{S_\alpha}$	$\int \rho(\phi) S_\alpha(\phi) \mathcal{F}(\phi) d\phi$	Composition PDF method (exact)
Radiation Source Term (Emission)	$\langle 4\pi\kappa I_b \rangle$	$\int 4\pi\kappa(\phi) I_b(\phi) \mathcal{F}(\phi) d\phi$	Composition PDF and particle based MCRT (exact)
Radiation Source Term (Absorption)	$\langle \kappa G \rangle$	$\langle \kappa G \rangle$	Particle based MCRT (δ-PDF hypothesis)

stress tensor $\langle\rho\rangle \widetilde{u_i'' u_j''}$ can be modeled in different ways. Available approaches include the classical turbulence models developed for nonreacting flows, such as the Prandtl mixing length model, one-equation models, or the two-equation k–ϵ model [28]. It is also possible to derive equations for the six components of the Reynolds stress tensor; that introduces new unclosed terms, which are modeled in the Reynolds-stress model (RSM). In the current work, a two-equation k–ϵ model is employed in which the evolution of turbulent kinetic energy $k = \widetilde{u_i'' u_i''}/2$ and its viscous dissipation rate ϵ are described by two balance equations [29]:

$$\frac{\partial}{\partial t}\left[\langle\rho\rangle k\right] + \frac{\partial}{\partial x_i}\left[\langle\rho\rangle \widetilde{u}_i k\right] = \frac{\partial}{\partial x_i}\left[\left(\mu + \frac{\mu_T}{\sigma_k}\right)\frac{\partial k}{\partial x_i}\right] + P - \langle\rho\rangle \epsilon, \tag{2.5}$$

$$\frac{\partial}{\partial t}\left[\langle\rho\rangle\,\epsilon\right]+\frac{\partial}{\partial x_i}\left[\langle\rho\rangle\,\widetilde{u}_i\epsilon\right]=\frac{\partial}{\partial x_i}\left[\left(\mu+\frac{\mu_T}{\sigma_\epsilon}\right)\frac{\partial\epsilon}{\partial x_i}\right]+\frac{\epsilon}{k}\left[C_{\epsilon1}P-C_{\epsilon2}\,\langle\rho\rangle\,\epsilon\right]. \tag{2.6}$$

Here μ is the molecular viscosity and the effective turbulent viscosity μ_T is given by

$$\mu_T=\langle\rho\rangle\,C_\mu\frac{k^2}{\epsilon}, \tag{2.7}$$

where σ_k and σ_ϵ are the respective turbulent Schmidt and numbers and C_μ is a model coefficient.

The production of turbulent kinetic energy P is given by

$$P=-\langle\rho\rangle\,\widetilde{u_i''u_j''}\frac{\partial\widetilde{u}_i}{\partial x_j} \tag{2.8}$$

The model constants employed here are the standard values: $C_\mu=0.09$, $C_{\epsilon1}=1.44$, $C_{\epsilon2}=1.92$, $\sigma_k=1.0$ and $\sigma_\epsilon=1.3$. In some cases, the coefficients are changed from the standard values to get the right jet spreading rates.

The k–ϵ model may not be sufficient for variable-density reactive flows [30]. Ongoing research is aimed at devising more general models. Although the k–ϵ model is not able to accurately predict all types of flows, it is considered adequate for the laboratory-scale jet flames that are studied in this work. Justification for use of the k-ϵ model in jet flames has been discussed in [31].

The Reynolds stresses in Eq.(2.2) can determined using a Boussinesq approximation as

$$\langle\rho\rangle\,\widetilde{u_i''u_j''}=-\mu_T\left(\frac{\partial\widetilde{u}_i}{\partial x_j}+\frac{\partial\widetilde{u}_j}{\partial x_i}-\frac{2}{3}\delta_{ij}\frac{\partial\widetilde{u_k}}{\partial x_k}\right)+\frac{2}{3}\,\langle\rho\rangle\,k\delta_{ij}. \tag{2.9}$$

Finally, turbulent fluxes of species $\left(\langle\rho\rangle\,\widetilde{Y''_\alpha u''_i}\right)$ and enthalpy $\left(\langle\rho\rangle\,\widetilde{h''u''_i}\right)$ are usually closed using a gradient diffusion hypothesis:

$$\langle\rho\rangle\,\widetilde{Y''_\alpha u''_i} = -\frac{\mu_T}{Sc_{\alpha T}}\frac{\partial\widetilde{Y_\alpha}}{\partial x_i}, \tag{2.10}$$

$$\langle\rho\rangle\,\widetilde{h''u''_i} = -\frac{\mu_T}{Pr_{hT}}\frac{\partial\widetilde{h}}{\partial x_i}, \tag{2.11}$$

where $Sc_{T\alpha}$ and Pr_T are the turbulent Schmidt number for species α and turbulent Prandtl number, respectively. The gradient-diffusion hypothesis fails in situations such as swirling flows and in cases where counter-gradient diffusion occurs [32]. However, this approach is used here for its simplicity.

At high Reynolds number, the mean molecular transport of momentum $\langle\tau_{ij}\rangle$, species $\langle J_i^\alpha\rangle$ and enthalpy $\left\langle J_i^h\right\rangle$ are generally negligible and are omitted from the averaged equations. They may be retained by simply adding a molecular diffusivity to the turbulent diffusivity, as shown in k-ϵ Eqs. (2.5) and (2.6).

Turbulent combustion models focus on the closure of the mean species chemical reaction rate $\widetilde{S_\alpha}$. The chemical source term $S_\alpha = S_\alpha(\underline{Y}, h, p)$ is a nonlinear function of chemical species mass fractions $\underline{Y}$, enthalpy h, and pressure p. Due to the strong nonlinearity, $\widetilde{S_\alpha}$ cannot be explicitly expressed in terms of any finite number of moments of $(\underline{Y}, h, p)$ even though $S_\alpha(\underline{Y}, h, p)$ may be known, in principle. Various models have been proposed and are described in detail in [3].

2.3 Composition PDF Method

During the past few decades, much research has been done in the field of turbulent combustion, mainly driven by the need for high-performance combustors as well as by emissions concerns. The use of PDF methods was originally motivated by difficulties encountered in the closure of mean chemical source terms when using moment methods [30, 33, 34]. The significant difficulties encountered in extracting the mean reaction rates arise from the fact that the terms are highly nonlinear and the fluctuations so large that the higher moments of the fluctuations cannot be neglected without introducing errors. An alternative to moment closures is the PDF closure, which was initiated by Dopazo and O'Brien [35], and later developed by Pope [24], Kollmann [36] and Dopazo [37]. A comprehensive description of the PDF methodology has been given by Pope [24]; PDF methods have established themselves as viable alternatives to conventional deterministic closure models and numerical techniques. Kollmann [36] has given an excellent review on functional formulations, PDF modeling and applications to both low and high Mach number combustion flows. Dopazo [37] has given a good review of developments in PDF methods.

In composition PDF methods, all the scalars necessary to establish the thermodynamic state of the reacting mixture (i.e., species mass fractions and enthalpy or temperature) are treated as random variables. The composition PDF then quantifies the probability of having a certain gas composition (including temperature) at each location in the computational domain. The variances and higher moments of all orders can be calculated directly from the PDF, as well as the means, which are the first moments.

The most remarkable feature of the PDF method is that one-point nonlinear sources, such as chemical reactions, can be treated exactly no matter how complicated they are. As an extension, any term in the equations, as long as it is a function of the local scalar variables only, can be treated exactly by composition PDF methods. This is in contrast to conventional moment methods, where the mean reaction rates can be determined only under special constraints of linearity or when the reactions are very fast or very slow compared to the turbulent time scales. Modest and coworkers [11, 38, 39] used this fact to accurately model the radiative emission. This is possible because the nonlinearity of radiative emission (a function of temperature only) and absorption coefficient (a function of composition variables only) can be treated exactly.

The composition PDF is not a self-contained model. The mean momentum equations must be solved for the velocity field $\underline{\widetilde{u}}$, and a turbulence model (such as k-ϵ) is required to determine both turbulent diffusivity and the mixing rate used in the stochastic mixing model [40, 41]. More advanced PDF methods have been developed to include additional independent variables into the PDF evolution equation such as the velocity–composition PDF method and the velocity–composition–dissipation joint PDF method [24, 42, 43]. In the former, a PDF transport equation for velocities and compositions is derived. The need for the gradient diffusion hypothesis is eliminated and the PDF contains all the essential information to describe a flow. However, though the velocity field is calculated, the method is still not stand-alone. Since the PDF considered is a one-point, one-time PDF, it contains no information on the time and length scales of turbulent motions. The turbulent dissipation field (turbulence timescale information) has to be provided externally. The velocity–composition–dissipation joint PDF method also

includes the turbulent dissipation rate as an independent random variable. This method now contains time and length-scale information, thus enabling it to stand alone without an external turbulence model or CFD solver (in principle). There are practical issues in determining the mean pressure field. This method is still in its early stages; the inclusion of velocities and time-scale information within the PDF adds further mathematical complexities to the modeling of the PDF equation as well as numerical difficulties. The composition PDF method, however, can be used in conjunction with well-established, robust, finite-volume codes and hence can be applied to complex configurations with relative ease [44, 45]. A comparison of various transported PDF methods is given in Table 2.3.

Table 2.3 Variants of transported PDF methods

PDF Method	External Information	Pressure Solver	Complex Config.
Composition PDF	Mean velocity, turbulent time scales	Robust algorithms	Easy
Velocity-Composition	Turbulent time scales	Relatively stable	Moderately difficult
Velocity-Composition-Frequency	None	Very complex	Extremely complex

2.3.1 Composition PDF Formulation

In a moment closure scheme it is typically assumed that only the first two moments of a quantity Q are important and that higher moments can be neglected without significant loss of accuracy. However, with the PDF method, any one-point statistic of

any quantity Q, which is only a function of the scalar field $\underline{\phi}$, can be evaluated directly from the PDF. The set of scalars considered includes all those necessary to specify the local thermodynamic state of the reacting mixture; species mass fractions and enthalpy are often an appropriate set. The quantity Q then can include the absorption coefficient κ, specific heat c_p, density ρ and any other quantities that depend only on $\underline{\phi}$. The following identities are the basis of evaluating mean quantities (both conventional and Favre averages):

$$\langle Q \rangle = \int_{-\infty}^{\infty} f(\underline{\psi}) Q(\underline{\psi}) d\underline{\psi}, \tag{2.12}$$

$$\langle \rho \rangle \, \widetilde{Q}(\underline{\phi}) = \int_{\infty}^{\infty} f(\underline{\psi}) \rho(\underline{\psi}) Q(\underline{\psi}) d\underline{\psi}, \tag{2.13}$$

where $\underline{\psi}$ represents the composition-space vector and $f(\underline{\psi})$ is defined as the probability density of the joint event $\underline{\psi} = \underline{\phi}$: i.e., $\{\psi_1 = \phi_1, \psi_2 = \phi_2, \cdots, \psi_n = \phi_n\}$. This also means that,

$$f(\underline{\psi}) d\underline{\psi} = \text{Probability} \left(\underline{\psi} \leq \underline{\phi} < \underline{\psi} + d\underline{\psi} \right). \tag{2.14}$$

Here $f(\underline{\psi})$ is known as the composition PDF and is the simplest form used in the PDF methods. It carries information only about the composition variables. It does not carry information about the velocity fields, or turbulence time and length scales. It is also a one-point PDF, in that it carries information about the probability distribution only of a single point. However, it contains complete information about the scalars at that point. The PDF thus can be used not only to estimate the mean quantities, but also for accurate determination of higher moments of these quantities. The biggest advantage is

that the moments of any quantity Q can be represented "exactly" even if Q is a highly nonlinear function of the composition vector $\underline{\phi}$.

2.3.2 PDF Equation for General Scalar

In a general turbulent reacting flow, the composition PDF is also a function of space $\underline{\mathbf{x}}$ and time t. The transport equation for the PDF $f(\underline{\psi}; \underline{\mathbf{x}}, t)$ can be derived [42] from the conservation laws of scalars, which for a composition variable $\phi_\alpha(\underline{\mathbf{x}}, t)$ is given generically by

$$\rho \frac{D\phi_\alpha}{Dt} = -\frac{\partial J_i^\alpha}{\partial x_i} + \rho S_\alpha, \tag{2.15}$$

where D/Dt is the material derivative, $\underline{J}^\alpha$ is the molecular diffusive flux of ϕ_α, and S_α is the rate of creation of ϕ_α. The transport equation for the Favre-averaged mass density function $\mathcal{F}(\underline{\psi}; \underline{\mathbf{x}}, t) = \langle \rho f \rangle = \langle \rho(\underline{\mathbf{x}}, t) \rangle \, \widetilde{f}(\underline{\psi}; \underline{\mathbf{x}}, t)$ can be obtained as follows [24, 46]:

$$\begin{aligned} &\tfrac{\partial \mathcal{F}}{\partial t} + \tfrac{\partial}{\partial x_i}[\widetilde{u}_i \mathcal{F}] + \tfrac{\partial}{\partial \psi_\alpha}[S_\alpha(\underline{\psi})\mathcal{F}] = \\ &-\tfrac{\partial}{\partial x_i}\left[\left\langle u_i'' | \underline{\psi} \right\rangle \mathcal{F}\right] + \tfrac{\partial}{\partial \psi_\alpha}\left[\left\langle \tfrac{1}{\rho}\tfrac{\partial J_i^\alpha}{\partial x_i} | \underline{\psi} \right\rangle \mathcal{F}\right] - \tfrac{\partial}{\partial \psi_\alpha}[S_{\text{nonlocal}}(\underline{\psi})\mathcal{F}] \end{aligned} \tag{2.16}$$

In Eq.(2.16), summation is implied over repeated indices i and α within the terms and i and α represent physical and composition space, respectively. The notation $\langle A|B \rangle$ denotes the conditional probability of event A given that B occurs. The first two terms in Eq.(2.16) are transport of the mass density function $\mathcal{F}$ when following the Favre averaged mean flow. The third term is the divergence of the flux of probability in the composition space due to source terms that depend only on the local compostion (e.g., chemical reaction and radiative emission). This equation also shows that no matter

how nonlinear these sources are, they can be represented exactly. The third term on the right-hand side are source terms that are not function of the local composition only (e.g., radiative absorption). These terms need modeling.

2.3.3 Modeling Turbulent Diffusion

The terms on the right-hand side of Eq.(2.16) must be modeled. The first term on the right-hand side represents transport of the mass density function $\mathcal{F}(\underline{\psi}; \underline{\mathbf{x}}, t)$ in physical space due to turbulent velocity fluctuations. Since the joint composition PDF contains no information about the velocity field, the conditional expectation of $\left\langle u_i^{''} | \underline{\psi} \right\rangle$ needs to be modeled. It is generally modeled based on a gradient-diffusion model with information supplied for the turbulent flow field by a flow solver as [24],

$$\left\langle u_i^{''} | \underline{\psi} \right\rangle \mathcal{F} \simeq \Gamma_t \frac{\partial \mathcal{F}}{\partial x_i}. \tag{2.17}$$

The turbulent diffusivity Γ_t is estimated by an ad-hoc relationship, which is derived from dimensional analysis and other considerations [24]. It is expressed as

$$\Gamma_t = C_\mu \langle \rho \rangle \sigma_\phi^{-1} k^2 / \epsilon = \frac{\mu_T}{\sigma_\phi} \tag{2.18}$$

where, μ_T and σ_ϕ are, respectively the modeled turbulent diffusivity as given in Eq.(2.7) in the standard two-equation k-ϵ model and a turbulent Schmidt or Prandtl number.

2.3.4 Modeling Molecular Mixing

The second term on the right-hand-side Eq.(2.16) represents transport in the scalar (composition) space due to molecular transport. This modeled term becomes very important when dealing with reactive flows, and the closure problem shifts to modeling molecular mixing accurately. Various models have been proposed including Interaction by Exchange with the Mean (IEM) [35], modified Curl model [47] and the Euclidean Minimum Spanning Tree (EMST) [48]. It has been shown that different mixing models achieve different levels of extinction in nonpremixed flames when applied in RAS/PDF formulations [49]. A comparison of most commonly used mixing models and their key features/limitations is shown in Table. 2.4.

Table 2.4 Mixing models for composition PDF methods

Mixing Model	Reference	Key Feature	Key Limitation
IEM	Dopazo [35]	Easy to implement	Unable to predict extinction
Modified Curl Model	Janicka et al. [47]	Better performance than IEM	Problems when there is moderate extinction
EMST	Subramaniam and Pope [48]	Local in composition space	Computationally much more expensive than IEM or Curl models

The IEM model, for example, does not relax the PDF to Gaussian in homogeneous isotropic turbulence, in contrast to experimental evidence. An alternative to IEM is the Coalescence-Dispersion (CD) model also known as the particle interaction model or stochastic mixing model. In this model, two fluid particles with distinct composition first "coalesce" and then "disperse" with identical compositions. Operationally, the two

particles p and q selected at random in a control volume, and mix with a specified probability p_{mix} during a time-step Δt. After mixing, the new scalar values on the two particles are the mass-weighted average of the scalar values before mixing. The probability of a pair of particles mixing is given by

$$p_{\text{mix}} = C_\phi N \frac{\Delta t}{\tau}, \tag{2.19}$$

where $\tau = k/\epsilon$ is the turbulent timescale, C_ϕ is the model constant and, N is the number of particles present in the control volume under consideration. A drawback of the CD model is that the new scalar values are limited to a countable number of values. This can be overcome by using a modified CD model proposed by Janicka et al. [47] so that the final scalar values can take any value between the bounds for that scalar. In the case of modified Curl's model, the composition of the coalsced particles p,q is changed according to

$$\phi_p^{new} = \phi_p + \frac{1}{2} a \left(\phi_q - \phi_p \right) \tag{2.20}$$

$$\phi_q^{new} = \phi_q + \frac{1}{2} a \left(\phi_p - \phi_p \right) \tag{2.21}$$

where ϕ_p is the composition of particle p, and a is a uniform random number such that $\phi \in (0, 1)$. In case of the CD model, $a = 1$ is used.

In the EMST model proposed by Subramaniam and Pope [48], the change in particle composition is determined by particle interactions along the edges of Euclidean minimum spanning trees constructed on ensembles of particles in the composition space.

Research for an improved mixing model is ongoing [50]. In the current work, variants of CD models and the EMST model have been used.

The final modeled transport equation for the mass density function $\mathcal{F}$ can be written as

$$\frac{\partial \mathcal{F}}{\partial t} + \frac{\partial}{\partial x_i}\left[u_i'' \mathcal{F}\right] + \frac{\partial}{\partial \psi_\alpha}\left[S_{\alpha,\text{react}}(\underline{\psi})\mathcal{F}\right] + \delta_{\alpha,s}\frac{\partial}{\partial \psi_\alpha}\left[S_{\text{rad,emission}}\mathcal{F}\right] = \frac{\partial}{\partial x_i}\left[\Gamma_t \frac{\partial \mathcal{F}}{\partial x_i}\right] + F_{\text{mix}} + \delta_{\alpha,s}\frac{\partial}{\partial \psi_\alpha}\left[S_{\text{rad,absorption}}|\psi\right] \tag{2.22}$$

where F_{mix} is the flux (in composition space) due to molecular mixing and is obtained from a mixing model. This equation can be solved using Lagrangian particle Monte Carlo methods as discussed in Section 2.3.5.

2.3.5 Solution Algorithm

In principle, the PDF transport equations Eqs. (2.16) and (2.22) can be solved by traditional finite-volume and finite-element methods. This approach was used by Janicka et al. [47] for a jet diffusion flame. In general, however, the PDF is a function of a large number of independent variables, which makes it prohibitively expensive to use standard finite volume methods (FVM) and finite element methods (FEM) to solve Eq.(2.22). Monte Carlo approaches to the solution of the PDF equation have therefore been developed [24]. The basic idea is to represent the PDF by a sufficiently large number of notional fluid particles. The mean quantities at any point in the domain are then calculated as an ensemble average over the particles in a sufficiently small neighborhood. By its nature, the particle tracking method is grid-free; however, in

general, a grid is required to extract the statistics of the scalars at discrete locations. The algorithm presented here was developed by Pope and coworkers [24, 51, 52] and by Subramaniam and Haworth [53]. An algorithm developed by Zhang and Haworth [44] to ensure consistency between the values obtained by a FV solution and Monte Carlo solution is also implemented. All use a coupled flow solver to provide information about the velocity field. The numerical methods have been analyzed for different types of errors by Pope et al. [54, 55]. The overall algorithm used in the current study is shown schematically (flow chart) in Fig. 2.3.5

The idea is to represent the PDF by a sufficiently large number of particles. Each particle can be interpreted as an independent realization of the flow which evolves in time according to a set of stochastic differential equations. Pope [56] has shown that there is a one-to-one correspondence between the modeled PDF equation, particle evolution equations and the modeled Eulerian governing equations for the field means. Thus, for a modeled mass-density function, Eq.(2.22), the corresponding particle locations $\underline{\mathbf{x}}$ and compositions $\underline{\phi}$ are governed by the following stochastic equations:

$$d\underline{\mathbf{x}}^*(t) = \left[\underline{\widetilde{u}} + \nabla\Gamma_T / \langle\rho\rangle\right]_{\underline{\mathbf{x}}^*(t)} dt + \left[2\Gamma_T / \langle\rho\rangle\right]^{1/2}_{\underline{\mathbf{x}}^*(t)} d\underline{W} \tag{2.23}$$

$$d\phi^*_\alpha(t) = S^*_{\alpha,\text{reaction}} dt + F^*_{\text{mix}} + \delta_{\alpha s} \frac{S^*_{\text{radiation}}}{\rho^*} dt, \alpha = 1, \ldots, s \tag{2.24}$$

where F^*_{mix} is the mixing model term, and $S^*_{\text{radiation}}$ is the radiative heat source calculated for the particle. In these equations, the number of species ranges from $\alpha = 1, \ldots, s-1$ and the s^{th} scalar is the enthalpy, so that the radiation source term only affects the s^{th}

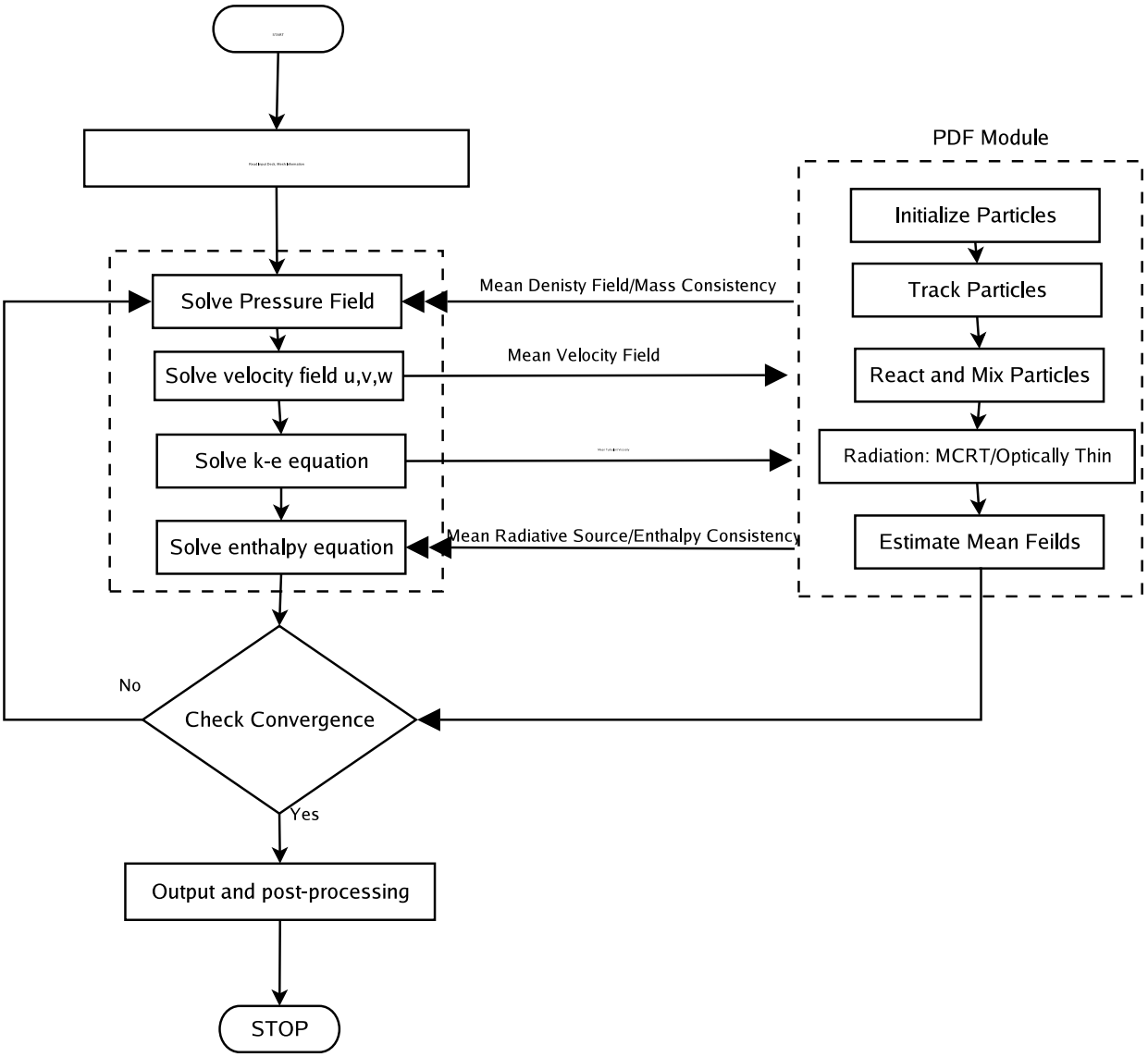

Figure. 2.1 Numerical algorithm for composition PDF method

scalar and does not contribute in the transport of other scalars directly. Variables with an asterisk refer to the values of a Lagrangian particle, $\underline{W}$ is an isotropic vector Wiener process and Γ_T is the turbulent diffusivity given in Eq.(2.18). The equation for the mean of any quantity $Q = Q(\underline{\phi})$ can be obtained by multiplying the PDF transport Eq.(2.22) by $Q(\underline{\psi})$, followed by an integration over the entire $\underline{\psi}$ space.

The time-step for the particle equations needs to be chosen carefully. It should not be larger than the local turbulent time-scales, in order to avoid false diffusion. Another criterion is that that the particle displacement in one time-step should not be too large compared to the cell size. Otherwise, the particles may traverse many cells in a time-step and rapid changes in scalar fields may not be captured. Therefore, the time-step is generally chosen to satisfy an extended Courant-Fredrichs-Levy (CFL) condition [55], which dictates the allowable time-step in a cell to be,

$$\Delta t_i = \min \left\{ \frac{k}{\epsilon}, N_{\text{cfl}} \frac{\Delta x}{\widetilde{u}}, N_{\text{cfl}} \frac{\Delta y}{\widetilde{v}}, N_{\text{cfl}} \frac{\Delta z}{\widetilde{w}} \right\}_i , \quad i = 1, \ldots, n, \tag{2.25}$$

where, $\widetilde{u}, \widetilde{v}, \widetilde{w}$ are mean velocity components in x, y, z directions, n is the total number of cells, $\Delta x, \Delta y, \Delta z$ are the maximum span of cell i in the corresponding directions, and N_{cfl} is the particle CFL number (usually taken to be below unity). The time step in the simulation is chosen to be the minimum amongst all the cells, i.e.,

$$\Delta t = \min \left\{ \Delta t_i, \quad i = 1, \ldots, n \right\}. \tag{2.26}$$

2.3.5.1 Particle Tracking Algorithm

Following Subramaniam and Haworth [53], for a particle j in cell i, the minimum time to intersect a face of cell i, $t^j_{min,i}$, is determined based on the velocity and location of particle j in cell i. At the end of the time-step, the particle stays in cell i if $t^j_{min,i} > \Delta t$. If $t^j_{min,i} < \Delta t$, the particle is moved to the face intersection point, its cell pointer is updated and its time-step is decremented by $t^j_{min,i}$. Tracking continues until all the particles have zero time remaining. Particles in a cell are cloned, if the number of particles in a cell drop below a prescribed minimum. In cloning, a parent particle is split into two particles of half mass, but each with same properties as the parent. If the number of particles in a cell exceeds a prescribed maximum, particles with small mass are selectively annihilated and the mass associated with these particles is distributed among the remaining particles in the cell. This algorithm results in comparable statistical error levels for all cells, and results in an efficiency improvement. A similar algorithm with additional time-step splitting was implemented by Li and Modest [57]. The particle tracking scheme is suitable for three-dimensional unstructured stationary or deforming meshes with relatively large Courant numbers (> 10) and large variations in the finite-volume element size (up to factor of 10^6 variation in the element volumes). Particles are tracked from element to element using trilinear basis functions. Details can be found in [44, 58]. The PDF is then obtained approximately as the histogram of the particles' properties in sufficiently small neighborhoods in physical space, and the means of the flow field are deduced statistically from the properties of these particles.

2.3.5.2 Mean Field Estimation

An important issue in PDF/Monte-Carlo methods is the estimation of means. Estimates of mean quantities from particle values are needed to evaluate Favre means, which also appear as coefficients in the particle evolution equations. Various approaches have been used to estimate the mean fields from a notional particle field [58]. Currently, field means are estimated by means of a particle-cloud-in-cell method so that the Favre average of a quantity Q in a cell c is given by

$$\widetilde{Q}_c = \frac{\sum_{p \in c} m_p Q_p}{\sum_{p \in c} m_p} \tag{2.27}$$

where, summation is over all the particles in a finite volume cell c, m_p is the mass of particle p and Q_p is the quantity carried by particle p.

For statistically steady flows, the simulations are run in a transient manner until the mean quantities become independent of time. Time averaged quantities are estimated as,

$$\widetilde{Q_{c,n}} = x\widetilde{Q_{c,n,p}} + (1-x)\widetilde{Q_{c,n-1}}, \tag{2.28}$$

where $\widetilde{Q_{c,n,p}}$ is the ensemble average in cell c at time-step n, $\widetilde{Q_{c,n}}$ is the time-averaged quantity in cell c at time-step n and $0 \leq x \leq 1$ is a blending factor. This method was found to give smooth mean scalar fields which evolve towards the correct value as the simulation times are increased. The advantage of such a scheme is that no memory is required to store time histories, while a disadvantage is that different time steps are not weighted equally. However, upon reaching a statistically converged state, the

results would be independent of the value of x. Initially $x = 0.99$ is used so that the mean quantities can develop rapidly. Thereafter, $x = 0.999$ is used, and appears to be sufficient for obtaining steady-state solutions.

2.4 Summary

The governing equations for turbulent reacting flows and the models used in the current study have been presented in this chapter. The main features of the composition PDF method along with its formulation and solution algorithm have been laid out. The composition PDF method allows exact closure of highly nonlinear source terms appearing in species equations due to chemical reactions, and the emission source term appearing in the enthalpy equation due to radiation. A Lagrangian particle Monte Carlo method is used to solve the transported PDF equations, as it can handle high dimensionality of the problem with relative ease. It is also noted that the composition PDF method is not self-contained and needs an external turbulence model and mean velocity fields to be used in the stochastic differential equations. However, an accurate closure for chemistry allows the method to handle any arbitrarily complex chemistry with relative ease.

Chapter 3

Radiation Modeling and TRI

3.1 Radiative Transfer Equation

For an absorbing–emitting, but nonscattering medium, the instantaneous radiative energy balance for a pencil of radiative energy propagating in the direction $\hat{s}$ is expressed as [1]

$$(\hat{s} \cdot \nabla) I_\eta = \kappa_\eta \left(I_{b\eta} - I_\eta \right), \tag{3.1}$$

where κ_η is the spectral absorption coefficient (a function of pressure p, temperature T and species mass fractions $\underline{Y}$), $I_{b\eta}$ is the spectral blackbody intensity (or Planck function) and I_η is the spectral intensity. The first term on the right-hand side is augmentation due to emission and the second term is attenuation due to absorption.

Radiation is coupled to the overall energy equation through a radiative source term, Eq.(2.4). This term comprises the net radiative loss (or gain) in a control volume and is the difference between the total energy emitted by the control volume and total energy absorbed by the control volume. It is a spectrally integrated quantity ($S_{\text{radiation}}$) given by [1]

$$S_{\text{radiation}} = -\nabla \cdot \underline{q}^R = \int_0^\infty \kappa_\eta \left(\int_{4\pi} I_\eta d\Omega - 4\pi I_{b\eta} \right) d\eta, \tag{3.2}$$

where $\underline{q}^R$ is the radiative flux. The subscript η denotes spectral dependence and Ω is the solid angle.

3.2 Turbulence-Radiation Interactions

In order to incorporate radiation in RAS-based turbulent combustion calculations, Eq.(3.1) needs to be averaged, resulting in

$$(\hat{s}\cdot\nabla)\left\langle I_\eta\right\rangle = \left\langle \kappa_\eta I_{b\eta}\right\rangle - \left\langle \kappa_\eta I_\eta\right\rangle . \tag{3.3}$$

Solving the mean continuity, momentum and energy equations (2.1)–(2.4) yields the Favre-averaged enthalpy and species mass fractions $\tilde{h}$ and $\underline{\tilde{Y}}$. However, the absorption coefficient κ_η depends nonlinearly on both species concentrations and the temperature so that, in general,

$$\left\langle \kappa_\eta I_{b\eta}\right\rangle = \left\langle \kappa_\eta\right\rangle \left\langle I_{b\eta}\right\rangle + \left\langle \kappa'_\eta I'_{b\eta}\right\rangle \neq \kappa_\eta(\underline{\tilde{Y}},\tilde{h})\left\langle I_{b\eta}\right\rangle , \tag{3.4}$$

$$\left\langle I_{b\eta}\right\rangle \neq I_{b\eta}(\langle T\rangle), \tag{3.5}$$

and

$$\left\langle \kappa_\eta I_\eta\right\rangle = \left\langle \kappa_\eta\right\rangle \left\langle I_\eta\right\rangle + \left\langle \kappa'_\eta I'_\eta\right\rangle \neq \kappa_\eta(\underline{\tilde{Y}},\tilde{h})\left\langle I_\eta\right\rangle . \tag{3.6}$$

The essence of TRI modeling is to accurately estimate the left-hand sides of Eqs. (3.4) and (3.6). In Eqs. (3.4) and (3.6), $\left\langle \kappa'_\eta I'_\eta\right\rangle$ represents the correlation between the fluctuating absorption coefficient and spectral incident intensity, and $\left\langle \kappa'_\eta I'_{b\eta}\right\rangle$ represents a correlation between the fluctuating absorption coefficient and the local blackbody intensity.

Following Li [46], these two correlations are loosely defined as absorption coefficient–incident intensity correlation and absorption coefficient–black body intensity (Planck function) correlation, respectively.

3.2.1 Optically Thin Fluctuation Assumption

The absorption coefficient–intensity correlation has been generally neglected by much of the research community, partly due to the difficulties in its modeling, and partly due to the fact that it is rarely of importance. The most commonly used justification in the literature was provided by Kabashnikov and Myasinkova [59]. They suggested that, if the mean free path for radiation is much larger than the turbulent length scale, then the fluctuations of the local incident radiative intensity would only be weakly correlated with those of the local absorption coefficient. Under these conditions one can assume

$$\left\langle \kappa_\eta' I_\eta' \right\rangle \simeq 0, \tag{3.7}$$

so that,

$$\left\langle \kappa_\eta I_\eta \right\rangle = \left\langle \kappa_\eta \right\rangle \left\langle I_\eta \right\rangle, \tag{3.8}$$

where $\left\langle \kappa_\eta \right\rangle$ is the mean absorption coefficient self-correlation. Kabashnikov and Myasinkova provided several conditions for the validity of this thin-eddy approximation [59]. In general, however, the thin-eddy approximation rests on the assumption that the optical thickness of the turbulent eddies is small:

$$\kappa_\eta l \ll 1, \tag{3.9}$$

where l is the turbulent eddy length scale. The validity of this assumption will depend on the eddy-size distribution and the radiative properties of the absorbing gases. In a numerical simulation of a combustion chamber, Hartick et al. [60] showed that the thin-eddy approximation may not be valid over some highly absorbing spectral regions. This observation suggests that the optically-thin-fluctuation approximation (OTFA) may result in miscalculation of the re-absorption of radiative energy when the medium has fluctuating radiative properties. As mentioned by Li [46], the fact that the radiative intensity I_η does not depend solely on the local composition makes this a very challenging and difficult problem. This is also the main reason why almost all researchers accept OTFA as reasonable and use it in their analysis. However, the degree of approximation introduced is still unknown. Modest and Mehta [13] obtained expressions for absorption TRI using a diffusion approximation, which is valid in optically very thick parts of the spectrum. In this work it was assumed that the absorption coefficient depended only on temperature (i.e., independent of species concentrations). It was shown that absorption TRI may not be negligible over certain parts of the spectrum, although the overall contribution to radiative transfer may not be significant [61].

In the case of turbulent sooting flames, the absorption coefficient is larger (than in nonsooting flames) over a significant part of the spectrum and, hence, it is expected that there maybe significant absorption TRI. This will be investigated in the current study.

3.2.2 TRI Modeling Efforts

In recent years much progress has been made in the modeling of TRI. An exhaustive review of the literature up to 2006 has been done by Coehlo [7]. The most relevant work from that review is summarized here for completeness; other work since that time is then reviewed and the salient features of each approach, along with approximations and limitations, are identified. Some of the most relevant works are summarized in Table 3.1. Review of numerical simulation of TRI in an uncoupled manner (where the radiative heat source does not feed back to the flow-field) or nonreacting flows is not included, as the focus is mainly on coupled radiation calculations. The interested reader is referred to [7].

Radiative calculations accounting for TRI and their effects feeding back to the flow field were first carried out by Song and Viskanta [62], who investigated combustion in a two-dimensional furnace. Simplifying assumptions were made to simulate scalar fluctuations including those of gaseous radiative properties by using an assumed joint Gaussian PDF, and the OTFA was invoked. A fully coupled system of equations including reactions and radiation was solved. The results showed that radiative fluxes increased by up to 80% with consideration of TRI when the flame occupied a large portion of the combustion chamber. Hartick et al. [60] extended this approach to an enclosed diffusion flame with assumed PDF shapes for the mixture fraction and chemical heat release rate. They concluded that turbulence–radiation interactions had only a small influence on the spatial distribution of temperature and other scalar fields. However, the drop

in temperatures caused significant effects on local nitrogen oxide production and emissions. Krebs et al. [63] showed that scalar fluctuations increased radiative emission at short wavelengths, and that concentration fluctuations tended to make the medium more transparent (i.e., more optically thin).

Most of the studies above treated turbulence–radiation interactions in a fairly approximate fashion, either by using some correlations for turbulent fluctuations or by assuming a shape for the PDF. Mazumder and Modest [64, 65] calculated the actual PDF by employing the joint velocity-composition PDF for the simulation of a bluff-body stabilized methane-air flame. When invoking the OTFA (i.e., neglecting absorption TRI), only emission TRI ($\langle \kappa_\eta I_{b\eta} \rangle$) needs to be determined and can be accurately found using transported PDF methods with no further approximations. Similarly, Li and Modest [57, 66–68] used a hybrid finite-volume/composition PDF method to study TRI in methane-air jet diffusion flames. They undertook a detailed investigation of the effect of parameters, including the Reynolds number, optical thickness, and Damköhler number on TRI. The OTFA was again invoked so that only emission TRI needed to be rigorously considered. Full-spectrum correlated k-distributions were used for spectral property variations and the simple P_1-approximation was employed as the RTE solver. Raman et al. [69] employed a similar hybrid finite volume/PDF Monte Carlo method to study partially premixed methane/air flames and obtained very good agreement with experiment. Emission TRI was accurately modeled, while the OTFA was invoked to neglect absorption TRI.

Absorption TRI is the correlation between fluctuations in the (local) absorption coefficient and the incoming intensity, which may be shaped by the entire domain (non-local). In general, the joint PDF formulation carries only one-point statistics and, hence, does not contain information about length-scales or gradients [61], and cannot obtain closure for the absorption TRI. One of the most rigorous attempts to take the effects of absorption TRI ($\langle \kappa_\eta I_\eta \rangle$) into account was considered by Tessé et al. [70, 71] in their modeling of radiative transfer in a turbulent, sooty, ethylene/air jet flame. The flame was simulated using the composition PDF method of Zamuner and Dupoirieux [72]. The converged mean fields were then used as a starting point for radiation calculations. Ad-hoc turbulent structures were superimposed randomly in the domain to simulate snapshots of turbulent fields. A Monte Carlo ray tracing scheme was carried out to calculate the radiative source term for each cell, based on the joint-PDFs of turbulent structures in the ray paths. With TRI the radiative heat loss was found to be about 30% of the chemical heat release, and the radiative energy absorbed in the flame was also comparable to the emitted energy, showing that the optically thin approximation was clearly invalid. However, there was strong sensitivity to the parameters that modeled the ad-hoc turbulent structures.

Very recently Wang and Modest [14, 73, 74] developed and tested several Monte Carlo emission and absorption schemes for media represented by discrete particles. This precludes the need of assuming turbulent structures, in the context of composition PDF methods involving Lagrangian particle tracking. It also allows accounting for absorption TRI. This method is used in the current work and the details are discussed in Section 3.5.

Table 3.1: TRI Modeling Efforts

RTE Solver	Reference	Combustion Geometry	Fuel, Soot	Radiative Properties, TRI
Optically Thin	Song and Viskanta [8]	2D Furnace	Natural Gas, Non-sooting	Correlated-k, OTFA
Optically Thin	Hartick et al. [60]	Confined diffusion flame	CH_4 , Non-sooting	Correlated-k, OTFA
P_1	Mazumder and Modest [64, 65]	Bluff body stabilized	CH_4 , Non-sooting	Wide-band correlated-k, OTFA
P_1	Li and Modest [57]	Piloted jet flame	CH_4 , Non-sooting	FSK, OTFA
Optically thin	Raman et al. [69]	Partially premixed jet	CH_4 , Non-sooting	OTFA
PMC	Tessè et al. [75]	Nonpiloted jet	C_2H_4 , Sooting	Correlated k, Ad-hoc turbulent structures
PMC	Wang and Modest [14]	Piloted jet	CH_4 , Non-sooting	LBL, Exact emission TRI, modeled absorption TRI.

The effects of TRI may be different for sooting and nonsooting flames. In the case of nonsooting flames, it has been shown that TRI enhances radiative emission and radiative loss, and causes a decrease in the flame temperature. There have been few studies for sooting flames and the effects of TRI are difficult to anticipate [7]. Here TRI will depend on correlation between temperature fluctuations and soot concentration fluctuations, which may either be positive or negative, depending on the values of temperature, soot concentration, wavelength and turbulent intensity. This investigation is one of the aims of the current work.

3.3 Spectral Modeling

Spectral models are an important aspect of radiation (and TRI) modeling. The absorption coefficient of important combustion gases like CO_2 , H_2O and CO is a highly non-regular function of wavenumber (or wavelength), varying by many orders of magnitude even across small spectral intervals [1]. Hence, to resolve the spectral absorption coefficient accurately, one has to resort to so-called "line-by-line" (LBL) calculations [76]. Line-by-line absorption coefficient data can be obtained from spectroscopic databases for various gases, which are created by combining results from complex quantum mechanical calculations and experimental observations. Various databases have been developed over the years, including [77–79]. However, from a CFD modeling point-of-view, this implies that the RTE needs to be solved for a huge number of spectral locations, and results must then be integrated over the entire spectrum according to Eq.(3.2). This requires solving the RTE about one million times for each time-step making radiation calculations computationally prohibitive in any realistic CFD model.

Most combustion models today include fairly primitive radiative property models to make radiation calculations in a reasonable amount of time. Radiative property models in essence try to achieve line-by-line accuracy for a fraction of LBL cost [1]. Some of the models are highly inaccurate in that regard, while others are successful. The simplest model of this form is the so-called gray-gas model which assumes no spectral variation of the absorption coefficient; it instead uses the Planck-mean absorption coefficient of the gases (and soot) defined as [1],

$$k_{P,\alpha}(T) = \frac{\pi \int \kappa_\eta I_{b\eta} d\eta}{\sigma T^4}. \tag{3.10}$$

where $k_{P,\alpha}(T)$ is the Planck-mean absorption coefficient, η is the wavenumber and σ is the Stefan-Boltzmann constant, α is the index for each participating medium in the mixture.

Such a model was used by Song and Viskanta [8] to analyze TRI in a 2D furnace. The box model is a slight improvement over the gray gas model, with constant absorption coefficients in certain spectral ranges of specific gases; for example, [64] uses a box model for CO_2 and H_2O . Then there is the weighted-sum-of-gray-gases (WSGG) model, where the nongray properties are weighted according to their importance over the spectrum, and the spectral effects of each gas are broken down as a sum of gray gases with different absorption coefficients [80, 81]. More sophisticated spectral models include the statistical narrow band (SNB) model [76] and the narrow-band correlated-k (CK) models [82]. However, when the medium is inhomogeneous in both temperature and composition, even these methods suffer from limitations and inaccuracies [1].

3.3.1 k-g Distributions

An inspection of the spectral absorption coefficients of gases shows that the oscialltory absorption coefficient has the same value k at many different wavenumbers even in a very small portion of the spectrum (narrow band), across which black-body intensity and other radiative properties remain essential constant. This fact has been used to reorder the absorption coefficient across the narrow bands into a montonic distribution normalized against a nondimensional wavenumber g, which is much more efficiently integrated across the spectrum. This is known as the narrow-band k-distribution approach. An example of such absorption coefficient variation in a narrow spectral band of CO_2 is shown in Fig. 3.1a and the corresponding narrow-band k-distribution is shown in Fig. 3.1b.

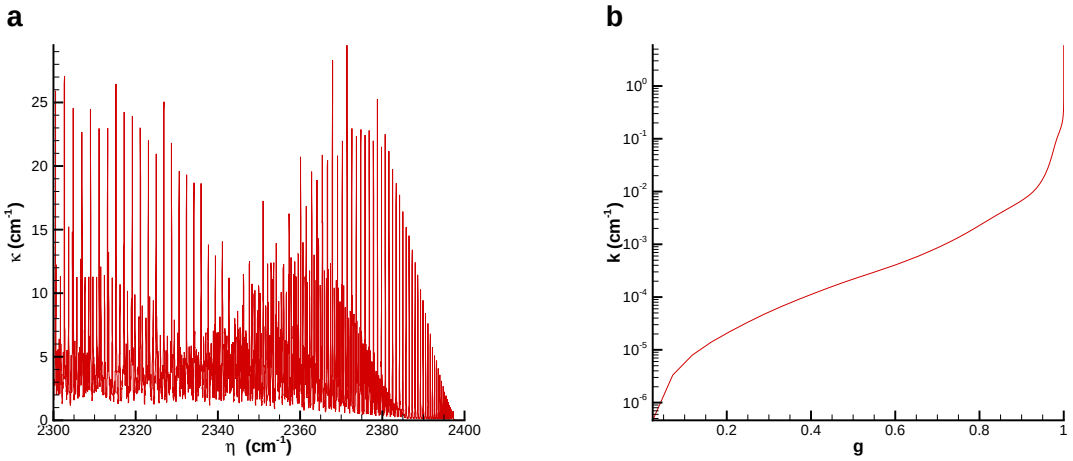

Figure. 3.1 a) Spectral absorption coefficient for CO_2 at 1000K; b)Corresponding k-distribution

The full-spectrum k-distribution (FSK) methods developed by Modest and coworkers [83–87] over the past few years are the most advanced spectral models for molecular

gases. The basic idea is to reorder the absorption coefficient across the entire spectrum by generating the cumulative distribution function of the absorption coefficient weighted by the Planck function [84]. This results in a smooth monotonic absorption coefficient as a function of a nondimensional wavenumber g. Li [46] reported that, using the FSK method, a mere nine quadrature points were sufficient to make accurate radiative calculations for methane–air diffusion flames, when only water vapor and carbon dioxide are considered as the radiating gases in the mixture. Thus very accurate radiative calculations are possible with CPU-efficiency increased by a factor of almost one hundred thousand (10^5) compared to LBL. Very recently, the method has been extended into a multi-group, multi-scale formulation by Pal and Modest [87], including provisions for handling soot radiation. This method is shown to be accurate even in highly inhomogeneous conditions and situations, where the FSK method does not perform satisfactorily. Application of this method to CFD problems, using conventional RTE solution methods, is a topic of ongoing research. Wang and Modest [88] developed a high-accuracy, compact, narrow-band database for on-the-fly assembly of FSK distributions to be used in CFD simulations. This method allows very accurate radiative calculations with a relatively small increase in CPU times.

3.4 RTE Solution Methods

The simplest approximation for the radiative source term is the so-called optically thin assumption, in which local re-absorption of radiation is neglected, and spectrally integrated absorption coefficients can be used for gases and soot, resulting in a simplified

expression for the radiative source term given by

$$S_{\text{radiation}} = \left(\sum_{i=1}^{i=Ngas} k_{p,i} P_i + k_{p,soot} \right) 4\sigma \left(T^4 - T_{surr}^4 \right), \tag{3.11}$$

where $k_{p,i}$ is the pressure-based Planck-mean absorption coefficient of radiating species such as H_2O and CO_2, in $m^{-1}bar^{-1}$, P_i is the partial pressure of species i, and $k_{p,soot}$ is the Planck-mean absorption coefficient of soot. This analysis only requires gray properties and thus does not depend on the wavelength. Obviously, such approximation is inaccurate in spectra with significant reabsorption. However, it is widely used due to its simplicity. In the current work, we use Planck-mean, ($k_{p,soot}$), and $\kappa_{soot,\eta}$ spectral values based on Rayleigh theory [1], assuming small particles, and a complex index of refraction given by Chang and Charalampopulous [89].

For a more accurate evaluation of the radiative source term, it is necessary to solve the nongray RTE, which has been done with various methods. The most widely used RTE solution methods are the Discrete Ordinates Method (DOM) [90, 91] and the spherical harmonics method (usually its first order approximation, P_1). In DOM, the directional variation of the intensity is resolved by a set of discrete directions spanning the solid angle 4π. In modern versions the discretization is based on finite volumes (which makes the formulation conservative), but finite differencing can also be used. The method has problems converging in optically thick situations, and needs iterative solution method if scattering and/or wall reflection is involved [1]. In addition, the discretized directions can result in the so-called ray-effect where the computed radiative intensity is restricted to specific ordinates and cannot approximate the entire solid angle.

This results in incorrect distribution of the radiative intensity when travelling over large distances. In the spherical harmonics [46, 65] method the radiative intensity is expanded into orthogonal spherical harmonics, resulting in a simple PDE formulation for the RTE. Generally, only the first harmonic is considered (hence the acronym P_1). However, the P_1-approximation is only accurate in situations where the radiative intensity is nearly isotropic and suffers from inaccuracies otherwise [92]. For example, Wang [92] showed that the P_1-method fails to yield correct results in a turbulent sooting propane-air flame due to the highly nonisotropic radiative intensity. Recent progress has been made to include higher harmonics into the formulation and hence improve its applicability to highly nonisotropic situations [93–95]. However, application of this formulation is complicated due to highly complex boundary conditions involving gradients in the transverse direction along with the normal. Applying higher order spherical harmonics to realistic combustion problems is not a focus of this work and is a topic of ongoing research.

Finally, there is the photon Monte Carlo (PMC) method to solve the RTE [1]. The PMC method can handle highly complex scenarios, including nongray effects, and arbitary geometries and radiative property inhomogeneity and solves the RTE in a statistical manner. In the current work, a recently developed PMC algorithm [74] has been used to solve for the radiative source terms and, is reviewed in detail.

3.5 Photon Monte Carlo Method

The PMC method directly simulates the basic processes involved in radiative transfer, i.e., emission, absorption, scattering and reflection, by tracing representative

photon bundles. Each photon bundle represents a fixed amount of photon (radiative) energy and it travels through the domain, undergoing absorption, scattering and reflection until it leaves the computational domain or is completely absorbed by the medium [1]. One important advantage of the PMC is that an increase in problem complexity does not add much to the numerical cost. This method is particularly well suited to model TRI because it can model abosrption TRI rigorously without the need for any additional approximations (such as OTFA).

A PMC method can either be a standard or energy-partitioning Monte Carlo [1]. In the energy partitioning method, the ray energy is progressively deposited in cells, through which the ray travels, instead of depositing all the energy in a single cell (as done in the standard Monte Carlo). This method is slightly more expensive per bundle than standard Monte Carlo, but results in much lower statistical variations. Hence a large variety of highly complicated problems can be simulated with reasonable efficiency and computing times. Application of PMC to reacting flows is complicated by the fact that the participating medium (i.e., combustion gases) and temperature are highly inhomogeneous throughout the domain. In practical CFD codes all turbulent structures are not resolved (and models are applied for unresolved structures).

3.5.1 PMC For Discrete Particle Fields

When using hybrid finite volume/PDF Monte Carlo methods to simulate turbulent reacting flows, the scalar fields are represented by discrete particles. Each particle is a flow-realization so that a particle field can be considered to be an instantaneous snapshot of the turbulent flow field. Based on this assumption, Wang and Modest [74, 96]

developed a PMC method for media represented by discrete particles. The particles were modeled as either point masses (PPM) or as spherical particles (SPM); the rays were either modeled as standard volume-less lines (Line) or assigned a small solid angle and hence treated as a cone with decaying influence function from the centerline. Based on these models, three different interaction schemes between rays and particles were proposed, i.e., Line-SPM, Cone-PPM, and Cone-SPM methods. From these, it was found that all the three models yielded correct results in test problems. However, when applied to a turbulent flow-field snapshot, in which each particle represents a δ-PDF, only the Cone-PPM model is deemed appropriate (rays are modeled as a cone with a small solid opening angle and particles are modeled as point masses). The schematic of the Cone-PPM model for PMC is shown in Fig. 3.2. Following the development of Wang [96], and

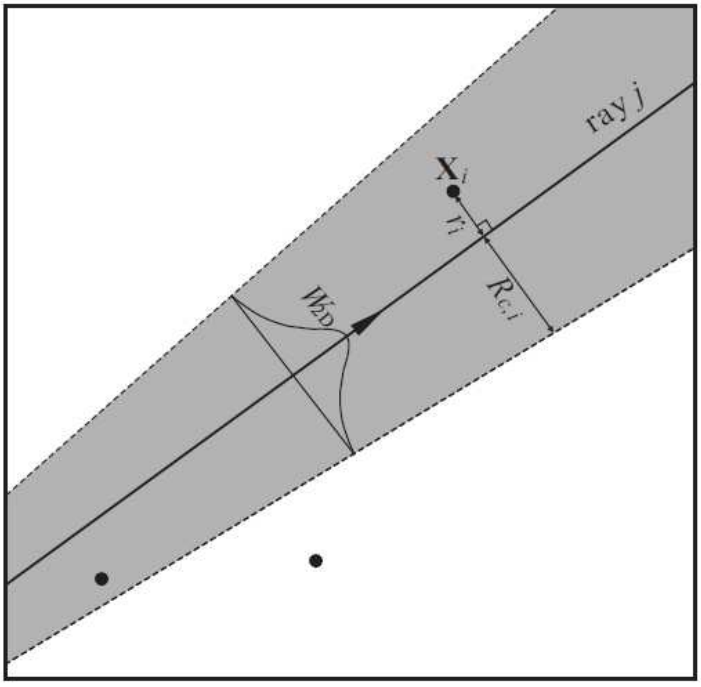

Figure. 3.2 Cone-PPM Scheme (from [96])

referring to Fig. 3.2, the contribution of a specific particle i to the optical thickness that ray j travels through can be written as

$$\Delta\tau_{i,j} = \frac{\kappa_{\rho,i} W_{ij} m_i}{\pi R_{c,ij}^2}, \tag{3.12}$$

where, $\kappa_{\rho,i}$ is the density-based absorption coefficient of the particle based on its composition, and is, in general a spectral quantity and W_{ij} is a normalized two-dimensional center-symmetric weight function that satisfies

$$\int_0^1 W_{2D}(r') 2r' dr' = 1 \quad \text{and} \quad r' = r/R_c, \tag{3.13}$$

R_c (and $R_{c,ij}$) is the local influence radius as depicted in Fig. 3.2 of the cross section normal to the cone axis, and m_i is the mass of particle i.

With this scheme, when the ray opening angle is increased, more particles are captured by the ray. However, more time is spent in computing the change in optical thickness along with a loss in fine resolution. Similarly, when the ray opening angle is decreased, fewer particles interact with the ray, resulting in a speed-up, but also accompanied by more statistical scatter. After detailed studies of the numerical efficiency of this scheme, Wang [96] concluded that a ray opening angle of 1° resulted in maximum numerical efficiency. The particle–ray interaction scheme described above is also coupled with an adaptive emission scheme to limit the ray energies to a small range. This results in more rays being emitted from important hot regions, while reducing the number of rays emitted from cold regions (which do not contribute much to the total radiative

transfer). Such a scheme greatly reduces statistical errors, with little increase in the CPU times, compared to the scheme where all particles emit identical numbers of rays.

3.5.2 Spectral Photon Monte Carlo

Modest [97] developed random number relations for nongray gases to be used in PMC, based on a statistical narrow-band model. Farmer and Howell [98] developed random number relationships based on an exponential wide-band absorption profile to treat nongray emission and absorption of carbon dioxide. Most recently Wang and Modest [14, 96] proposed a PMC coupled with both the full-spectrum k-distributions (FSK) as well as line-by-line (LBL) calculations. They showed that the computational cost for both methods was comparable. Thus, with this method it will be possible to attain line-by-line accuracy for radiative calculations in reacting flows.

Following the development of Modest [1], the probability of a photon being emitted in a differential wavenumber interval $d\eta$ is proportional to the Planck function weighted by the spectral absorption coefficient, i.e.,

$$\text{Probability}(\eta \leq \eta^{'} \leq \eta + d\eta) \propto \kappa_{\eta} I_{b\eta} d\eta \tag{3.14}$$

To simulate emission from such a nongray gas, using photon bundles, one can statistically map the wavenumber for a given gas-phase species i to a uniform random number $R_{\eta,i} \in [0, 1)$ such that,

$$R_{\eta,i} = \frac{\int_0^{\eta} \kappa_{\eta,i} I_{b\eta} d\eta}{\int_0^{\infty} \kappa_{p,\eta,i} I_{b\eta} d\eta} = \frac{\int_0^{\eta} \kappa_{p,\eta,i} I_{b\eta} d\eta}{\int_0^{\infty} \kappa_{p,\eta,i} I_{b\eta} d\eta} = \frac{\pi}{k_{p,i} \sigma T^4} \int_0^{\eta} \kappa_{\eta} I_{b\eta} d\eta \tag{3.15}$$

where, $\kappa_{p,\eta,i} = \kappa_{\eta,i}/p_i$ is the pressure-based spectral absorption coefficient, and p_i is the partial pressure of species i; $k_{p,i}$ is the Planck-mean pressure-based absorption coefficient. Since Eq.(3.15) is an implicit relationship between the random number and the wavenumber, it is more convenient to tabulate this relationship in a database and invert random numbers to obtain the emission wavenumbers for the photon bundles.

When dealing with mixtures of multiple absorbing-emitting gases, employing the fact that absorption coefficients are additive, one can derive a random number relationship between wavenumber for the mixture and a uniform random number $R_\eta \in [0, 1)$. It can be shown that [96]

$$R_\eta = \frac{\sum_i x_i k_{p,i} R_{\eta,i}}{\sum_i x_i k_{p,i}}, \tag{3.16}$$

where $x_i = p_i/p$ is the mole fraction of species i, p is the total pressure of the mixture, and $R_{\eta,i}$ are the species random numbers.

It can be seen that the relationship between η and R_η is implicit and as such a mapping between R_η to η has to be done by trial and error. If the total pressure is fixed, then both the species random number as given in Eq.(3.15) and the pressure-based absorption coefficient are functions of wavenumber, temperature species mole-fractions only, i.e.,

$$R_{\eta,i} = f_{R,i}(\eta, T, x_i), \quad \kappa_\eta = f_{\eta,i}(\eta, T, x_i), \quad i = 1, 2, \ldots, N_{rs}, \tag{3.17}$$

where N_{rs} is the number of radiating species considered. If self-broadening is neglected, then both these are functions of wavenumber and temperature only. Thus, it is possible to tabulate both $R_{\eta,i}$–η and $\kappa_{p,\eta,i}$–η relationships, followed by a 3D interpolation scheme (or 2D if self-broadening is neglected), to get a unique mapping between R_η and η. It is

also reported that a bisection search algorithm is used to invert the relationship between $R_{\eta,i}$–η, to obtain the emission wavelength. Once η is fixed, the absorption coefficient can be obtained directly from $\kappa_{p,\eta,i}$–η tabulated values. A similar formulation can also be done based on the FSK approach [96]. However, it was found that the numerical effort when using the PMC was similar irrespective of whether the spectral model is based on FSK or LBL. It should be noted that efficient utilization of LBL approach requires very high memory resources during computations, as the LBL random-number tables need to be populated in the run-time memory. In the current work the power of PMC is utilized and radiation modeling is done using the LBL approach for carbon dioxide, water vapor and soot. In addition, the Cone-PPM model also allows capturing of absorption TRI appropriately.

3.6 Summary

The radiative transfer equation was introduced, and the origin of emission TRI and absorption TRI was explained. The most relevant literature on modeling TRI was reviewed. The basic formulation of the PMC for use in media represented by discrete particles was presented. The spectral formulation of the PMC was briefly reviewed. The PMC can achieve line-by-line accuracy as well as model emission and absorption TRI accurately, thus achieving all the radiation modeling objectives required for the current study.

Chapter 4

Soot Modeling

4.1 Introduction

Soot formation is one of the most complex problems in combustion science, and remains poorly understood. There has been increasing need to design combustion systems in which the amount of soot is controlled. Intense experimental and theoretical research has improved the fundamental understanding of the various soot formation processes. New insight into the controlling physical and chemical mechanisms has been used to develop simple design guidelines, empirical correlations, semi-empirical computer models or full-blown attempts to describe detailed elementary chemical reactions and physics of soot formation [2, 99–101]. Accurate prediction of soot formation is of interest for various reasons; the main ones are summarized here.

- Formation of soot reduces the carbon available for combustion and hence reduces the efficiency of combustion.
- Industrial furnaces may actually require increased soot formation to enhance the heat transfer via radiation for heating purposes. A corresponding need is to design devices to oxidize the excess soot to prevent it from being released into the atmosphere.

- Soot can contain (in trace amounts) volatile materials, which may be hazardous to the environment.

- Soot formation processes can be used to develop products including carbon black, which has a wide range of applications from printing ink materials to fillers in rubber manufacturing.

4.2 Soot Formation and Oxidation

Soot formation involves highly coupled chemical and physical processes. In terms of the underlying processes, soot formation can be viewed as consisting of four major subprocesses [2, 99, 102]: homogeneous nucleation of soot particles, particle coagulation, particle surface reactions (growth and oxidation), and particle agglomeration. Each of these processes has been studied by various researchers and will be reviewed briefly.

4.2.1 Nucleation

Several proposals have been made as to the general nature of soot particle inception; these include polyacetylenes, ionic species [103], or polycyclic aromatic hydrocarbons (PAH) [102]. The current consensus, supported by numerous experimental and modeling studies, is that soot particles form mainly via PAHs. In understanding formation of PAH, the primary focus is on the formation of the first aromatic ring (benzene C_6H_6) from small aliphatics (straight-chained molecules), as this step is perceived by many as the rate-limiting step in the reaction sequence to larger aromatics [104–106].

The formation of the aromatic ring is followed by growth of these aromatics into PAH. Frenklach and Wang [104, 107] proposed a mechanism "H-abstraction-C_2H_2 - addition" (HACA), which implies a repetitive reaction of two principal steps: (i) Abstraction of a hydrogen atom from the reacting hydrocarbon by a gaseous hydrogen atom,

$$A_i + H \leftrightarrow A_{i^-} + H_2, \tag{4.1}$$

followed by (ii) addition of a gaseous acetylene molecule to the radical site formed,

$$A_{i^-} + C_2H_2 \rightarrow \text{products}. \tag{4.2}$$

Here A_i is an aromatic molecule with i rings, and A_{i^-} is its radical. The key feature of this mechanism is the reversibility of reaction (4.1). The reverse reaction can be one of the following:

$$A_{i^-} + H_2 \rightarrow A_i + H, \tag{4.3}$$

or

$$A_{i^-} + H \rightarrow A_i. \tag{4.4}$$

The contribution of reaction (4.3) increases with pressure and molecular size as compared to reaction (4.4). The reversibility of the acetylene addition step (reaction 4.2) determines the total rate of molecular growth. It has been found that this mechanism of PAH growth is the most (thermodynamically) stable pathway; by a repetitive re-activation through hydrogen atoms, the PAH molecules grow by acetylene addition and hop from one island of stability to another [108].

Acetylene is not the only species that can be responsible for growth of aromatic rings. Several other proposals have been made including those involving methyl, propargyl, and cyclopentadienyl radicals. The main focus is on the possibility of forming relatively stable radicals which grow and form larger molecules. A good summary of these mechanisms can be found in [108].

Parallel to aromatics growth is aromatics oxidation, primarily by O_2 and OH. The effect of oxidation at the small-molecule level is twofold. On the one hand, it diverts carbon mass from further growth. On the other hand, in high-temperature environments, molecular oxygen actually promotes formation of soot by building up the radical pool, mainly H atoms, thereby promoting the HACA mechanism discussed earlier. Thus, the net effect of higher O_2 can be the reverse of reducing the amount of PAHs produced (i.e., PAH oxidation due to higher O_2 content may be off-set by PAH growth due to HACA).

The transition of gas-phase species to solid particles is probably the least understood part of the soot formation process. In early models, soot was defined as the mass accumulated in PAH species above a certain size; thus it was assumed that transition from gaseous species to solid particles happens purely by chemical growth. This model was later expanded [104, 107] by proposing that at some size, the PAH species begin to stick together forming PAH dimers. The PAH dimers collide with other PAH molecules to form PAH trimers and tetramers and so on; meanwhile, individual PAH species keep increasing in size via molecular chemical reactions. Thus, formation of PAH dimers is assumed to mark the emergence of a "solid" particle phase [108].

4.2.2 Coagulation and Aggregation

Once soot particles are formed, they collide with each other forming larger particles. Experimental studies revealed that initially the particles look spherical and later grow into agglomerates, which no longer retain spheroidal geometry but look more like mass fractals [102]. Hence, particle coagulation is usually classified as coalescent growth and agglomeration into (fractal) aggregates.

In the coalescent regime the particles are assumed to collide and coalesce completely. The phenomenology and mathematical treatment of this regime is similar to aerosol dynamics [109, 110]. It is usually presumed that the formation of spherical soot particles precedes that of aggregates, but transition from spherical to fractal growth is not well understood. One point of view is that the particles are composed of viscous matter that coalesces completely at small sizes but does not have sufficient time for fusion as the particle size increases. Another point of view is that the nearly spherical shape of primary particles is the product of simultaneously occurring coagulation and surface growth and the transition to fractal aggregates is caused by cessation of surface growth. Recent kinetic molecular dynamics (KMD) studies by Frenklach and coworkers [111] show that particle aggregation begins at the onset of nucleation itself. In the absence of surface growth there is no smoothing mechanism, which is necessary to construct spheroidal particles. However, the surface reactions need to be fast enough to bury the colliding particles stuck on the surface of larger particles. If the colliding particles are too large, the surface growth is not able to bury them and the structures attain the shape of nonspherical mass-fractal-like properties.

4.2.3 Surface Reactions: Growth and Oxidation of Soot Particles

The number of nascent soot particles is controlled by the kinetics of nucleation, and coagulation controls the evolution of the particle number density, i.e., the number of "independent" particles in a given control volume. However, the amount of carbon mass accumulated in soot is determined primarily by surface reactions. It was established in experimental studies of laminar premixed flames that acetylene is the principal gaseous species that reacts at the particle surface and that this carbon deposition process follows first-order kinetics [112]. Species other than acetylene have been thought of as possible surface growth precursors, mostly aromatics [113, 114]. However, unresolved issues remain with these species [115].

A key idea was the introduction of the hypothesis of chemical similarity, which postulates that chemical reactions taking place on soot particle surfaces are analogous to those for large PAH molecules [107]. In other words, the surfaces of soot particles are assumed to look like the edge of a large PAH molecule covered with C-H bonds. Abstraction of H atoms activates these sites, forming surface radicals, which react with incoming gaseous species – both hydrocarbons promoting growth and oxidizing agents, which remove the carbon from soot particles. This is essentially similar to the HACA mechanism used in PAH growth and can be termed surface-HACA [108]. The surface-HACA mechanism is consistent with the findings of Harris and Weiner [112], who identified that acetylene dominated surface growth in their flames. Recent re-examination of surface growth by Faeth and coworkers also supports the validity of HACA in explaining

the observed soot surface growth rates in a series of laminar premixed [116, 117] and diffusion [118] flames.

Table 4.1 Soot surface growth mechanism. Here $\rightarrow$ indicates an irreversible reaction and $\leftrightarrows$ denotes a reversible reaction, C_s denotes a soot particle and C_s^* is a soot radical. The kinetic rate coefficients for each of the reactions and other details can be found in the references listed.

No.	Reaction	References
1	$C_s + \mathrm{H} \leftrightarrows C_s^* + \mathrm{H_2}$	[15, 104]
2	$C_s + \mathrm{OH} \leftrightarrows C_s^* + \mathrm{H_2O}$	[15, 104]
3	$C_s^* + \mathrm{H} \rightarrow C_s$	[104]
$4A$	$C_s + \mathrm{C_2H_2} \rightarrow C_s + \mathrm{H}$	[104]
$4B$	$C_s + \mathrm{C_2H_2} \rightarrow C_s^* + \mathrm{H}$	[119]
5	$C_s^* + \mathrm{O_2} \rightarrow 2\mathrm{CO} + \mathrm{products}$	[104]
6	$C_s + \mathrm{OH} \rightarrow \mathrm{CO} + \mathrm{products}$	[104, 120]

Experimental observations on soot formation in premixed flames indicates that the surface growth rate of soot particles declines with the extent of particle growth [102, 112]. This phenomenon is called "soot surface aging." This aging has been attributed to two factors [104]: a decrease in H atom concentration and a decrease in the number of active sites on the soot particle surface capable of sustaining growth. The first factor reduces the kinetic driving force of the HACA mechanism and the second factor reduces the surface reactivity of the soot particle. This change in surface reactivity needs to be accounted for in the models. The surface-HACA mechanism is summarized in Table 4.1. The kinetic rate coefficients for each of the reactions and details can be found in the references listed in the table. In the present work the surface-HACA mechanism will be used [104]. A key element of that mechanism is that surface radicals are completely depleted during the acetylene addition step. Wang et al. [119] reported that this mechanism

under-predicts soot by an order of magnitude in opposed-flow diffusion flames. They reported improved agreement with experiments with surface radicals conserved during the acetylene addition step. They also noted that reality probably lies somewhere between the two extremes of complete depletion and complete conservation of radical surface sites; i.e., reactions $4A$ and $4B$ in Table 4.1 must be happening simultaeously and not exclusively.

4.3 Modeling Soot Formation

Successful modeling of soot requires accurate accounting of both formation and oxidation. However, this entails modeling of highly coupled non-linear processes of both physical and chemical nature. Difficulties and uncertainties in understanding the soot processes impedes progress in accurate soot prediction. Models of different sophistication levels have been put forth and applied to many practical systems, and can be broadly classified into empirical, semi-empirical and detailed models [2]. Semi-detailed/semi-

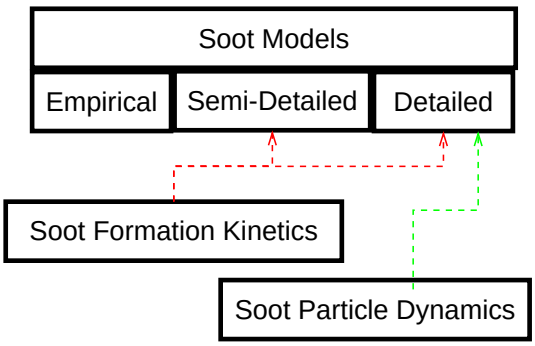

Figure. 4.1 Types of soot models.

empirical models attempt to incorporate some aspects of the physics and chemistry of

the phenomena, instead of just correlations based on experimental data. Rate expressions are developed for each subprocess, and the rate coefficients for each are generally adjusted to match the experimental soot profiles. Semi-empirical models typically involve a set of coupled differential equations, usually for the particle number density and a soot mass fraction or soot volume fraction. Although still crude, semi-empirical models help to understand the sooting processes. In semi-empirical models, the total particle number density is calculated and the particle size distribution is generally unknown [121, 122]. Models that rely on empirical inputs for soot nucleation, growth and oxidation are limited inherently to specific conditions. Detailed models use detailed chemical kinetics and physical models to describe each sub-process that occurs in the gas-phase, solid-phase and on the surface of soot particles. Thus, the detailed models hold maximum promise of predictive abilities over a wide range of operating conditions. Accounting accurately for soot-particle dynamics is the key feature of various detailed and semi-detailed models.

Table 4.2: Particle dynamics models

Models	Reference	PSDF Information	Key feature	Key limitation
Discrete Sectional Methods	Colket and Hall [106]	PSDF resolved into finite sections	Deal with bimodal PSDF accurately	Number of sections needed for resolution can be very large
Method of Moments	Frenklach [123]	Average properties of PSDF (moments)	Accurate and computationally feasible	Limited applicability if bimodal distribution exists
Stochastic Model	Balthasar and Kraft [124]	PSDF regenerated using Monte Carlo	PSDF can be more predicted more accurately	No feedback to flow-field, limited to frozen field analysis

Continued on Next Page...

Table 4.2 – Continued

Models	Reference	PSDF Information	Key feature	Key limitation
Kinetic Molecular Dynamics	Mitchell and Frenklach [111]	Molecular level soot formation	Detailed insight into soot formation processes	Cannot be used for engineering level problems

The main objective of the detailed models is to predict properties of the soot particle size distribution function (PSDF). Various models have been proposed for this purpose. The soot particle dynamics have been modeled using the discrete-sectional method [106] and the method of moments [104, 125]. The method of moments has the merit of computational economy while modeling soot processes in sufficient detail. Balthasar and Kraft [124] recently proposed a stochastic method to solve for the particle size distribution function (PSDF) directly instead of solving for the moments of the distribution function. The method is based on a stochastic particle system, and soot formation subprocesses can be treated probabilistically. However, the method is a Monte Carlo inversion technique and needs inputs about all the scalars and soot moments to generate the PSDF. Available particle dynamics methods are summarized in Table 4.2.

4.4 Method of Moments

The starting point for the method of moments is the time evolution of a particle ensemble (without any reactions) described by population balance equations known as the "Smoluchowski master equations" [109, 110]. These can be written as

$$\frac{dN_1}{dt} = -\sum_{j=1}^{\infty} \beta_{1,j} N_1 N_j, \tag{4.5a}$$

$$\frac{dN_i}{dt} = \frac{1}{2}\sum_{j=1}^{i-1} \beta_{j,i-j} N_j N_{i-j} - \sum_{j=1}^{\infty} \beta_{i,j} N_i N_j \qquad i = 2 \ldots \infty. \tag{4.5b}$$

Here N_i denotes the number of particles of size i per unit volume, i.e., size i particle number density. N_1 is the number density of the smallest particles and $\beta_{i,j}$ is the collision

coefficient between particles of size i and j. In general, then, $\beta_{i,j} = \beta_{i,j}(N_i, N_j, m_i, m_j)$ where m_i is the mass of particle of size i.

The greatest difficulty in solving these equations comes from the dependence of $\beta_{i,j}$ on the sizes of the colliding particles. Earlier models, which assumed a constant $\beta_{i,j}$ were found to be inaccurate and lacked physical justification. The key features of the Smoluchowski equations, Eqs. (4.5a) and (4.5b), are as follows:

- They conserve the total particle mass, i.e., there is no net particle creation (nucleation) or destruction (complete oxidation).
- The particles grow only by coagulation, i.e., there are no surface reactions, but only collisions of particles.
- The first term in Eq.(4.5b) represents creation of current (i-sized) particles by collision of smaller particles and the second term denotes destruction of current (i-sized) particles by collision with all other particles.

If all $N_i, i = 1 \ldots \infty$, are known, the particle size distribution function (PSDF) is known and all physical quantities can be easily determined. The solution of Eqs. (4.5a) and (4.5b) is prohibitively expensive, as there will be as many coupled ODEs as there are particle size classes.

4.4.1 Method of Moments: Formulation

The concentration moment of the particle number density function N_i is

$$M_r = \sum_{i=1}^{\infty} m_i^r N_i \tag{4.6}$$

It can be seen that if $r = 0$, then $M_0 = \sum_{i=1}^{\infty} N_i$ is the total particle number density. For $r = 1$, $M_1 = \sum_{i=1}^{\infty} m_i N_i$ is the total mass of particles per unit volume, so that the volume fraction is given by $f_v = M_1/\rho_s$. Higher-order moments may lack simple physical interpretation but are needed for accuracy. It can be seen that the knowledge of all integer moments ($r = 0, \ldots, \infty$) is equivalent to the knowledge of the size distribution function itself. However, most of the principal properties for the particle ensemble can be deduced from the first few moments.

Multiplying Eqs. (4.5a) and (4.5b) by m_i^r and summing over all size classes $i = 1, \ldots, \infty$ results in a general form of equations given by [123]

$$\frac{d}{dt}\left[\sum_{i=1}^{\infty} m_i^r N_i\right] = G_r, \quad r = 0, \ldots, \infty. \tag{4.7}$$

In this case, $G_1 = 0$ since the total mass of the particles does not change during evolution. However, when one adds processes such as surface reactions, nucleation etc., this does not remain the case. With the assumption $m_i = i m_1$, it can be shown that,

$$G_0 = \frac{1}{2}\sum_{i=1}^{\infty}\sum_{j=1}^{\infty} \beta_{i,j} N_i N_j \quad , \tag{4.8a}$$

$$G_r = \frac{1}{2}\sum_{k=1}^{r-1} \binom{r}{k} \left(\sum_{i=1}^{\infty}\sum_{j=1}^{\infty} m_i^k m_j^{r-k} \beta_{i,j} N_i N_j\right) \quad . \tag{4.8b}$$

The collision coefficient $\beta_{i,j}$ is nonadditive and its functional form depends on the coagulation regime, which is generally classified based on the Knudsen number, Kn =

$2\lambda_f/d$, where λ_f is the mean free path (for particle collision) and d is the particle diameter. Details can be found in Appendix A.

4.4.2 Particle coagulation

Physically, particle coagulation is a process in which small particles (assumed to be spherical) collide with each other and coalesce completely to form larger spherical particles. It has been found in kinetic molecular dynamics (KMD) simulations that small particles are indeed spheroidal, and the assumption of spherical particles seems to be reasonable [111, 126]. After a certain size, however, the particles cannot coalesce completely and start to form long chains, which eventually grow into three-dimensional fractal-like structures. This is particle aggregation and will be considered later on.

Particle coagulation can be modeled in the two limits of continuum and free-molecular regimes; i.e., the functional form of $\beta_{i,j}$ can be derived and transformed for use in the moment equations (4.8). Details are again provided in Appendix A.

4.4.3 Particle nucleation

Particle nucleation is the most important step in soot formation and results in generation of the smallest size particles N_1. A general equation for this can be written as [123, 127]

$$\frac{dN_1}{dt} = R_{N_1} - G_{N_1} - \frac{k_s s_1}{\Delta m} N_1, \tag{4.9}$$

where R_{N_1} is the chemical pathway for generating the smallest soot particles, G_{N_1} is the reduction of these particles by coagulation with other particles, and the last term on the right-hand-side is the destruction of these particles by surface reactions (oxidation by

O_2 and OH molecules) modeled using a reaction rate k_s per unit area; s_1 is the surface area of the smallest particle.

The nucleation rates need to be transformed for use in the moment equations so that the moment equations take the form

$$\frac{dM_r}{dt} = R_r + G_r. \tag{4.10}$$

The most comprehensive model for soot nucleation is probably due to Frenklach and Wang [104, 108]. However, it is far too complex for present purposes, as it involves additional moment equations for the PAH distribution function, and needs ~ 100 species and $\sim$ 500 reactions [128]. A proposition by Frenklach and Harris [125] is to treat Eq.(4.9) as an additional equation to the moment equations and to model each of the terms separately. Following [104], the soot particles can be assumed to be initiated by PAH coagulation, i.e., by the coalescence of two PAH species into a dimer. The formation rate of all possible dimers is then given by

$$R_r = \frac{1}{2}\sum_{i=i_0}^{\infty}\sum_{j=i_0}^{\infty}\beta_{i,j}^{\mathrm{PAH}}(m_i + m_j)^r N_i^{\mathrm{PAH}} N_j^{\mathrm{PAH}}, \quad r = 0, 1, \ldots, \tag{4.11}$$

where

$$\beta_{i,j}^{\mathrm{PAH}} = \epsilon\sqrt{\frac{\pi k_B T}{2\mu_{i,j}^{\mathrm{PAH}}}}(d_i + d_j)^2 \tag{4.12}$$

The terms $\mu_{i,j}^{\mathrm{PAH}}$ are the corresponding reduced moments of the PAH concentration and cannot be easily obtained. A simpler implementation of this is available in [129, 130] as

$$R_0 = \epsilon \sqrt{\frac{4\pi k_B T}{m_C N C_{\mathrm{PAH}}}} d_{\mathrm{PAH}}^2 N_{\mathrm{PAH}} N_{\mathrm{PAH}} \tag{4.13a}$$

$$R_r = 2 N C_{\mathrm{PAH}} R_{r-1} \tag{4.13b}$$

where NC_{PAH} is the number of carbon atoms per PAH molecule, m_C is the mass of carbon molecule C_2, and N_{PAH} is the number density of the PAH molecules involved in soot nucleation. The diameter of the PAH molecule and other properties can be calculated. N_{PAH} can be obtained from the molar concentration of the PAH species.

Lindstedt and coworkers [131, 132] assumed a very simple nucleation step given by

$$R_r = 2 \frac{N_A}{C_{\mathrm{min}}} k_N(T) [\mathrm{C_2H_2}], \quad r = 0, 2, 3, \ldots, \tag{4.14}$$

where N_A is Avogadro's constant and C_{min} is the number of carbon molecules in the smallest PAH which coagulates into a dimer to form the incipient soot particle.

4.4.4 Surface reactions

Surface growth is the process of mass deposition on the particle surface by gas-phase chemical species. The basic mathematical formulation for inclusion of a surface

growth rate in the moment equations can be written as follows [123]:

$$\frac{dN_1}{dt} = -\frac{r_s N_1 s_1}{\Delta m} \tag{4.15a}$$

$$\frac{dN_i}{dt} = \frac{r_s}{\Delta m}(N_{i-1}s_{i-1} - N_i s_i) \tag{4.15b}$$

where r_s is the growth rate per unit area, s_i is the area of particle of size i and Δm is the difference in mass between adjacent bins. It should be noted that as soon as a particle in bin size i adds mass in the amount of Δm, it "shifts" to bin $i+1$. Multiplying Eq.(4.15) by m_i^r and summing over all size classes, one obtains [123]

$$\left(\frac{dM_r}{dt}\right)_{\text{surface growth}} = W_r = \frac{r_s}{\Delta m}\sum_{k=0}^{r-1}\binom{r}{k}\sum_{i=1}^{\infty}\Delta m^{r-k} m_i^k N_i s_i \quad r = 1, 2, \ldots \tag{4.16}$$

Depending on the size of the soot particle, W_r can either be modeled as a spherical particle or as an aggregate. In the current work, particles are modeled as spherical. The surface growth rate needs to be added to the total "production rates" of the moments so that the evolution of the moments takes the form,

$$\frac{dM_r}{dt} = R_r + G_r + W_r \tag{4.17}$$

The simplest case is to consider spherical particles, for the surface area is a direct function of the particle diameter. Using the kinetic mechanism of surfcae-HACA [104] shown in Table 4.1, it can be shown that with one surface growth reaction a mass

equivalent to two carbon atoms is added to a (soot) particle. The mass of hydrogen is generally neglected without any serious error in the formulation [104]. Thus $\Delta m = 2m_C$ can be used in Eq.(4.16). The surface area of the particle is calculated with the assumption $m_i = im_1$, so that one obtains [104, 125, 127]

$$W_r^{\text{coag}} = k_{sg} C_g \alpha \chi_s \pi \left(\frac{6m_C}{\pi \rho_s}\right)^{2/3} M_0 \sum_{k=0}^{r-1} \binom{r}{k} \Delta^{r-k} \mu_{r+2/3} \quad r = 1, 2, \ldots, \tag{4.18}$$

where k_{sg} is the kinetic rate coefficient for reaction with gas g, C_g is the molar concentration of the gas species, α is a steric factor as explained below, χ_s is the nominal number density of surface radical sites, Δ is the number of carbon atoms added/removed from the particle due to reaction with gas g, m_C is the mass of the carbon atom, μ_x is the reduced fractional moment of the PSDF and ρ_s is the density of soot generally taken as 1.8 g/cm^3 [104]. There are a multitude of approximations and assumptions in Eq.(4.18), which are summarized as:

1. Surface growth is assumed to occur due to reactions of C_2H_2 with surface radicals, and condensation of PAH on the particle surface. Surface oxidation is due to reactions of O_2 with surface radicals and reactions of OH with the particle surface. These reactions are assumed to be analogous, at each active site on the particle surface, to the corresponding gaseous reactions of large PAH molecules [104].

2. k_{sg} is the reaction rate for the modeled reaction of the soot with a participating gaseous species g, which is one of the species on the right-hand-side of the reactions shown in Table 4.1.

3. C_g is the molar concentration of the gaseous species.

4. χ_s is the number density of the surface radical sites, which is determined from the number density of total surface sites, which in turn are estimated to be 2.5×10^{15} cm^{-2} [107]. A kinetic steady-state approximation is then used to obtain the total radical sites available on the particle for reactions with gas-phase species which is given by $\chi_s = K_{\text{steady}} \chi_{\text{all}}$ [104].

5. The factor α is the fraction of the surface sites available for chemical reactions, and was introduced into the equations by Frenklach and Wang [107] to account for the difference between the soot surface growth rates in low- and high-temperature flames [15]. It was suggested that α quantifies the changing morphology of the soot particle surface, as it travels in the post-flame region and that the extent of this change is dependent on the particle surface temperature. The physical rationale is that α considers the growing soot surface to have "graphitic" edges amenable to chemical reactions, but some parts are comprised of nonreactive basal aromatic planes [15]. The temperature-dependent α-model for surface growth was confirmed by Faeth and coworkers in the post-flame regions of laminar premixed flames [116, 117].

6. The functional form for α has been evolving over the years, starting with constant values [104, 106] to a temperature-dependent value used by Appel et al. [15]

$$\alpha = \tanh[a(T)/\log \mu_1 + b(T)]. \tag{4.19}$$

By comparing experimental results from seven laminar premixed flames from different investigators, they were able to deduce $a(T)$ and $b(T)$ as linear functions of local temperature T.

The details of the full formulation, including coagulation and surface reactions and expressions for fractional moments based on an interpolative closure proposed by Frenklach and coworkers, can be found in Appendix A. This model is used in the current study after careful validation in laminar flames as discussed in Chapter 5.

The method of moments model can be extended to handle soot aggregation into nonspherical mass-fractals [127]. However, such formation is expected more in high pressure flames. An important effect of a mass-fractal like morphology is an increase in available surface area for surface growth and oxidation and changes in the radiative properties of soot particles (as scattering can become important) [133].

4.5 Soot Radiative Property Models

The principal approximations for the radiative properties of soot particles can be divided into three classes: (i) Rayleigh scattering, used for small particles; (ii) Mie scattering theory, used if the particles assumed to be spheres are too large to apply the Rayleigh theory; and (iii) Rayleigh-Debye-Gans theory for fractal aggregates (RDG-PFA), for which the particles cannot be modeled as spheres and hence Mie theory cannot be applied [134]. It has been shown by Kazakov and Frenklach [127] that, at atmospheric and subatmospheric pressures, soot maintains a spheroidal geometry. However, at higher pressures, the surface growth rate and coagulation are such that soot particles no longer

maintain a spherical geometry. Instead, the soot particles become mass-fractal like structures, thereby making radiative property calculations complex [133].

In the current study, the soot particles are assumed to be spherical and small compared to the wavelength of the light; this limits the applicability to atmospheric or slightly higher pressures. In such cases, one can use the Rayleigh theory to obtain expressions for both the absorption and scattering coefficients of the soot particles [1].

The radiative properties of a cloud of spherical particles of radius a, interacting with an electromagnetic wave (light) of wavelength λ, are governed by three independent nondimensional parameters: (i) Complex index of refraction $m = n - ik$, (ii) size parameter $x = 2\pi a/\lambda$, and (iii) clearance-to-wavelength ratio c/λ. In general, independent scattering can be assumed ($c/\lambda \gg 1$) and only the first two parameters are required [1]. The values of n and k have been investigated by various researchers, and are been known to functions of wavelength [135, 136]. However, many experimentalists have used constant values for the complex index of refraction to interprete measured intensities.

At atmospheric pressure, typcial soot particle diameters are 30–50 nm, and are typically irradiated by light with wavelength ~ 3.0 μm, resulting in $x \simeq 0.05$. In the limit $x \to 0$ it can be shown that the scattering and absorption cross-sections of the soot particles are given by [1],

$$Q_{\text{sca}} = \frac{8}{3}\left|\frac{m^2-1}{m^2+2}\right|^2 x^4 \quad , \tag{4.20}$$

$$Q_{\text{abs}} = -4\mathcal{I}\left\{\frac{m^2-1}{m^2+2}\right\} x \quad . \tag{4.21}$$

Thus it can be seen that, if $x \ll 1$, scattering from the soot particles can be neglected. In aggregated form, scattering and absorption cross-sections are more complex to evaluate [133], and scattering may become important. Based on Eq.(4.21), and if the soot particles are small, it is possible to deduce the spectral absorption coefficient of soot as [1]:

$$\kappa_\lambda = \frac{36\pi nk}{(n^2 - k^2 + 2)^2 + 4n^2k^2} \frac{f_v}{\lambda} \tag{4.22}$$

where f_v is the soot volume fraction and λ is the wavelength. Chang and Charalampopulous [136] reported functional forms of n and k for soot particles as a function of wavelength, based on a series of experiments. They developed the following correlations:

$$n = 1.811 + 0.1263(\ln \lambda) + 0.0270(\ln \lambda)^2 + 0.0417(\ln \lambda)^3 \quad , \tag{4.23}$$

$$k = 0.5821 + 0.1213(\ln \lambda) + 0.2309(\ln \lambda)^2 - 0.0100(\ln \lambda)^3 \quad , \tag{4.24}$$

where λ is the wavelength of light in μm. These correlations have been used in the current study to evaluate spectral soot absorption coefficients.

4.5.1 Nongray Soot in PMC

Based on Eqs. (4.23) and (4.24) and Eq.(4.22), the random number relationships for soot can be calculated similar to Eq.(3.15) as

$$R_{\eta,s} = \frac{\pi}{k_{p,s}\sigma T^4} \int_0^\eta \kappa_{\eta,v,s} I_{b\eta} d\eta, \tag{4.25}$$

where the subscript s denotes soot, $\kappa_{\eta,v,s} = \kappa_{\eta,s}/f_v$ is the soot-volume-fraction based spectral absorption coefficient of soot, and $k_{p,s}$ is the corresponding Planck-mean absorption coefficient for soot. Thus, the random number relationship for mixtures of nongray gases and soot can be calculated similar to Eq.(3.16) as

$$R_\eta = \frac{P\sum_i x_i k_{p,i} R_{\eta,i} + f_v k_{p,s} R_{\eta,s}}{P\sum_i x_i k_{p,i} + f_v k_{p,s}} \tag{4.26}$$

where subscript i denotes participating gaseous species, and s denotes soot. Similar to the approach used in gas-phase random-number databases, the mapping between $R_{\eta,s}$–η and $\kappa_{\eta,v,s}$–η can be tabulated once and for all, and then used as necessary. Additional details of this approach can be found in [96].

This approach needs some modifications if the absorption coefficient of soot is not directly proportional to the soot volume fraction. For example, when dealing with mass-fractal-like aggregates, which can be much larger, the Rayleigh approximation fails. However, such a model is not a part of the current study.

4.6 Soot Moment Transport Equations

The transport equations for the method of moments can be derived from the transport equation for the number density and can be written as [137]

$$\frac{\partial M_r}{\partial t} + \frac{\partial (u_i M_r)}{\partial x_i} = \frac{\partial}{\partial x_i}\sum_{j=1}^{\infty} D_{p,j}\frac{\partial (m_j^r N_j)}{\partial x_i} + \frac{\partial}{\partial x_i}\frac{\nu M_r}{T}\frac{\partial T}{\partial x_i} + M_r^{\text{source}} \quad . \tag{4.27}$$

In Eq.(4.27) the second term on the RHS is the thermophoretic diffusion term which is the diffusion of small particles due to a temperature gradient [137, 138]. M_r^{source} is the source term for moment M_r, which is obtained from adding the moment sources due to nucleation, coagulation/aggregation and surface reactions, which have been detailed earlier.

A new quantity is defined as a mass-based moment $M_{mr} = M_r/\rho$, where ρ is the density of the gas-phase mixture. Substituting this into Eq.(4.27) results in

$$\frac{\partial \rho M_{mr}}{\partial t} + \frac{\partial (u_i \rho M_{mr})}{\partial x_i} = \frac{\partial}{\partial x_i}\left(\sum_{j=1}^{\infty} D_{p,j} \frac{\partial \left(\rho (m_j^r N_j) \right) / \rho}{\partial x_i} \right) + \frac{\partial}{\partial x_i}\left[\frac{\mu M_{mr}}{T} \frac{\partial T}{\partial x_i} \right] + M_r^{\text{source}}. \tag{4.28}$$

It is expected that in high Reynolds number turbulent flows the thermophoretic diffusion and differential diffusion of the particles can be neglected [132]. Reynolds averaging of Eq.(4.28) then leads to

$$\frac{\partial \langle \rho \rangle \widetilde{M_{mr}}}{\partial t} + \frac{\partial (\langle \rho \rangle \widetilde{u_i} \widetilde{M_{mr}})}{\partial x_i} = -\frac{\partial (\langle \rho \rangle \widetilde{u_i'' M_{mr}''})}{\partial x_i} + \frac{\partial}{\partial x_i}\left[D_{p1} \frac{\partial (\langle \rho \rangle \widetilde{M_{m,r-\delta}})}{\partial x_i} \right] + \langle \rho \rangle \widetilde{M_{mr}^{\text{source}}} \tag{4.29}$$

The first term on the RHS of Eq.(4.29) is turbulent diffusion while the second term is the Fickian diffusion discussed earlier. The term $\langle \rho \rangle \widetilde{M_{mr}^{\text{source}}}$ includes contributions from nucleation, coagulation, aggregation and surface reaction as also discussed in earlier sections.

Using Eq.(4.29) it should be possible to solve for the soot moments using standard RAS methods described earlier (Chapter 2). However, the closure problems associated with modeling chemical source terms and turbulent diffusion of scalars is also present in

the case of transported moments. Thus it is desirable to formulate a transported PDF approach for the moment equation 4.29.

4.6.1 Turbulent Closure

In principle, a mass density function (MDF), based on chemical species and the PSDF can be formulated as

$$\mathcal{F}(Y_1, Y_2, \ldots, Y_S, h, N_1, N_2, \ldots; \underline{\mathbf{x}}, t), \tag{4.30}$$

where Y_i is the mass fraction of gaseous species i, h is the absolute enthalpy, and N_j is the number density of soot particles of size class j. However, this approach is impractical due to the number of size classes needed to resolve the PSDF accurately. Following the approach of Balthasar et al. [139] and Lindstedt and Louloudi [132], if the particles of all size classes travel with the same velocity as the gas phase, then an MDF based on the moments of the PSDF can be written as,

$$\mathcal{F}(Y_1, Y_2, \ldots, Y_S, h, M_0, M_1, \ldots; \underline{\mathbf{x}}, t) \quad , \tag{4.31}$$

where M_r represents the r^{th} concentration moment (of soot particles). The transport equation of such an MDF is similar to that discussed earlier (see Section 2.3.2):

$$\frac{\partial \mathcal{F}}{\partial t} + \frac{\partial}{\partial x_i}\left[\widetilde{u}_i \mathcal{F}\right] + \frac{\partial}{\partial \psi_s}\left[S_{\text{reaction}}(\underline{\psi})\mathcal{F}\right] = \frac{\partial}{\partial x_i}\left[\Gamma_t \frac{\partial \mathcal{F}}{\partial x_i}\right] + F_{\text{mix}} \quad , \tag{4.32}$$

where $\mathcal{F}$ is the joint composition PDF including soot moments.

Balthasar et al. [139] derived the consistency conditions for different mixing models and showed that the IEM, CD and EMST models can be used directly to "mix" the soot moments. However, soot particles are defined when they attain characteristics that are different from the gas phase. This implies that soot cannot "mix" at the molecular level. Thus, even though mixing models can be applied to soot PSDF moments, it does not appear physically plausible and hence no mixing of soot moments is carried out here. In the current work, the soot moments M_r with $r = 0, 1, 2, 3, 4, 5$ will be used.

4.7 Summary

In this chapter, an overview of soot models used in the current study has been given. Various physical processes involved in soot formation have been discussed. Soot modeling approaches have been identified, followed by a detailed discussion of the method of moments. Soot radiative property models and assumptions used in the current study have also been outlined. Finally, extension of the transported PDF methods to handle TCI in soot formation is discussed.

Chapter 5

Assessment in Laminar Flames

5.1 Introduction

To make progress in soot modeling for luminous turbulent flames, reaction mechanisms should be established and validated systematically in configurations where the confounding effects of TCI and TRI are absent. To this end, a comprehensive modeling study of soot formation in laminar flames has been performed. The scope is limited to atmospheric-pressure ethylene-air flames and to soot modeling based on a method of moments [123]. Both premixed flames and opposed-flow diffusion flames are considered with variations in gas-phase mechanisms and soot model parameters.

Principal goals of this chapter are i) to systematically evaluate parameters in soot submodels combined with different gas-phase mechanisms available in the literature; ii) to identify key sensitivities in these models; and iii) to establish guidelines for soot modeling in turbulent flames.

5.2 Physical models and numerical methods

5.2.1 Gas-phase Mechanisms

Seven gas-phase mechanisms have been evaluated (Table 5.1). The 100-species ethylene mechanism (ABF100) proposed by Appel, Bockhorn and Frenklach [15] is modified from the 99-species mechanism (WF99) proposed by Wang and Frenklach [105];

Table 5.1 Gas-phase reaction mechanisms.

Name	# of Species	# of Reactions	Ref., Remark
WF99	99	533	[105]
ABF100	100	542	[15]
QLY70	70	463	[140]
QLY33	33	205	[140] Reduced by DRG [141]
WI46	46	235	[143]
ABF31	31	179	Retain species common to ABF100 and QLY33
LVW19	19	36	[144]

both of these include species up to four-ring polyaromatic hydrocarbons (PAHs). Qin et al. [140] proposed a 70-species mechanism (QLY70) that includes species up to benzene. The QLY70 mechanism was reduced by Law [141] to a 33-species mechanism (QLY33) using the directed-relational-graph (DRG) method. MECHMOD [142] was used to reduce ABF100 to a 31-species mechanism (ABF31) that contains all the species common to ABF100 and QLY33. Williams and coworkers [143] developed an ethylene mechanism that contains 46 species (WI46). Li, Varatharajan and Williams [144] proposed a 19-species mechanism (LVW19) that contains 36 one-way reactions. All of these mechanisms contain only elementary reactions with no algebraic constraints. The author is not aware of previous application of QLY70, WI46, ABF31 or LVW19 to soot modeling.

5.2.2 Soot models

Two different nucleation mechanisms have been evaluated. Frenklach and co-workers proposed PAH-based nucleation mechanisms [104], while Lindstedt and co-workers used an approach based on acetylene concentration [122, 132]. The author is not aware of previous applications of the acetylene-based nucleation model to premixed flames. PAH-based nucleation mechanisms inherently require use of large gas-phase reaction mechanisms. Here soot coagulation is considered in free-molecular, continuum and transition regimes.

Soot surface growth models have been an active area of research for several decades [2]. Frenklach and Wang [104, 107] proposed chemical similarity, which postulates that chemical reactions taking place on the soot particle surface are analogous to those for large PAH molecules [107]. The surface-HACA mechanism is consistent with the findings of Harris and Weiner [112], who identified that acetylene dominates surface growth in their flames. Soot surface oxidation is via attack by OH radicals and oxygen [120]. Here the surface-HACA mechanism has been used [104]. A key element of that mechanism is that surface radicals are completely depleted during the acetylene addition step. Wang et al. [119] reported that this mechanism underpredicts soot by an order of magnitude in opposed-flow diffusion flames. They reported improved agreement with experiments with surface radicals conserved during the acetylene addition step. They also noted that reality probably lies somewhere between the two extremes of complete depletion and complete conservation of radical surface sites. The two extremes are considered here.

The surface reaction rate due to gaseous species (growth or oxidation) for a soot moment r can be written as,

$$W_r^{surf} = k_{sg} C_g \alpha \chi_s M_0 \sum_{k=0}^{r-1} \binom{r}{k} \Delta m^{r-k} \mu_{r+2/3} \tag{5.1}$$

where k_{sg} is the kinetic rate coefficient for reaction with gas g, C_g is the molar concentration of the gas species, α is a steric factor, χ_s is the nominal number density of surface radical sites, Δm is the change in soot mass due to the reaction [104] and μ_p is the reduced soot moment. The factor α is the fraction of the surface sites available for chemical reactions; it was introduced by Frenklach and Wang [107] to account for differences in soot surface growth rates with temperature as a result of structural changes. The functional form for α has evolved from constant values [104, 106] to a temperature-dependent expression used by Appel, Bockhorn and Frenklach [15]. Here two different values of α are considered: $\alpha = 1$ (all the soot surface sites are available for reaction) and $\alpha = \alpha_{\mathrm{ABF00}}$, corresponding to the functional form introduced by Appel, Bockhorn and Frenklach [15]. The latter includes a dependence on soot particle size as well as temperature. The authors are not aware of previous application of α_{ABF00} to laminar opposed-flow diffusion flames. The importance of PAH condensation on soot surface growth also has been a much-researched topic [145], and a model for that process is included in the method of moments whenever PAH molecules are present in the gas-phase mechanism. The principal model variants considered in this study are given in Table 5.2.

Table 5.2 Soot submodel variants studied

Submodel	Variants	Independent values possible	Reference
Nucleation	C_2H_2 , PAH	2	[122], [104]
Coagulation	Transition Regime	1	[123]
Surface radicals	Depleted, Conserved	2	[15], [119]
Surface reactivity parameter α	1,α_{ABF00}	2	[15]
PAH condensation	Yes, No	2	[123]

5.2.3 Numerical tools

The laminar flames have been simulated using PREMIX [146] and OPPDIF [147]. Species consumption/creation due to reactions of gas-phase with soot is included. Both codes have been modified to handle soot moments [15, 119] as additional scalars. The molecular transport properties and gas-phase kinetics have been implemented using TRANSPORT [148] and CHEMKIN-II [149], respectively. Mixture-averaged diffusion properties are used for the gas-phase species. Differential and thermophoretic diffusion are included for soot moments as in [15, 119]. The thermodiffusion of gas-phase species was neglected. The soot moments are modeled based on the average number of carbon atoms present per unit volume. This implies that the higher moments attain very large values. Hence, scaling is necessary to obtain stable numerical solutions. Here transport equations are solved for the natural logarithms of the soot moments. Achieving convergence with PREMIX was relatively straightforward. OPPDIF was more problematic.

Table 5.3 Laminar flames modeled.

Name	Type	Ref.	Remark
XSF97_1	Premixed	[116]	C/O = 0.78
XSF97_2	Premixed	[116]	C/O = 0.88
XSF97_3	Premixed	[116]	C/O = 0.98
ZYW03_1	Premixed	[150]	C/O = 0.69
WDS96_1	Diffusion	[119]	$a = 117/\text{s}$
WDS96_2	Diffusion	[119]	$a = 79/\text{s}$
HC01_1	Diffusion	[151]	
HC01_2	Diffusion	[151]	

There numerical convergence was obtained by gradually ramping up the soot moment source terms over time until a converged steady-state solution was obtained.

5.3 Flame configurations

Eight flames are included in the present study (Table 5.3).

5.3.1 Laminar premixed flames

Steady, one-dimensional, burner-stabilized ethylene/air flames have been modeled. In all cases, the measured temperature profiles have been prescribed in PREMIX. Xu, Sunderland and Faeth [116] measured temperature, species and soot volume fractions for different C/O ratios (equivalence ratios). These flames were studied by Appel, Bockhorn and Frenklach [15]. Here three of these flames have been modeled. For a similar configuration, Zhao et al. [150] reported PSDF, soot volume fraction and temperature profiles. This flame was simulated by Singh et al. [152] using a different soot-particle dynamics model.

5.3.2 Laminar diffusion flames

In contrast to premixed flames, diffusion flames have strongly oxidizing regions, thereby emphasizing different physics in the models. Wang et al. [119] studied four opposed-flow ethylene flames with different strain rates, a, and reported velocity and soot-volume-fraction profiles. They modeled the flames using a method of moments, with surface HACA for soot growth. They also explored sensitivity of computed temperature profiles to thermal radiation (using an optically thin model) and found that temperatures dropped by less than 1 K over the entire domain. Here, two of these flames are modeled including solving the energy (T) equation, with no radiation correction. In another study, Hwang and Chung [151] studied opposed-flow diffusion flames, including oxygen-enriched flames. They proposed different rate coefficients for the surface HACA mechanism. Two of their flames (those having oxygen concentrations similar to standard air) are simulated in the current study.

5.4 Results and discussion

5.4.1 Gas-phase species

Acetylene is a key species in soot models. Computed and measured C_2H_2 profiles for the XSF97_2 flame are shown in Fig. 5.1. Significant under-prediction of C_2H_2 and soot were found in all flames for WI46 and LVW19 regardless of the nucleation and surface growth parameters. Based on this, the WI46 and LVW19 mechanisms were removed from further consideration.

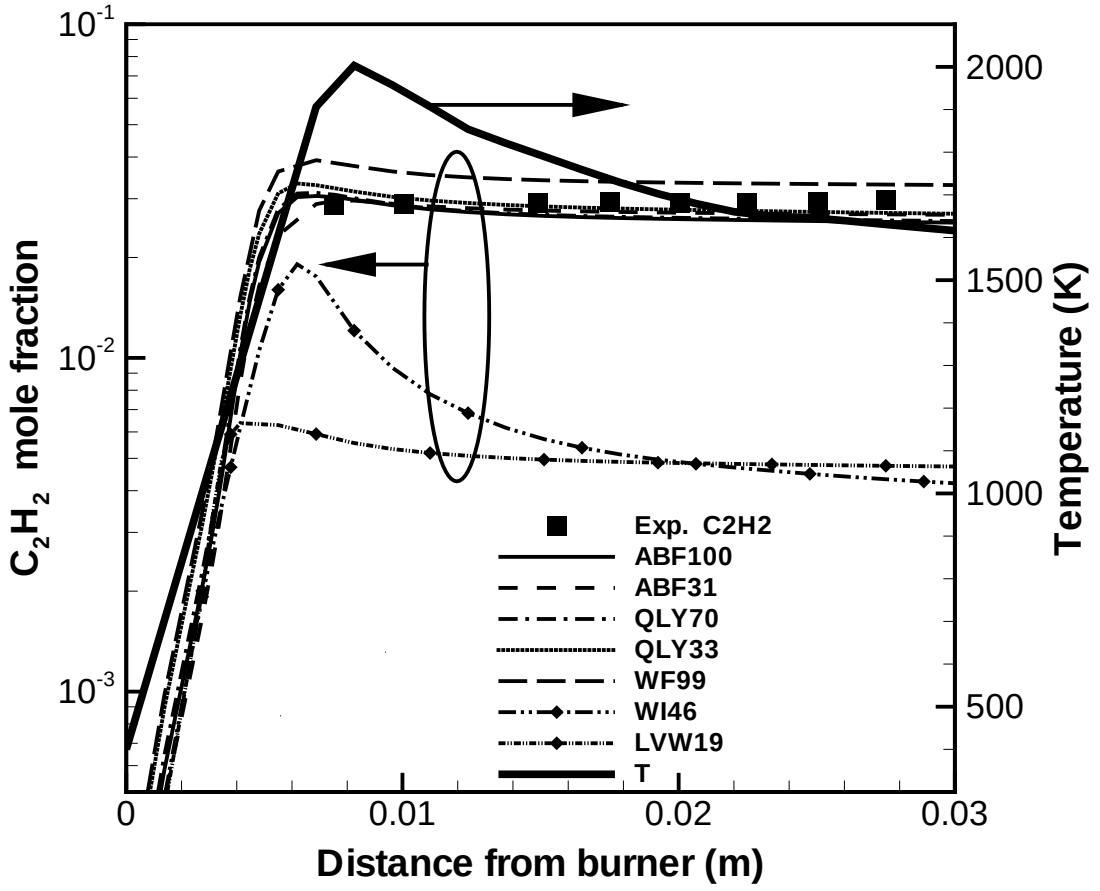

Figure. 5.1 Computed and measured C_2H_2 mole fraction profiles for the XSF97_2 premixed flame. The temperature profile is also shown.

The combinations of gas-phase mechanisms and soot submodels for nucleation, PAH condensation and surface growth parameters for the remaining comparisons are shown in Table 5.4. For example, the only difference between Model 1 and Model 17 is that PAH condensation is considered in Model 1 and is neglected in Model 17. Similarly the difference between Model 17 and Model 18 is that surface radicals are depleted in Model 17 and are conserved in Model 18.

5.4.2 Laminar premixed flame structure

Computed flame structures for flames XSF97_1, XSF97_2 and XSF97_3 are similar to those reported in earlier studies [15]. Typical computed and measured species and soot volume fractions for several models are shown in Figs. 5.1 and 5.2. For the ZYW03_1 flame, measured profiles had to be shifted 3 mm upstream towards the burner to obtain a good match with experiments. This is consistent with the findings of Singh et al. [152]. Comparisons of individual terms in the soot moment equations reveal that the surface reaction rates are much more important than nucleation rates (not shown). This implies that the overall soot yield should be relatively insensitive to the nucleation submodel (PAH-based versus acetylene-based), and this is borne out in the results. The first six soot moments have been retained here. Computed soot volume fractions with three moments differ little from the six-moment results. Therefore, only three soot moments have been retained for the diffusion flame calculations.

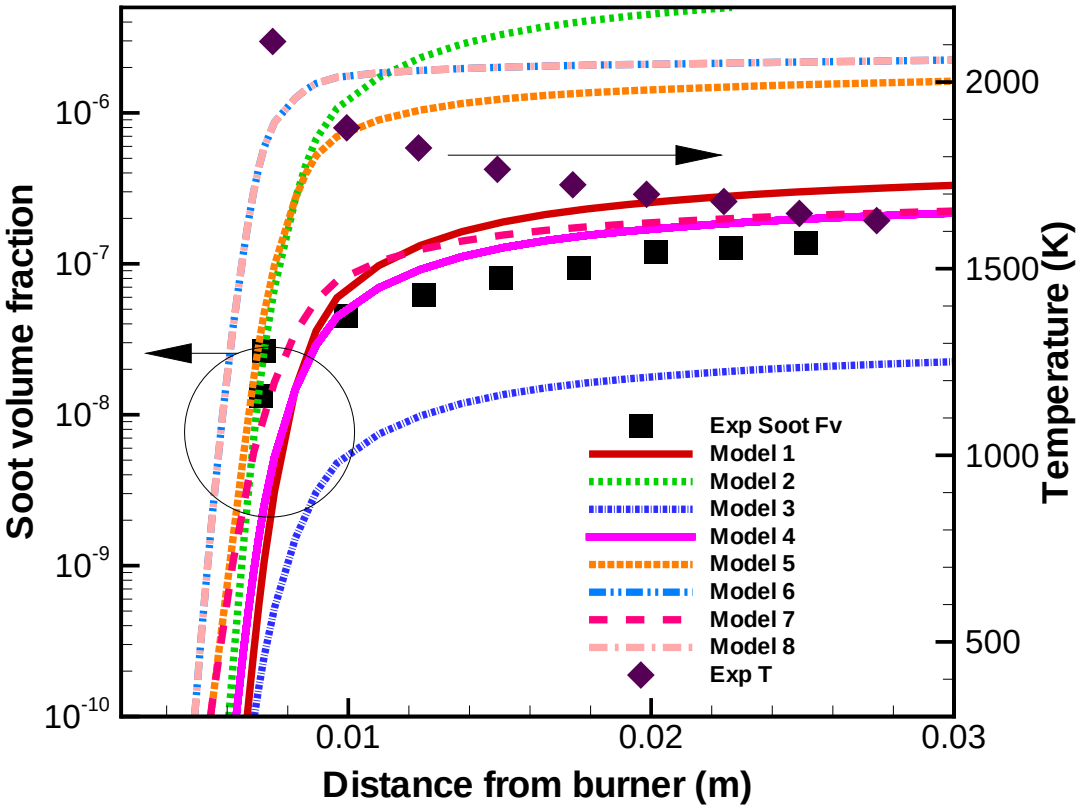

Figure. 5.2 Computed and measured soot volume fractions with different models for premixed flame XSF97_1.

5.4.3 Laminar diffusion flame structure

Following an approach similar to that reported in [119], boundary conditions were modified slightly to line up computed velocity profiles with experimental measurements. This should have negligible influence on the main mixing zone. Computed and measured velocity profiles for flames WDS96_1 and WDS96_2 are in good agreement (Fig. 5.3). Velocity profiles are not available for flames HC01_1 and HC01_2 . However, the computed and measured stagnation point locations are in good agreement (not shown).

5.4.4 Soot volume fractions

Overall flame structures are well captured for both premixed and diffusion flames. To compare the performance of the many model variants, the principal figure-of-merit is taken to be the soot volume fraction at one point in the flame. For diffusion flames, this is simply the peak value. For premixed flames, it is the value at the last product-side data point reported in the experiments. Ratios of computed-to-measured soot volume fractions for 36 model variations are reported in Table 5.4. The ideal model would have values close to unity for all eight flames. To facilitate interpretation of Table 5.4, ratios greater than unity are in bold font, and ratios in the range 0.2 to 5.0 are shaded and bold. This choice of range is somewhat arbitrary, but serves to sort those models that do not perform well across a wide range of flames (rows with few or no shaded entries- e.g. Model 19) from those that are promising (rows with many shaded entries- e.g., Model 33). A few highlights are emphasized here.

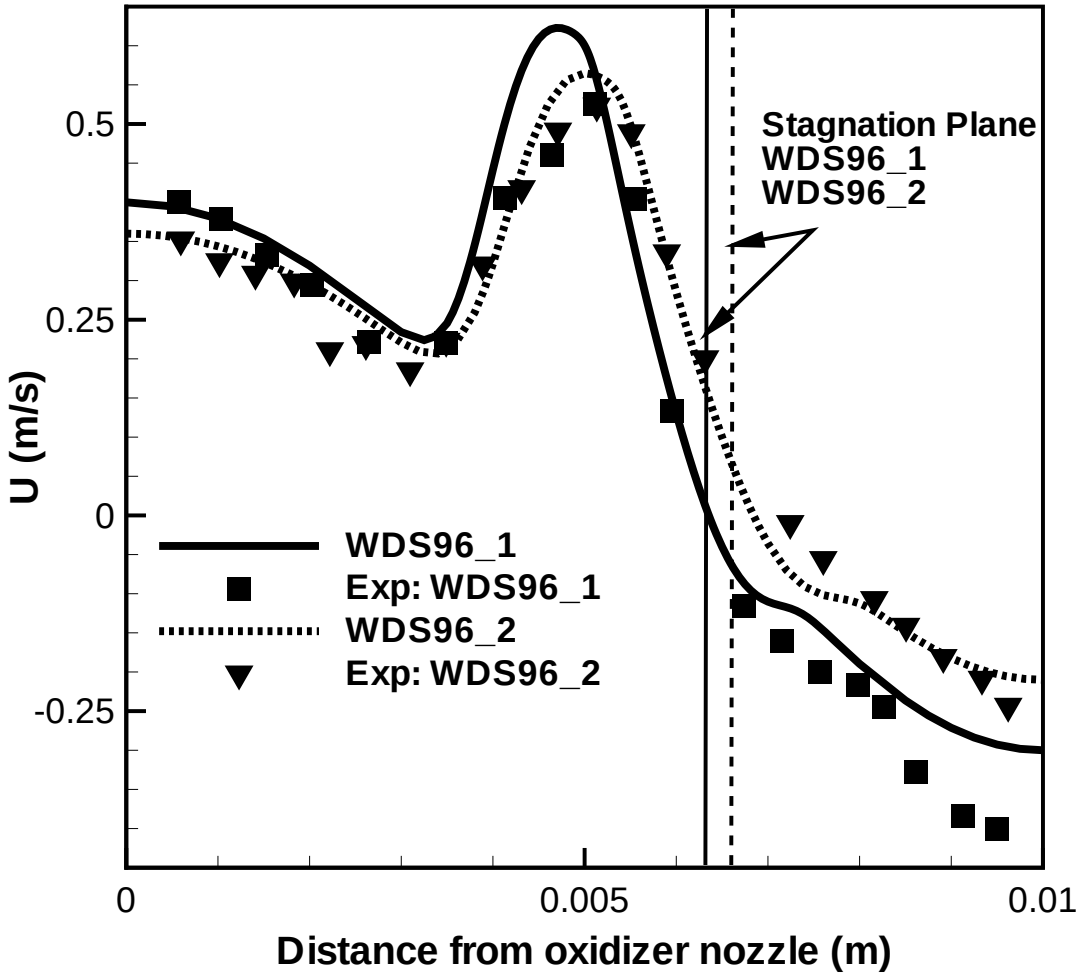

Figure. 5.3 Computed (lines) and measured (symbols) velocity profiles for WDS96_1 and WDS96_2 diffusion flames.

Table 5.4 Ratios of computedto measured peak soot volume fractions for 36 models in eight flames (Table 5.3). Shaded entries correspond to satisfactory predictions.

Model parameters						Ratio of computed to measured (peak) soot volume fractions							
						Diffusion flames				Premixed flames			
Model	Chemistry	Nucl. Mech	PAH Cond.	Surf. Factor	Surface Radicals	WDS96_1	WDS96_2	HC01_1	HC01_2	XSF97_1	XSF97_2	XSF97_3	ZYW03_1
1	WF99	PAH	Y	1.0	Dep	0.0036	0.0027	0.023	0.12	**0.99**	**1.7**	0.10	0.00034
2	WF99	PAH	Y	1.0	Con	**0.99**	**0.79**	**26**	**19**	**13**	**35**	**3.8**	0.0066
3	WF99	PAH	Y	ABF	Dep	0.00068	0.00056	0.0031	0.0056	0.075	0.13	0.10	0.00028
4	WF99	PAH	Y	ABF	Con	0.056	0.043	**0.25**	**0.67**	**0.58**	**1.5**	**0.46**	0.0026
5	WF99	C2H2	N	1.0	Dep	**1.3**	**0.70**	**1.5**	**2.3**	**11**	**5.0**	**0.24**	0.040
6	WF99	C2H2	N	1.0	Con	**46**	**27**	**30**	**19**	**16**	**6.6**	**5.5**	**1.6**
7	WF99	C2H2	N	ABF	Dep	0.11	0.062	0.082	0.041	**1.5**	**0.75**	0.069	0.025
8	WF99	C2H2	N	ABF	Con	**4.6**	**2.6**	**3.6**	**2.9**	**9.6**	**5.0**	**1.8**	**0.38**
9	ABF100	PAH	Y	1.0	Dep	**0.62**	**0.45**	**1.9**	**2.6**	**8.4**	**3.8**	**0.33**	0.017
10	ABF100	PAH	Y	1.0	Con	**65**	**41**	**77**	**27**	**97**	**54**	**11**	**0.24**
11	ABF100	PAH	Y	ABF	Dep	0.18	0.15	**0.66**	**0.90**	**0.62**	**0.33**	0.13	0.013
12	ABF100	PAH	Y	ABF	Con	**5.0**	**3.6**	**47**	**84**	**5.0**	**3.1**	**1.2**	0.081
13	ABF100	C2H2	N	1.0	Dep	**1.2**	**0.68**	**1.4**	**2.3**	**11**	**4.6**	**0.23**	0.033
14	ABF100	C2H2	N	1.0	Con	**45**	**24**	**30**	**19**	**16**	**5.8**	**5.2**	**1.1**
15	ABF100	C2H2	N	ABF	Dep	0.11	0.060	0.080	0.041	**1.7**	0.69	0.067	0.021
16	ABF100	C2H2	N	ABF	Con	**4.3**	**2.4**	**3.7**	**2.8**	**9.5**	**4.5**	**1.6**	**0.30**
17	WF99	PAH	N	1.0	Dep	0.0035	0.0026	0.021	0.11	**0.99**	**1.7**	0.09	0.00031
18	WF99	PAH	N	1.0	Con	**0.99**	**0.78**	**25**	**18**	**13**	**35**	**3.8**	0.0065
19	WF99	PAH	N	ABF	Dep	0.00060	0.00047	0.0022	0.0039	0.075	0.12	0.027	0.00025
20	WF99	PAH	N	ABF	Con	0.055	0.042	**0.24**	**0.64**	**0.58**	**1.5**	**0.45**	0.0025
21	ABF100	PAH	N	1.0	Dep	**0.45**	**0.29**	**0.95**	**1.6**	**8.3**	**3.7**	**0.25**	**0.30**
22	ABF100	PAH	N	1.0	Con	**60**	**36**	**48**	**5.8**	**96**	**54**	**11**	**0.23**
23	ABF100	PAH	N	ABF	Dep	0.092	0.069	**0.20**	**0.20**	**0.59**	**0.31**	0.087	0.010
24	ABF100	PAH	N	ABF	Con	**4.3**	**2.9**	**11**	**10**	**5.0**	**3.0**	**1.1**	0.076
25	QLY70	C2H2	N	1.0	Dep	**1.0**	**0.90**	**0.83**	**1.2**	**13**	**6.1**	**0.26**	0.12
26	QLY70	C2H2	N	1.0	Con	**44**	**29**	**23**	**13**	**17**	**7.8**	**5.8**	**5.0**
27	QLY70	C2H2	N	ABF	Dep	0.083	0.060	0.051	0.028	**2.0**	**0.9**	0.072	0.059
28	QLY70	C2H2	N	ABF	Con	**4.1**	**2.9**	**2.9**	**1.9**	**11**	**5.9**	**1.7**	**1.04**
29	QLY33	C2H2	N	1.0	Dep	**2.2**	**2.0**	**2.1**	**1.9**	**11**	**6.1**	**0.35**	**0.20**
30	QLY33	C2H2	N	1.0	Con	**57**	**36**	**34**	**11**	**16**	**6.6**	**5.4**	**7.9**
31	QLY33	C2H2	N	ABF	Dep	0.16	0.13	0.12	0.053	**2.1**	**0.99**	0.092	0.088
32	QLY33	C2H2	N	ABF	Con	**9.6**	**6.9**	**7.9**	**4.4**	**11**	**5.9**	**3.6**	**1.9**
33	ABF31	C2H2	N	1.0	Dep	**2.3**	**2.1**	**2.9**	**2.0**	**9.9**	**4.8**	**0.21**	0.13
34	ABF31	C2H2	N	1.0	Con	**54**	**36**	**35**	**16**	**13**	**6.2**	**4.5**	**3.8**
35	ABF31	C2H2	N	ABF	Dep	0.19	0.15	0.17	0.066	**1.6**	**0.75**	0.062	0.060
36	ABF31	C2H2	N	ABF	Con	**9.2**	**7.0**	**8.5**	**4.2**	**8.3**	**4.4**	**1.6**	**0.67**

Model 11 was proposed by Appel, Bockhorn and Frenklach [15] and applied to flames XSF97_1, XSF97_2 and XSF97_3. Soot volume fractions for XSF97_3 are under-predicted by Model 11, as reported in [15]. However, a variant that conserves surface radicals (Model 12) predicts the soot volume fraction well.

Examples of computed and measured soot volume fractions for a diffusion flame are provided in Fig. 5.4. Models 1 and 2 were used by Wang et al. [119], and their results are reproduced here. Models 9, 11, 13, 15 and 16 also are shown in Fig. 5.4.

Figure 5.5 compares results from a C_2H_2 -based nucleation model (Model 16) with those from an otherwise identical model that uses PAH-based nucleation (Model 24) for a premixed flame and a diffusion flame. For the premixed flame (Fig. 5.5a), the predicted number density with C_2H_2 -based nucleation is approximately a factor of two higher, and the soot volume fractions are also higher, although by a lesser factor. On the other hand, the soot volume fraction prediction in the diffusion flame is almost independent of the nucleation mechanism, as observed by Leung, Lindstedt and Jones [122]. This implies that most of the soot production in opposed-flow diffusion flames results from surface reactions.

The effects of PAH condensation and surface reactions are shown in Fig. 5.6. The overall contribution of PAH condensation is relatively small compared to surface reactions for the diffusion flames. This is true even when surface radicals are depleted. The effects of PAH condensation for premixed flames are even smaller (Table 5.4).

Models 11 and 15 (surface radicals depleted) tend to under-predict soot by approximately one order of magnitude, while Models 12 and 16 (surface radicals conserved) over-predict soot in most flames by factors of four-to-five (Table 5.4). This suggests that

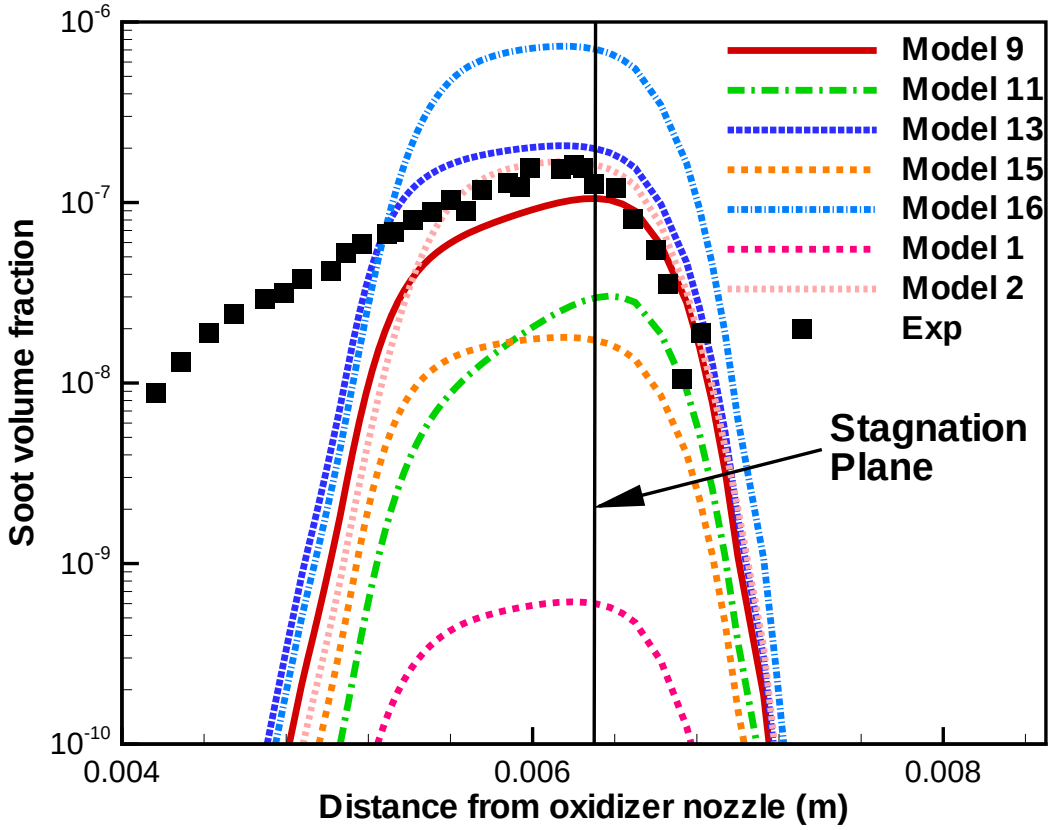

Figure. 5.4 Computed and measured soot volume fraction profiles with different models for WDS96_1 flame.

something between complete depletion and full conservation might be appropriate. A function might be devised that depends on local conditions, similar to what has been done with the steric factor α [15].

The influence of gas-phase reaction mechanisms on soot prediction is strong. For example, Model 9 yields good predictions for seven out of eight flames studied. However, ABF100 would be computationally prohibitive in turbulent flame simulations. Models 8, 16 and 28 give reasonable predictions in six or seven flames out of eight. In fact if the acceptance criterion were extended to a full order of magnitude (0.1–10.0), these models would be shaded for all flames. These models employ acetylene-based nucleation and do not include PAH condensation. This suggests that it may not be necessary to carry gas-phase species up to PAH's.

5.5 Summary

To make progress in soot modeling for luminous turbulent flames, it is important to develop and validate reaction mechanisms/soot models over a broad range of conditions and without the additional complexities of turbulence. Here, seven different ethylene-air mechanisms have been studied to determine their suitability for soot modeling, together with a method of moments for soot particle dynamics. Sensitivity to key soot model parameters has been explored. The assessment has been performed for eight different laminar flames, including both premixed and diffusion flames.

Computed soot volume fractions are most sensitive to variations in surface growth processes (steric factor α, and conserved versus depleted surface radicals). Soot nucleation also influenced soot yields in premixed flames. Acetylene-based (versus PAH-based)

nucleation generally performed adequately, and PAH condensation does not appear to be essential. This suggests that relatively small gas-phase reaction mechanisms should suffice. A fruitful line of research for soot modeling would be to develop a function that effectively interpolates between complete depletion and full conservation of surface radicals during the C_2H_2 addition step.

While no model gave soot volume fractions within a factor of five from experimental values for all eight flames, several models are within a factor of 10 for all eight flames. Models 29 and 33 appear promising, for example. Here, oxygen-enriched flames have not been considered. In oxygen-enriched flames, the role of PAH has been found to be higher than in the flames considered here [150]. Soot agglomeration into mass fractals also has not been considered; this is known to be a factor in high-pressure flames [127]. It has been shown that method-of-moments has limitations when dealing with bimodal PSDF (e.g., [150]). The effect of alternative particle dynamics models (e.g., sectional methods) has not been studied here. Other fuels also are of interest. These extensions are the subjects of ongoing research.

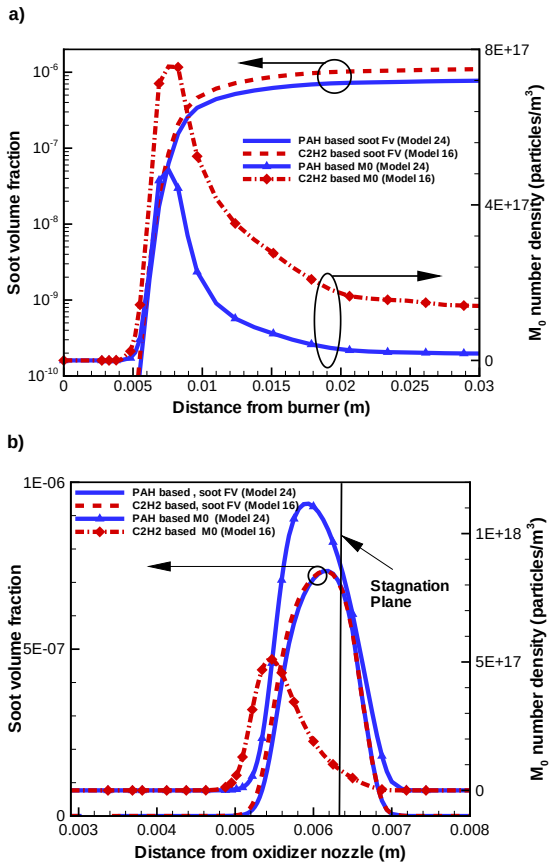

Figure. 5.5 Effect of nucleation submodels: a) XSF97_2 premixed flame.b) WDS96_1 diffusion flame.

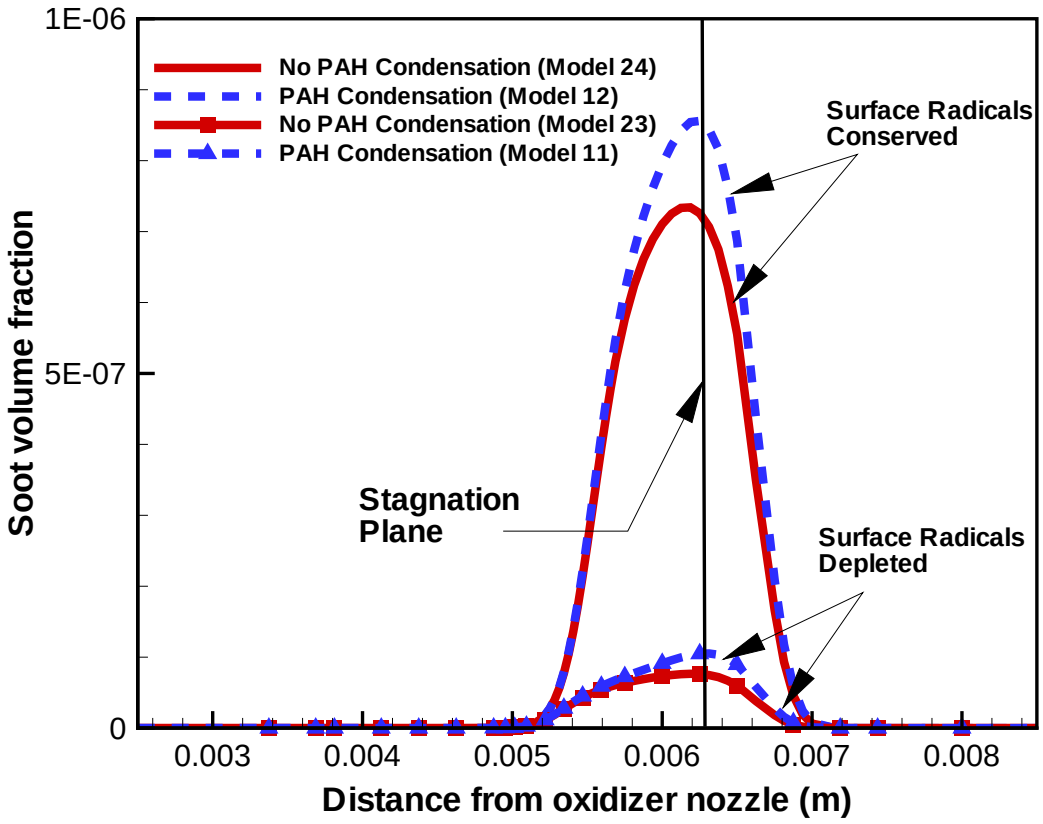

Figure. 5.6 Effect of PAH condensation: WDS96_1 diffusion flame with and without PAH condensation, with different contributions from surface reactions.

Chapter 6

Validation in Turbulent Flames

6.1 Introduction

In order to quantitatively characterize effects of TRI on flame structure and vice-versa, it is important to validate the models used in the current study against experimental measurements. A number of nonpremixed turbulent jet flames have been experimentally investigated by various researchers (see [153] and references therein). These experiments are generally used to understand turbulent combustion and also aid in model development by providing important data for comparison with predictions. Most of the modern combustion measurements use laser diagnostics (scattering and extinction) for various quantities including temperature, species mass-fractions, soot volume fractions etc, [154]. The principal advantage of laser diagnostics is that they are nonintrusive to a large extent. In addition, they also have very rapid response times, thus allowing even transient measurements in turbulent conditions.

However, the main requirement for these techniques is optical access. Thus, if the flames are optically thick, the laser cannot reach "inside" the flames. The measurements of various species or temperature typically use absorption or scattering response in certain spectral ranges [154]. In case of sooting flames, the soot emission, which occurs over a large part of the spectrum, interferes very strongly with the low-intensity scattering measurements typically used for species measurements. For this reason almost no studies

for moderate-to-highly sooting flames report species data (due to very high uncertainty in species measurements).

6.2 Flame Configurations

In this chapter, various turbulent jet-flames are simulated and relevant predictions are compared with data available. The flames operate over a wide range of jet Reynolds numbers with either pure ethylene fuel or a blend of 90% methane–10% ethylene by volume. Each flame simulation is discussed in detail after a brief description of the flame configurations and models used. Table. 6.1 lists the principal flames studied.

Table 6.1 Turbulent flames simulated for validation of the models.

Flame	Name	Fuel	Oxidizer	Jet Reynolds Number	Reference
I	CJ94	C_2H_4	Air	11800	[155]
II	KH87	C_2H_4	Air	15100	[156]
III	ET00_21	Blend	Air	6700	[157]
IV	ET00_30	Blend	30% O_2	6700	[157]
V	ET00_40	Blend	40% O_2	6700	[157]
VI	ET00_55	Blend	55% O_2	6700	[157]

Flames I and II are moderately sooting pure ethylene flames with peak soot volume fraction on the order of 1.5 ppm. Flames III–VI are from a 90% methane–10% ethyelene blend and have much lower sooting propensities. It is expected that the peak soot volume fractions in these flames are on the order of 0.2 ppm, in spite of the fact that the residence times for these flames are much larger compared to flames I and II.

6.3 Model Summary

Table 6.2 lists all the physical/empirical models used for various subprocesses involved in a full turbulent reacting flow simulation. Most of these submodels have some model constants. In the current study, an attempt has been made to keep most all model parameters the same for all the flame simulations, thereby reaching a somewhat unified model for all turbulent reacting flows. Table 6.2 serves as a reference table for all the flames discussed in this chapter. The gas-phase chemistry and soot models were selected based on the study done in Chapter 4. It should be noted that none of the model parameters are "tuned" for any particular flame, and exactly the same models are used for all the flames.

6.4 Flame I (CJ94)

A turbulent jet flame studied experimentally by Coppalle and Joyeux [155] with a jet Reynolds number of $11,800$ has been simulated. The temperature and soot volume fractions were measured simultaneously using two-color pyrometry and extinction measurements, respectively. This flame has been studied numerically by Lindstedt and Louloudi [132] using optically thin radiation. The effect of re-absorption on temperature predictions and soot yield was left as an open question. In addition, their solution method for scalar transport was a parabolic time-marching scheme, which is not generally extendable to arbitrary configurations. Empirical models were used for all the soot subprocesses including surface growth and oxidation.

Table 6.2 All submodels used in the current study.

Quantity	Model	Tunable Parameters	Values	References
Turbulent Reynolds stress	k–ϵ	$C_\mu, C_{\epsilon 1}, C_{\epsilon 2}$	C_μ=0.09, $C_{\epsilon 1}$=1.44, $C_{\epsilon 2}$=1.92 (Standard)	[42]
Turbulent species, enthalpy fluxes	Gradient diffusion + k–ϵ	Turbulent Schmidt (Sc_T) and Prandtl (Pr_T) Numbers	$\mathrm{Sc}_T = 0.7$, $\mathrm{Pr}_T = 1$ (Standard)	[42]
Chemical source terms (closure)	Transported PDF method	Mixing models	EMST ($C_\phi = 2$)	[158]
Gas-phase chemistry	33-species, 205-reactions (QLY33)	**NONE**	-	[140, 141]
Soot Model	Method of moments	Nucleation, Surface Reactions, Radical conservation	Model 32 (Chapter 5)	[159]
Soot scalar source terms (closure)	Transported PDF method	Mixing models	No Mixing	[160]
Gas-phase radiative properties	Line-by-line databases: H_2O ,CO_2	**NONE**	Neglect CO and fuel radiation	[1]
Soot radiative properties	Absorption coefficient based on [89]	Complex index of refraction, Scattering	$m = n(\eta) - ik(\eta)$, Rayleigh scattering (negligible)	[1, 89]
RTE Solver	Full nongray photon Monte Carlo	Cone opening angle, number of rays, energy partitioning	Based on [96] and TPDF settings	[96]
TRI (closure)	Emission and Absorption TRI	Within statistical limits		[96]

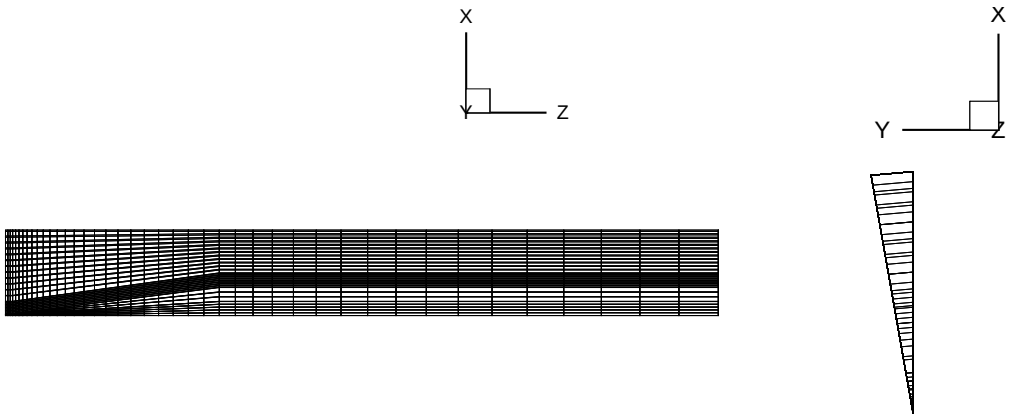

Figure. 6.1 Grid used in turbulent jet flame simulation.

Here an elliptic solution method is employed for scalar transport (including soot moments), which can be easily applied to complex configurations. A weak co-flow is used instead of simulating a jet flame into quiescent air, and a small false pilot is employed to stabilize the flame. The jet diameter is $d_j = 4$ mm with incoming fuel velocity of 29.5 m/s. A three-dimensional wedge-like grid system is employed to simulate the axisymmetric flame by applying periodic boundary conditions on the sides as shown in Fig. 6.1, with a wedge angle of 10°; the dimensions in x- and z- directions are 30 d_j and 250 d_j, respectively. The grid is fine near the fuel jet to accurately resolve large local gradients in the mixing region and coarser in the coflow air region to save computational time. With composition PDF methods, it is found that around 30 particles per cell on average are sufficient to resolve the turbulent fluctuations in the flame [44].

The PMC method is used for radiation modeling, mainly following the approach used in [73]. The rays are traced as cones with 1° opening angles and 200,000 rays are traced per time step. Since the flames are statistically stationary, time-averaged radiative

source terms evaluated for each cell are fed back to the finite volume (FV) code. In traditional FV methods, the residual error diminishes to zero with sufficient number of iterations, and can be used to monitor convergence. However, the residual error in hybrid FV/Monte Carlo method cannot show the same behavior due to presence of statistical noise. Hence, a different metric is generally used to monitor convergence; following the approach of Wang and Modest [73], emission-weighted average temperature (T_e) and volume-averaged root-mean-square (rms) fluctuations ($\left\langle T'' \right\rangle_v$)are used to monitor convergence, i.e.,

$$T_e = \frac{\int_V k_p T^5 dV}{\int_V k_p T^4 dV} \quad \text{and} \quad \left\langle T'' \right\rangle_v = \frac{1}{V} \sum_c \left[\frac{V_c}{\rho_c} \sum_{p \in c} m_p (T_p - T_c)^2 \right]^{1/2} V_c, \tag{6.1}$$

where the outer sum denotes summation over cells, and the inner sum is over particles inside a cell.

6.4.1 Principal Results for Flame I

The simulations are run in a transient fashion until the convergence criteria are no longer changing with time, using a timestep of $\Delta t = 50$ μs. Convergence results are shown in Fig. 6.2 using the PMC as RTE solver, but are similar when using the optically thin approximation. Figure 6.3 shows the converged steady-state contours of the mean temperature and soot volume fraction using the PMC. The contours show reasonable distribution of soot commensurate with the flame structure.

The computed centerline mean temperature profiles obtained without soot radiation, and with soot radiation using either the optically thin approximation or the PMC

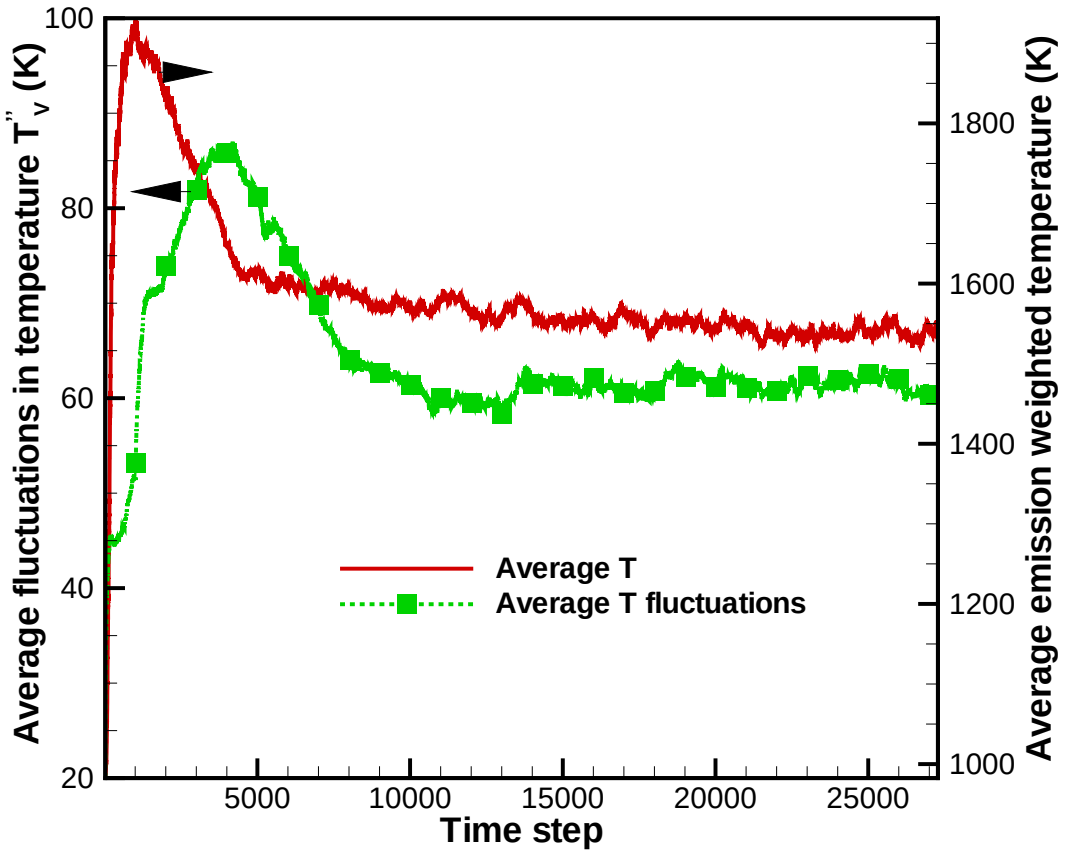

Figure. 6.2 Progress of convergence criteria for PDF/Monte Carlo simulation.

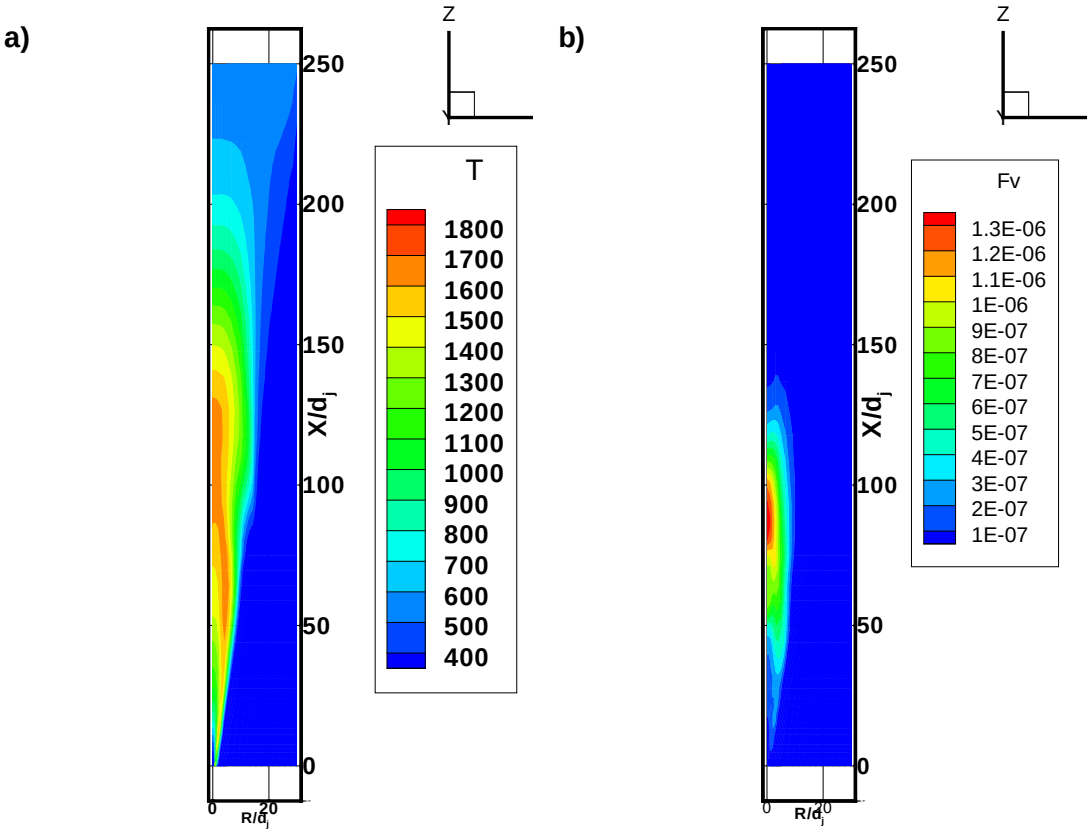

Figure. 6.3 Mean temperature and soot volume fraction contours.

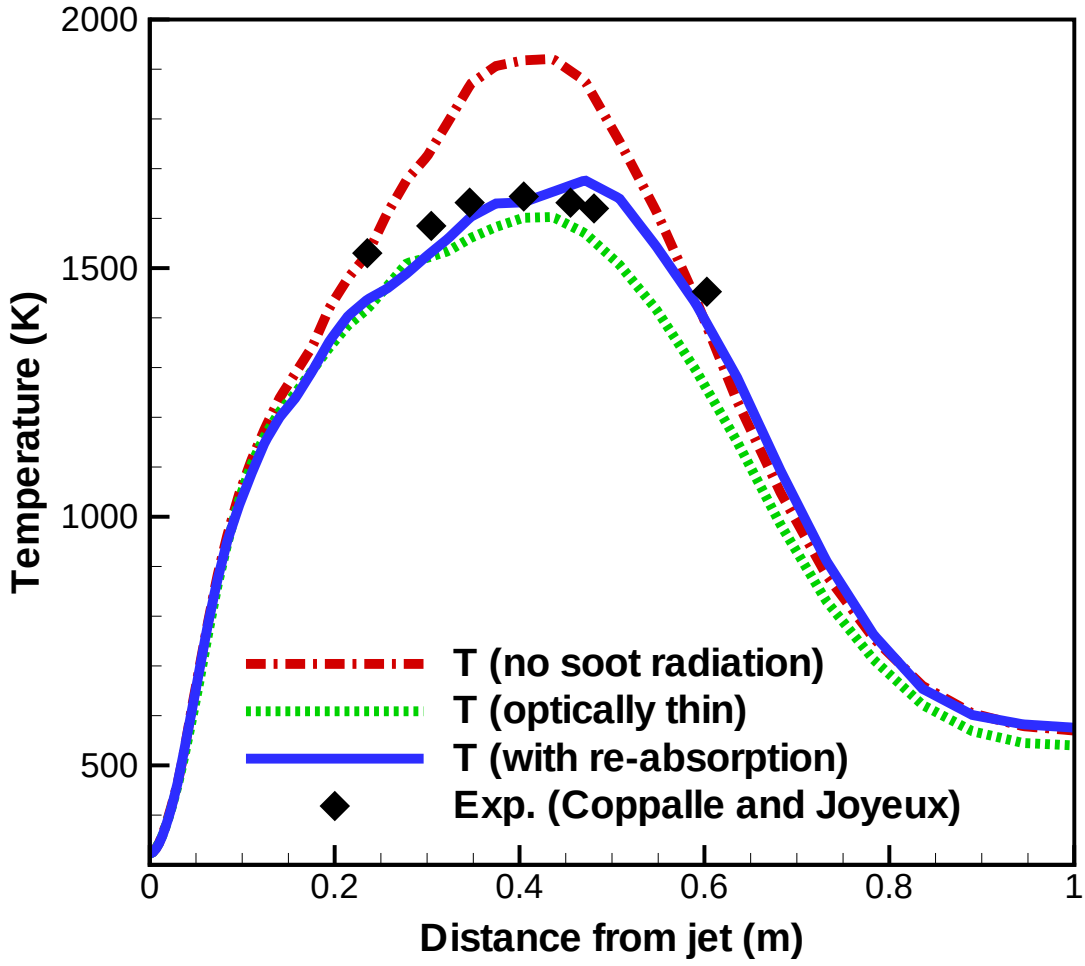

Figure. 6.4 Measured and computed centerline mean temperature profiles using optically thin radiation and PMC method.

are shown in Fig. 6.4. It can be seen that soot radiation has a large effect on the temperatures and, consequently, on the entire flame structure. The peak centerline mean temperature drops by more than 300 K from 1920 K to 1600 K in case of optically thin radiation. Thus, optically thin radiation under-predicts peak temperature compared to the experimentally measured value of 1665 K. Optically thin radiation results also under-predict temperatures in most of the downstream region. This fact has important implications on soot formation and oxidation rates, thereby changing the soot profiles. Using the PMC (thus accounting for re-absorption) results in a peak mean centerline temperature of 1678 K, which is closer to the experimental value. Therefore, accounting for re-absorption is necessary when modeling sooting flames of this size. An important observation is that the change in temperature fields affects the soot levels, which in turn affects the amount of heat radiated from the flame.

The predicted centerline mean soot levels are compared with experiment in Fig. 6.5. It can be seen that the change in flame structure also affects the soot predictions. The peak axial soot volume fraction is slightly lower than experiments when using both optically thin and PMC models. However, considering the ppm levels of soot, the agreement is very encouraging. Re-absorption results in higher temperatures, which increase both surface growth and oxidation rates, and local conditions dictate the net effect on the soot growth rates. In the current flame accounting for re-absorption results in a higher soot formation rate, giving better agreement with experiments. Radial soot volume fractions at two different stations are shown in Fig. 6.6. It can be seen that predictions follow the trend of experiments. At both stations the optically thin radiation model underpredicts

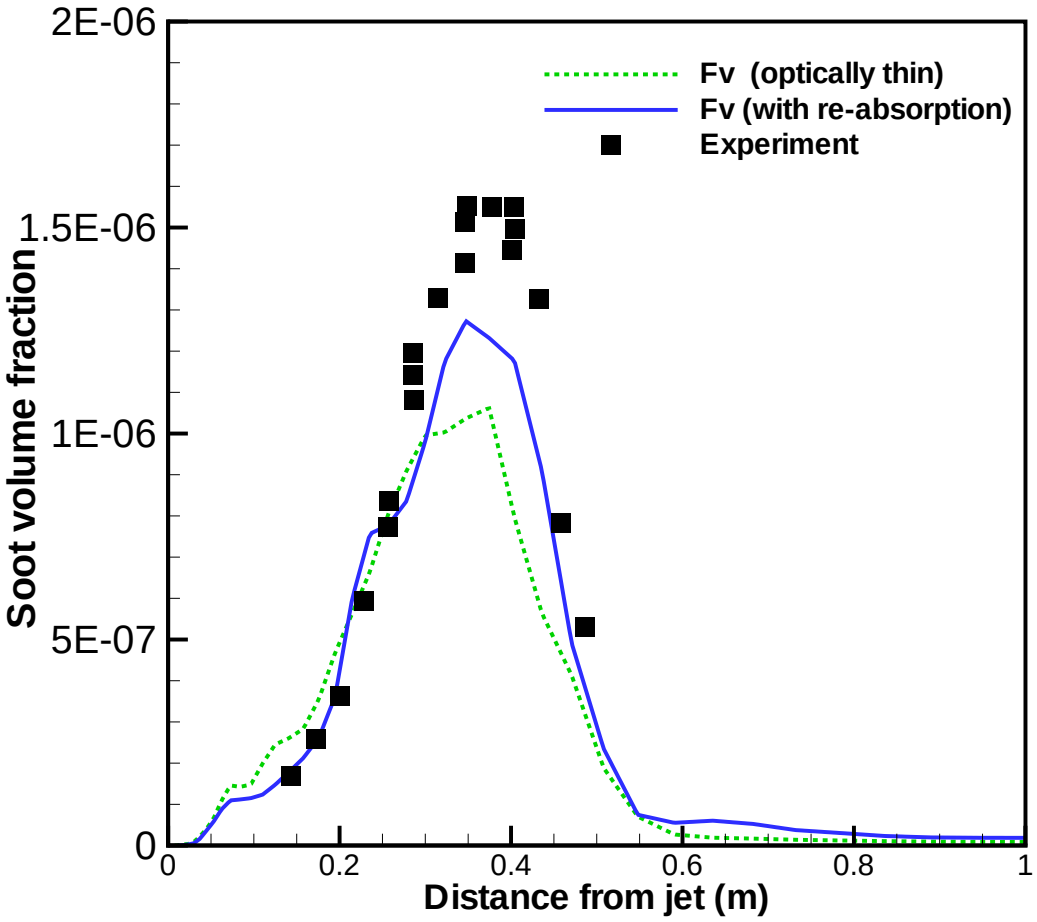

Figure. 6.5 Measured and computed centerline mean soot volume fraction profiles using optically thin radiation and PMC method

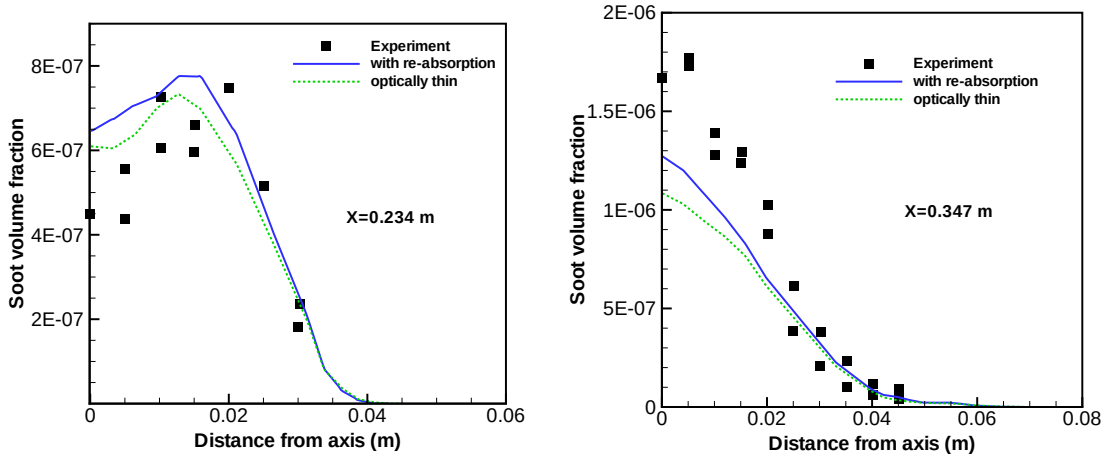

Figure. 6.6 Measured and computed radial soot volume fraction profiles at two axial stations

soot to a greater extent than when accounting for re-absorption. Both models are able to capture the off-center peak location reasonably.

6.5 Flame II (KH87)

Kent and Honnery [156] experimentally studied ethylene/air jet flames of varying Reynolds numbers from ~ 7500 to ~ 15000. Extinction measurements were carried out along secants and radial soot volume fractions were "estimated" using an Abel inversion technique [161]. A consequence of this is that soot volume fractions can have a high degree of uncertainty, at least near the axis of the flame. The degree of uncertainty however, was not quantified. The temperatures were directly measured using uncoated thermocouples and a radiation correction was applied using a surface emissivity of 0.2. They also did a modeling study for these flames using a state-relationship between local mixture-fraction and soot volume-fraction. Even though they reported qualitative agreement, the results did not match well with experimentally measured values for soot

volume fractions. They concluded the study by re-iterating that the time-scales for soot formation are such that a state relationship with local compositions cannot adequately predict soot formation.

The burner consists of cylindrical nozzle of diameter $d_j = 3$ mm. The burner is aligned vertically and fuel is burned in still air. This flame has also been subject to investigation by several authors [132, 156, 162]. Said, Garo and Borghi [162] used a global soot model, with formation and oxidation rates as functions of fuel mass fraction, temperature and intermediate species (OH, CO), respectively. An optically thin radiation model was used to account for radiative losses. An extension of a probabilistic Eulerian-Lagrangian model (PEUL) was used to handle turbulence–chemistry interactions in the soot formation processes [163]. In addition, the prescribed PDF used a conserved scalar approach. They reported good agreement with experiment; however, the soot model cannot be applied to all fuels, and use of optically thin radiation is also questionable. Lindstedt and Louloudi [132] studied the same flame using a composition PDF method, and empirical soot submodels for surface-growth and PAH condensation. They also invoked the optically thin approximation which has been shown to affect the predictions in Flame-I above (Section 6.4.1).

6.5.1 Modeling for Flame II

A mesh similar to that shown in Fig. 6.1 is used for simulating the current flame. A weak co-flow is used instead of simulating a jet flame into quiescent air. Due to very high jet velocity (52.0 m/s), it was found that a false-pilot approach needed either a very broad pilot, or very high pilot velocity to stabilize the flame. Both these approaches result

in additional enthalpy flowing into the computational domain in addition to modifying the jet spreading and flame mixing characteristics upstream. However, in absence of a false pilot, the flame cannot sustain or stabilize itself near the jet exit. To obtain better stability for the flame, equilibrium calculations are performed in a small region near the jet exit up to $x/d_j = 10$. This makes the flame structure immediately near the jet exit purely mixing-controlled, with infinite-rate reactions.

A three-dimensional wedge-like grid system is employed to simulate the axisymmetric flame by applying periodic boundary conditions on the sides as shown in Fig. 6.1, with a wedge angle of 10°; the dimensions in x- and z- directions are 30 d_j and 250 d_j, respectively. The grid is fine near the fuel jet to accurately resolve large local gradients in the mixing region and coarser in the coflow air region to save computational time.The results showed a very strong sensitivity to C_ϕ with predicted temperatures differing by more than 150 K for larger values of C_ϕ. The increased temperatures have a direct effect on the predicted soot volume fractions and hence the radiative losses from the flame. The simulation is run in a transient manner with a timestep of $\Delta t = 1.0 \times 10^{-4}$ s. There are 25–40 particles per cell, and approximately one ray per particle in the PMC method.

6.5.2 Principal Results for Flame II

The converged, steady-state contours of the mean temperature and soot volume fraction are shown in Fig. 6.7. The overall flame structure is commensurate with expected results.

The computed centerline mean temperature profile is compared with the experiments in Fig. 6.8. The computed peak mean temperature is 1850 K which is about

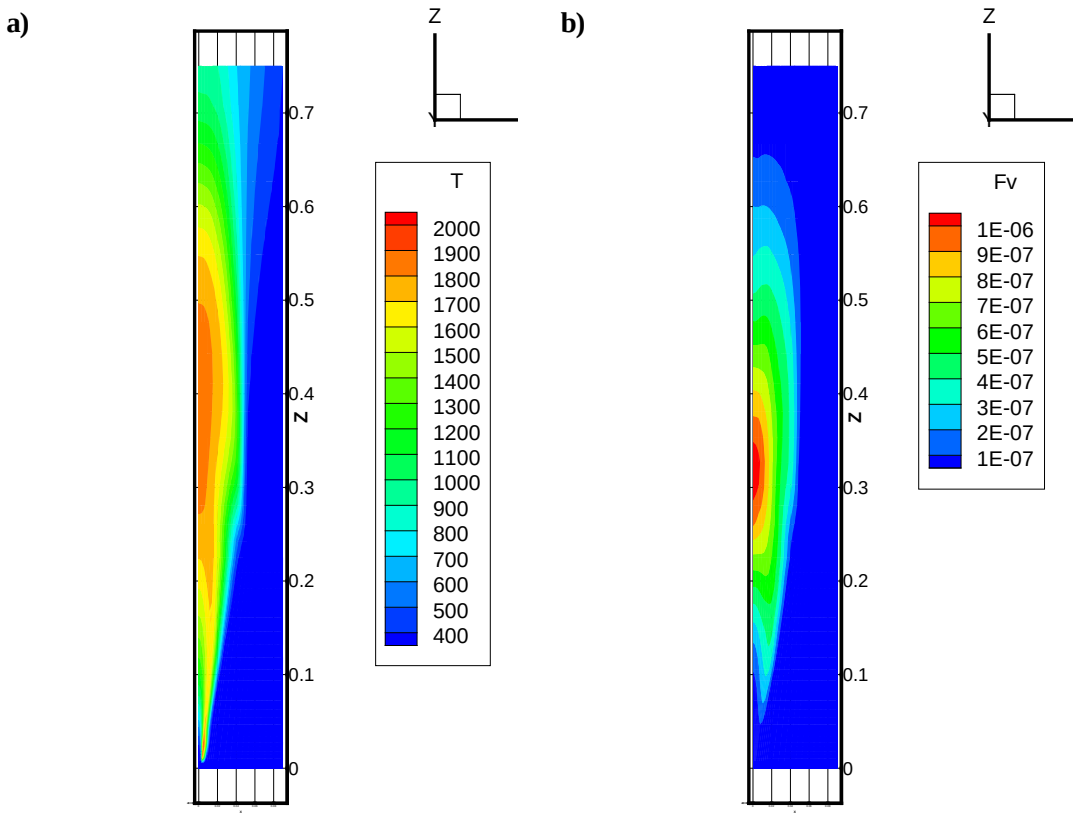

Figure. 6.7 a) Mean temperature and b) soot volume fraction contours for Flame-II.

70 K higher than the experimental peak temperature of 1778 K. As noted in [156], the temperature in the highly sooting region may be measured incorrectly due to presence of soot. Computed axial soot volume fraction is also shown in Fig. 6.8. It can be seen that the discrepancy between computed and measured temperatures is very small in the upstream region, and increases in the region where large amount of soot is present. The overall trend of temperature fall after the peak is captured accurately.

Experimental data in [156] is presented in relationship to the position where maximum laser extinction occurs; that location is denoted by x_m. Table 6.3 lists various quantities obtained in the simulation, compared with the experimental data.

Table 6.3 Comparison between computed and experimental values for various quantities in Flame-II.

Description	Experiment	Computation	Remark
Peak soot location (x_m) (m)	0.345 m	0.328 m	-
Peak temperature location (m)	0.38 m	0.37 m	-
Peak temperature (K)	1778	1850	-
Axial peak soot (ppm)	-	1.05	-

Computed and experimental radial mean temperature profiles at different axial locations are shown in Fig. 6.9. The axial distances are normalized based on the computed peak-soot location. There is good agreement at the upstream station ($x/x_m = 0.4$), much before the peak soot volume fraction location. Downstream at $x/x_m = 0.7$, the computed temperature is higher at the axis, while it drops much faster compared to experiment away from the axis. Near the peak soot location $x/x_m = 1$, the temperature is over-predicted near the axis, but overall agreement is very encouraging in the radial direction.

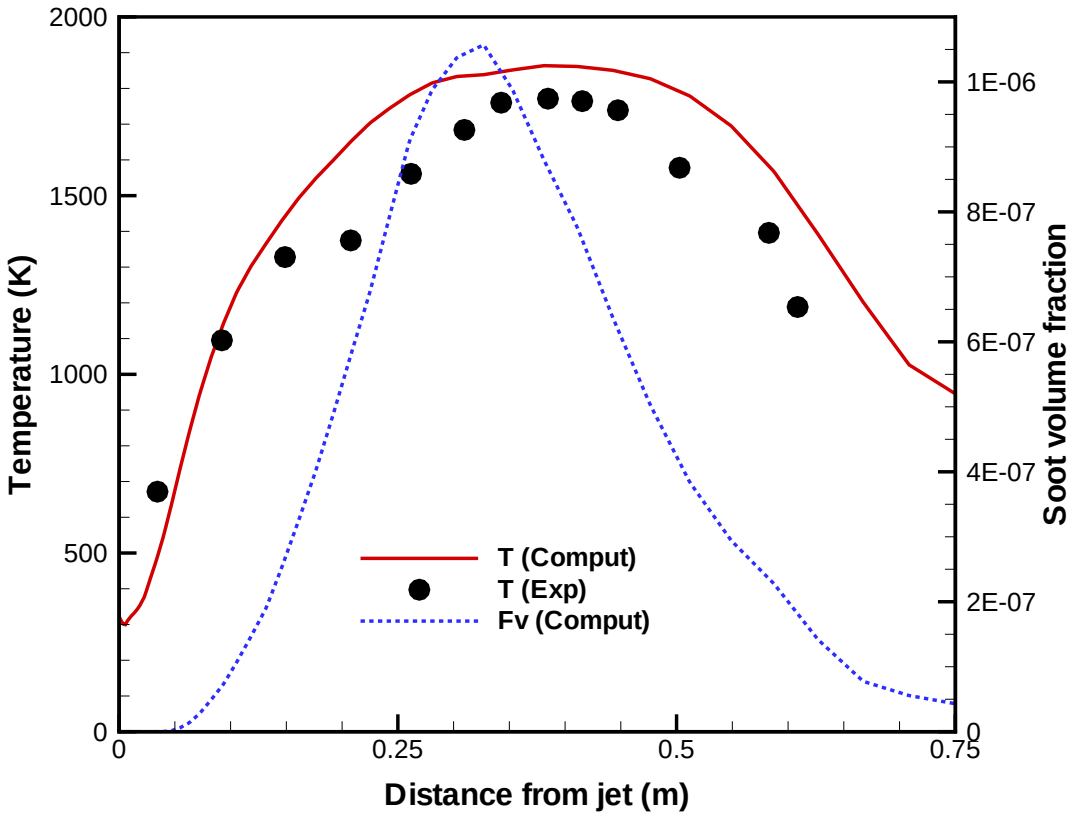

Figure. 6.8 Centerline mean temperature profiles for Flame-II (KH87). Dashed line is the computed soot volume fraction.

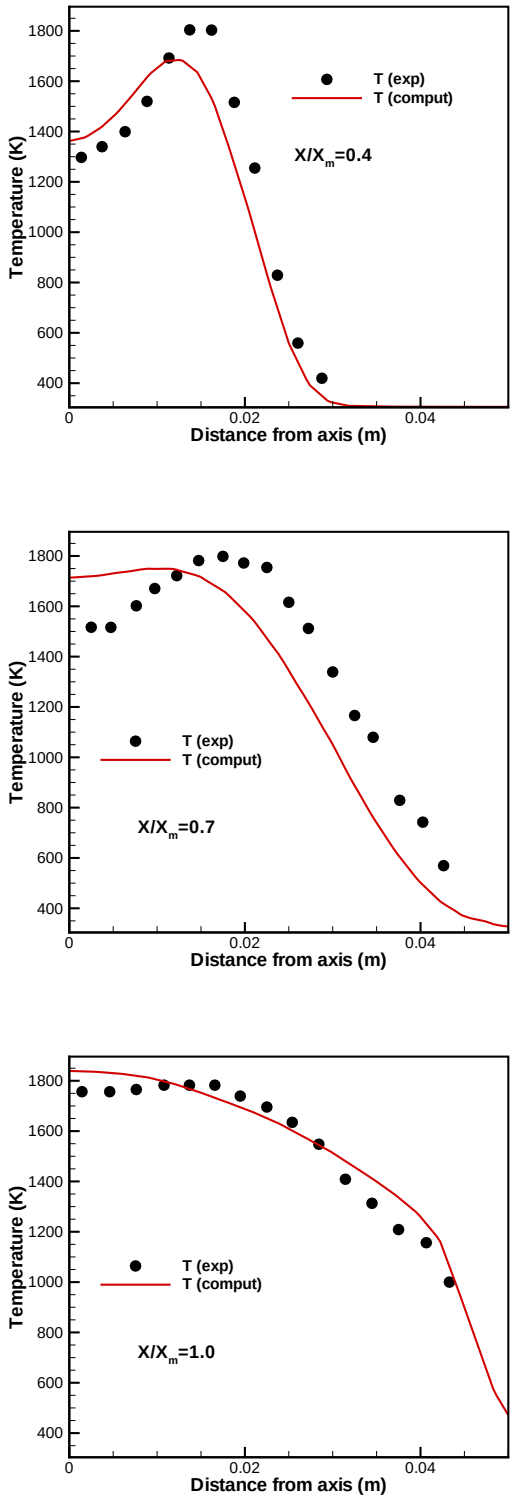

Figure. 6.9 Radial mean temperature profiles at three axial locations for Flame-II

The experimental radial mean soot volume fraction profiles were obtained by an Abel-inversion of the line-of-sight extinction data. The line-of-sight extinction measurements were coupled to soot volume fraction based on an assumed complex index of refraction for soot $m_{\mathrm{KH87}} = 1.94 - 0.54i$. The inversion procedure also results in increased uncertainty near the axis [156]. In the current study, the correlations given by Eqs. 4.23 and 4.24 have been used. Hence, the computed data has been corrected to be consistent with experimental data. The basic assumption is that the intensity attenuation will remain constant irrespective of the assumed optical properties of soot. A similar adjustment has been performed for all the flames studied here. The radial mean soot volume fraction profiles at various axial locations are shown in Figures 6.10 and 6.11. As seen in Fig. 6.10, the computed soot volume fraction at the upstream station ($x/x_m = 0.4$) shows an off-center peak not seen in experiment. However, the prediction is still within a factor of two over most of the domain. At the downstream location ($x/x_m = 0.7$), the computed soot is within 30% of the experiment, throughout the radial distance.

As shown in Fig. 6.11, at the peak soot station $x/x_m = 1$, the soot is under-predicted near the axis, while it is over-predicted away from the axis. This could be due to lower oxidation rates in the simulations compared to the experiments, or it may be due to uncertainty of soot measurements near the axis. A similar trend is seen in the downstream station $x/x_m = 1.4$, where it can be seen that the soot is over-predicted by up to a factor of 2.0 away from the axis; this probably is within the expected accuracy of the models.

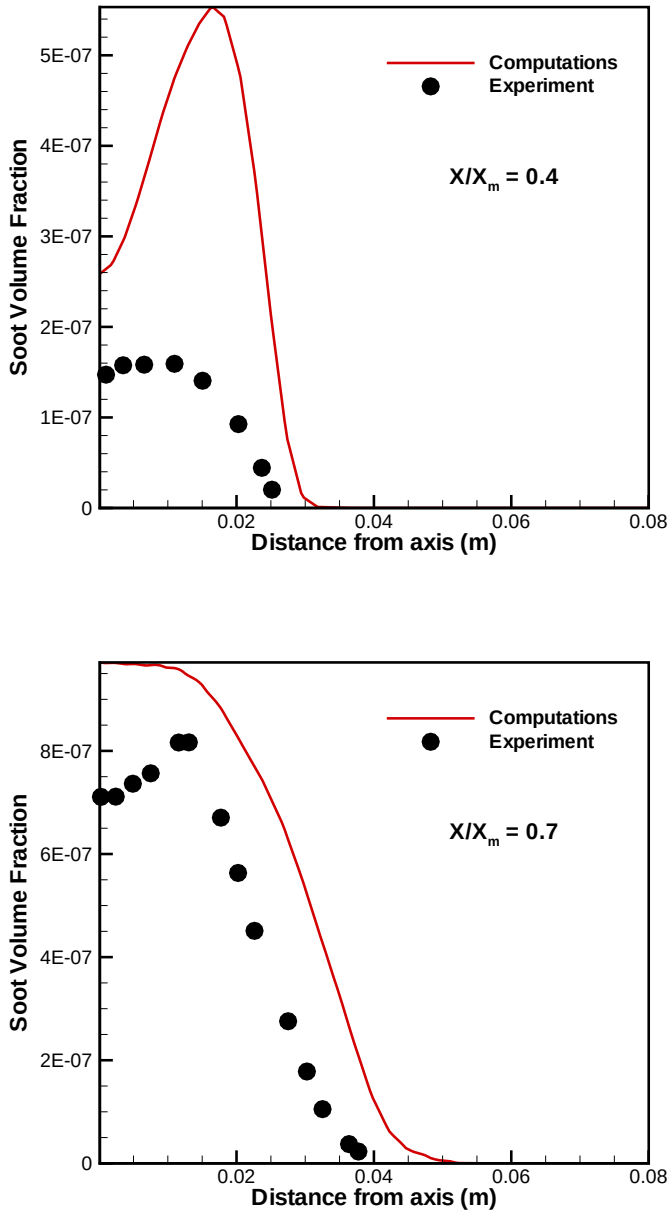

Figure. 6.10 Radial soot volume fraction profiles at the upstream stations for Flame-II.

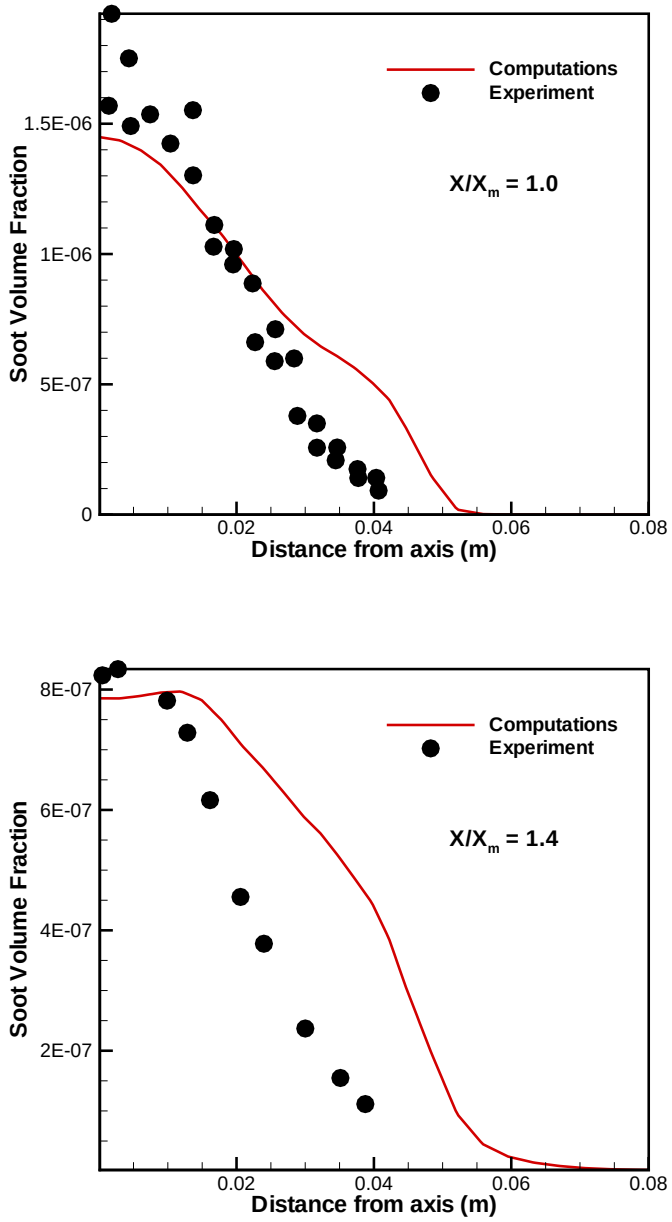

Figure. 6.11 Radial soot volume fraction profiles at the downstream stations for Flame-II.

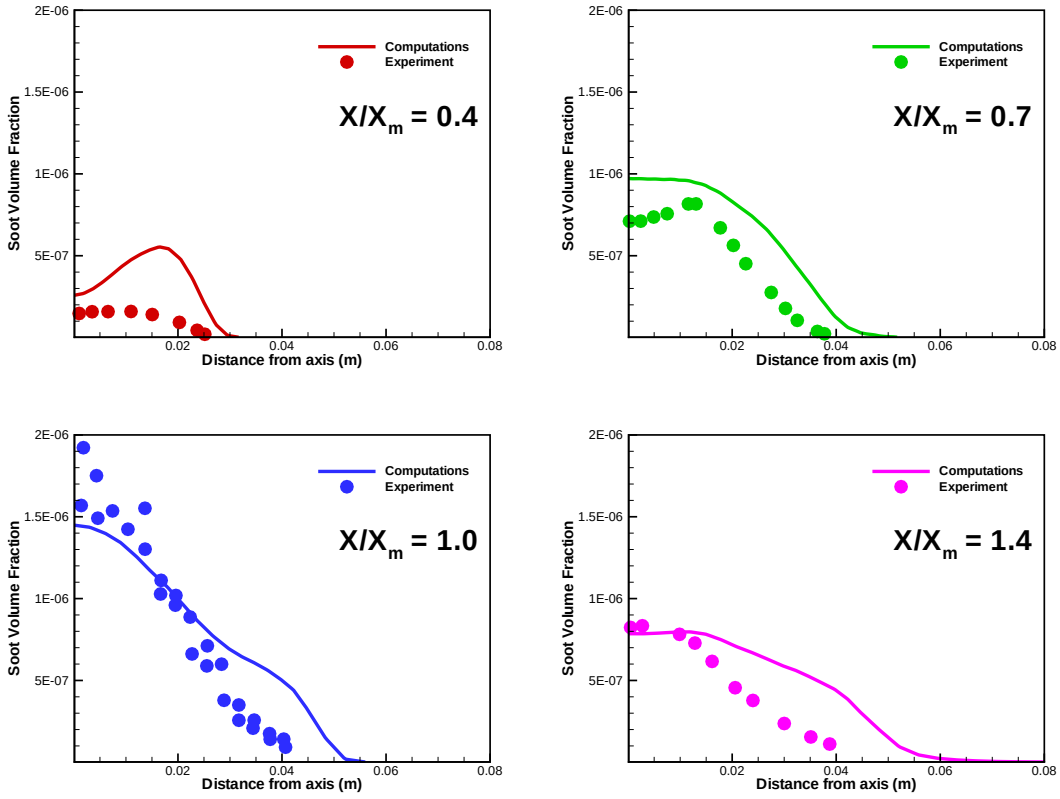

Figure. 6.12 Radial soot volume fraction profiles relative to each other (constant ordinate scale) for Flame-II.

To better understand the predicted and measured soot volume fractions, and soot formation characteristics of the flame, the soot predictions are presented on the same scale in Fig. 6.12. It can be seen that the modeled soot core extends further radially than experimental data. However, in general, the agreement with the experimental data is very encouraging.

6.6 Flames III–VI (Oxygen Enhanced Flames)

Turns and coworkers [92, 157, 164, 165] undertook detailed characterization of turbulent jet flames with oxygen enrichment. They conducted a number of experiments to understand how key parameters affect the soot, radiation and emission characteristics of jet flames over a range of oxygen indices from 21% (air) to 100% (pure O_2). Fuel issued from a jet with inner diameter 3 mm, into a low-velocity oxidizer stream for a variety of conditions. The fuel jet velocities (jet Reynolds numbers) were also varied to understand effects of turbulence levels and residence times on various measured quantities. In addition, a number of different fuel types including propane, natural gas (94% methane), methane-ethylene (90%–10% by volume) mixture etc, were used. Endrud [157] reports experimental data which was later extended and used by Wang [92] in developing comprehensive modeling strategies for turbulent jet flames.

Wang et al. [164] used the ABF00 (Table 5.1) mechanism [15], which becomes prohibitively expensive when used in the context of transported PDF methods. Hence, propane flames are not considered in the current validation, even though propane flames yield the maximum soot formation. The soot yields from natural-gas flames are almost an order of magnitude lower than propane flames and hence were not considered here.

Another set of experiments was conducted with a methane-ethylene mixture (90%–10% by volume) as fuel. Oxygen concentration was varied from 21% to 100%. Soot formed in these flames was found to be a strong function of the oxygen concentration, initially increasing and then decreasing with the amount of oxygen present in the oxidizer stream. The flame structure was varied, with peak temperatures occuring earlier along the axis as the oxygen concentration is increased.

Line-of-sight laser-extinction measurements were used to measure an equivalent soot volume fraction at different axial locations. The equivalent soot volume fraction is given by

$$Fv^* = \frac{1}{d_j}\int_{-\infty}^{\infty} Fv(r)dr = \frac{\lambda}{6\pi d_j \mathrm{Im}\left(\frac{m^2-1}{m^2+2}\right)} \ln\frac{I}{I_0} \tag{6.2}$$

where, Fv^* is the equivalent soot volume fraction, d_j jet diameter, λ is the wavelength of laser used for measurement, $m = n - ik$ is the complex index of refraction of soot and I/I_0 is the measured attenuation (extinction) of the intensity as the beam passes through the flame. As pointed out by Wang et al. [164], the equivalent soot volume fraction is an easily reproducible global measurement, and in the absence of simultaneous detailed measurement of soot volume fraction, velocities and temperature, the equivalent soot volume fraction is a more precise way to differentiate among sooting characteristics than using the Abel-inversion technique to get radial profiles of soot volume fractions (e.g. as was done in [156]).

Radiation measurements were made using a wide-angle (150°), wide-band radiometer with a IRTRAN window that allows transmission at 12 μm wavelengths of water bands. Radiative heat flux measurements were made at 100 mm intervals along

the wall and then integrated to determine the total heat loss. The duct walls are coated with infrared high-temperature black paint. The net radiative loss from the flame is evaluated by using Simpson's quadrature along the bounding surfaces of the domain [157]. The radiant heat loss as a fraction of the total chemical heat release rate was also reported [157, 164]

6.6.1 Modeling for Flames III–VI

The models used are summarized in Table 6.2. Standard k-ϵ model is used, along with the transported PDF model (extended to handle soot scalars) for accurate turbulent closure. The mixing model constant $C_\phi = 2$ yielded the closest results to experiment, which are also reported here. Simulations carried out with $C_\phi = 3$ as the mixing model constant, showed almost 20% higher radiative wall fluxes although the soot predictions were commensurate with the experiments. The RTE is solved using PMC method, with soot, H_2O and CO_2 emission/absorption included in the formulation. Radiation from CO and fuels is neglected. For the PDF model, 25–40 particles per cell are used, along with 1 ray per particle in the PMC method.

6.6.2 Principal Results: Oxygen Enriched Flames

The converged, mean temperature contours for flames III–VI are shown in Figure 6.13. It can be seen that as the oxygen mole fraction increases from 21% (air) to 55%, the peak (and overall) temperature in the flame increases. Also the peak temperatures occur upstream and closer to the jet exit, as the fuel burns off in shorter distance after

exiting the jet. Consequently the residence times for the flames decrease along with the flame length.

The computed centerline mean temperature profiles are shown in Fig. 6.14. It can be seen that the peak axial temperature increases from $\sim$ 1800 K to $\sim$ 2600 K with the increasing oxygen content. This has a direct effect on the sooting tendency and overall flame structure, as discussed later. The axial location of the peak temperature shifts upstream with increasing oxygen content.

The equivalent soot volume fractions for Flames IV–VI are shown in Fig. 6.15. The equivalent soot measurements were inferred based on extinction measurements and using the complex index of refraction of soot proposed by Lee and Tien [166]. These measurements have been modified to be consistent with the soot index of refraction proposed by Chang and Charalampopulous [136], and then compared with the computations. The peak soot volume fraction is highest at 30% oxygen and drops progressively as the oxygen content is increased. The experiments report unmeasurable soot at atmospheric conditions and with oxygen indices above 55%. The increase in oxygen has a two-fold effect on the soot kinetics.

a. Higher oxygen concentration increases the hydrogen-radical pool (H_2-O_2 chemistry). The hydrogen radicals are very active and result in larger radical sites on the soot surfaces, which in turn increases acetylene-addition and hence promotes soot growth.

b. Increased oxygen also oxidzes the soot precursors as well as the soot that is being formed, thereby reducing the soot formation.

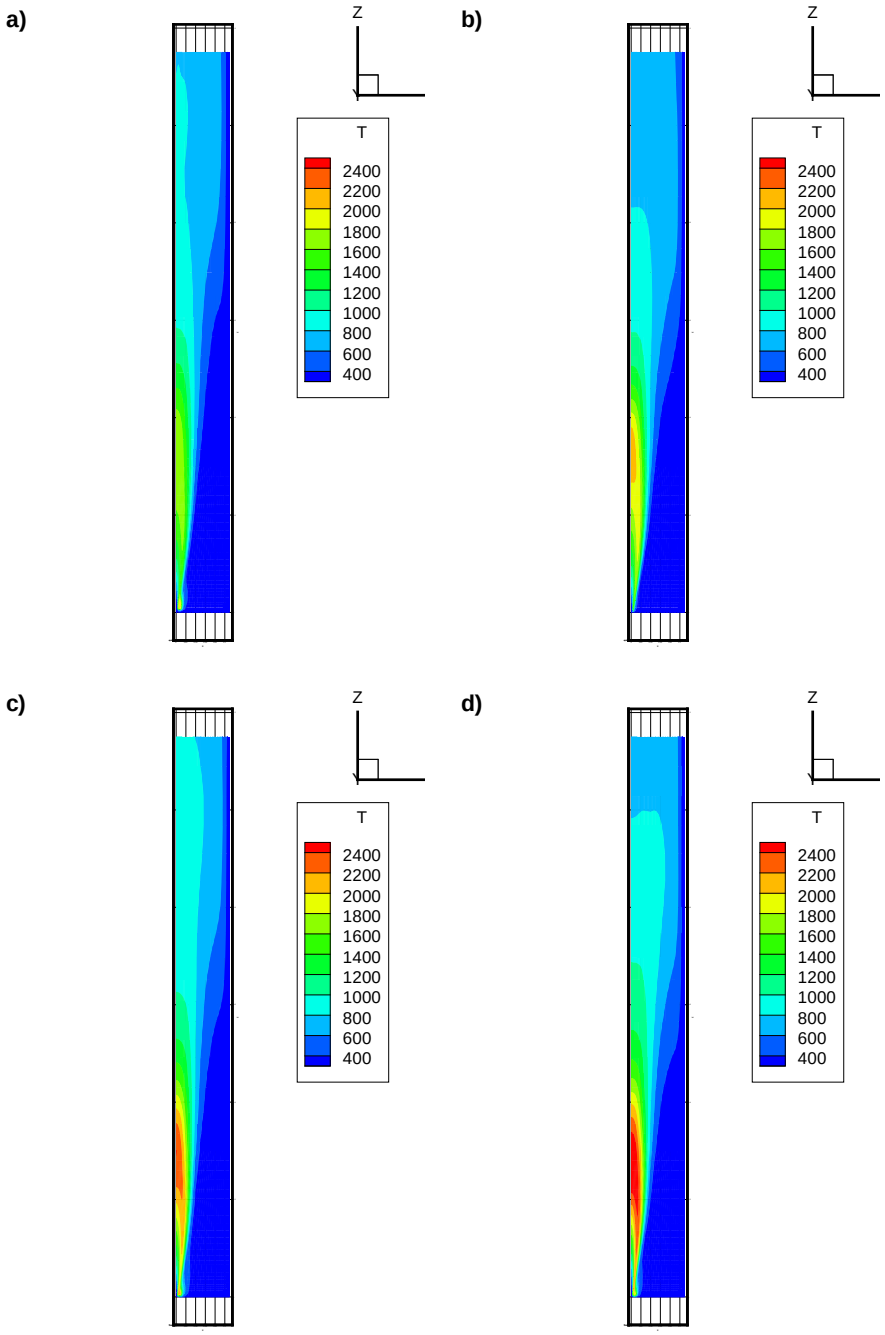

Figure. 6.13 Computed mean temperature contours for a) Flame III through d) Flame VI.

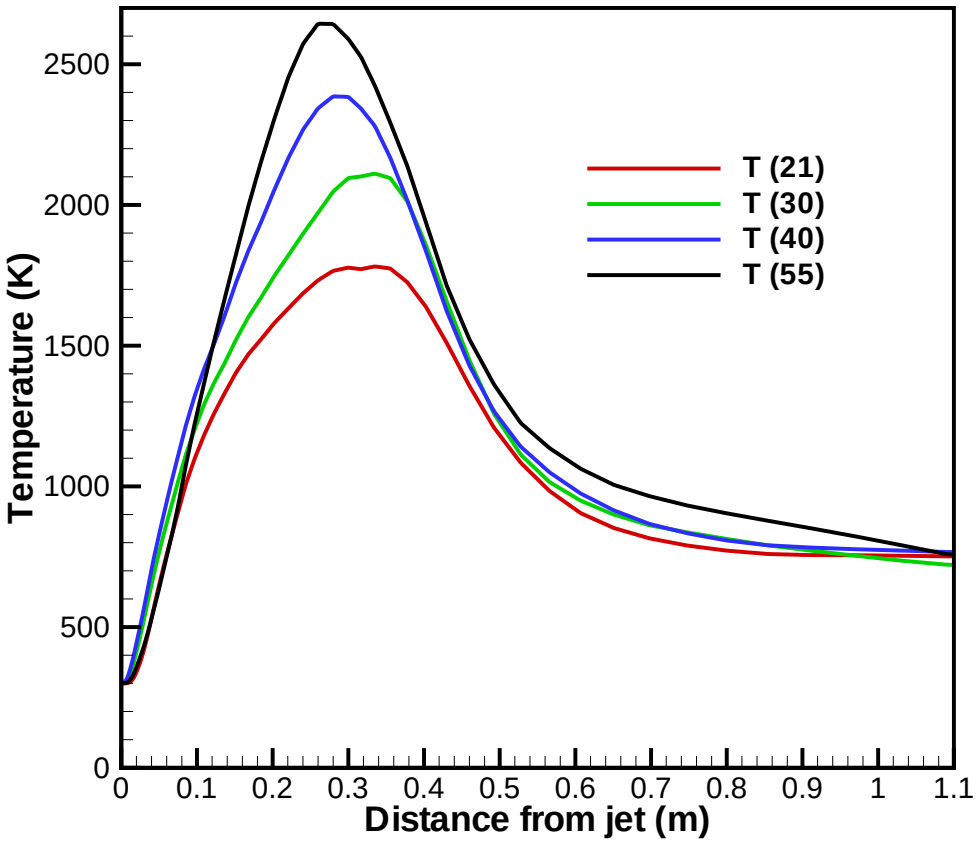

Figure. 6.14 Computed centerline mean temperature profiles for Flames IV–VI with increasing oxygen content

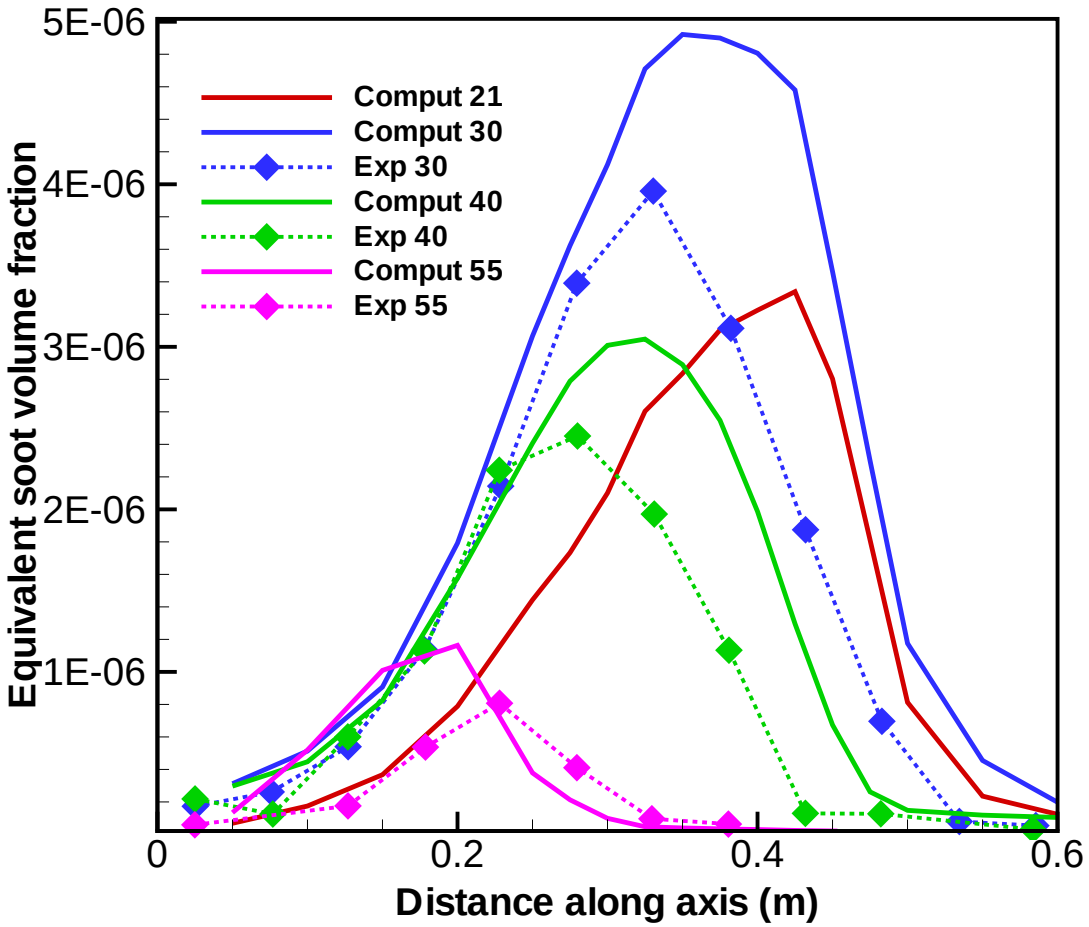

Figure. 6.15 Computed and measured equivalent soot volume fraction profiles Fv^* for different oxygen indices.

The net effect of oxygen enhancement is therefore decided by the relative importance of these processes. Thus in the initial stages, the increasing oxygen results in a larger increase of the hydrogen-radical pool and hence a much enhanced soot growth. This is followed by a gradual increase in the soot oxidation rates, progressively reducing the soot yield.

It can be seen from Fig. 6.15 that the agreement between the computed and experimental equivalent soot volume fraction is reasonable. The computed peak soot location is always upstream compared to the experimental data for all the flames considered. This could be due to the k-ϵ model which over-predicts the jet spreading rate, thereby resulting in slightly shorter flames. Another possibility is that the chemistry model being used was optimized for ethylene (C_2H_4) and may not be completely faithful in modeling methane (CH_4), particularly with increasing oxygen concentration. However, the soot prediction is within 25% of the experiments, and represents a significant advance in the current state-of-the-art modeling strategies for soot formation in turbulent flames. There is a random-error element in the experimental soot of approximately $\pm 5.0 \times 10^{-7}$, and hence for small soot volume fractions, the signal to noise ratio is very low for reliable measurements. Such is the case with Flame-III, with just air as the oxidizer or when oxygen concentration is increased beyond 55%. Another aspect to note is the fact that soot is under-predicted for flames IV and V, while slightly over-predicted for flame VI. This is most likely to the unsuitability of the current chemistry model for oxygen-enriched methane flames.

The computed and experimental radiative wall fluxes are shown in Fig. 6.16. The peak predicted radiative flux is within $\sim$ 15%-20% of measurements. The radiative

emission has a fourth power dependence on the temperature; thus a 20% discrepancy in radiative fluxes would suggest a temperature discrepancy of $\sim 5\%$, if all other quantities are predicted correctly.

Similar studies were done by Wang [92] using a Two-Stage Lagrangian (TSL) model for turbulence–chemistry interactions and P_1-RTE solver. However, it was realized that the P_1 method was highly inaccurate in the current scenarios due to very anisotropic intensity distribution. Here, the use of PMC results in a much better agreement with experimental data and shows the efficacy of all the underlying models being applied. Wang [92] used Model 11 listed in Table 5.4, and reported an under-prediction of soot by more than an order of magnitude. However the composition PDF method was not used for capturing TCI. The higher temperatures reported in [164] will also result in suppressed soot formation, thereby affecting the radiative losses from the flame and in general the overall flame structure. Accurately accounting for the turbulence–chemistry interactions is known to reduce the predicted temperatures to a great extent, particularly in jet flames [44, 88]. The net effect of accounting for the turbulence–radiation interactions would be analyzed in detail in Chapter 7.

It can be seen that the predicted peak wall fluxes for all flames III-VI are upstream of the experimental measurements and could be attributed to the shorter computed flames. In fact, with increasing oxygen content, the computed peak shifts more upstream than experiments as can be seen from Table 6.4. This implies that the computed flames occupy a smaller region of the domain compared to the experimental flames as the oxygen index is increased. The difference is most pronounced for flames V and VI, where the

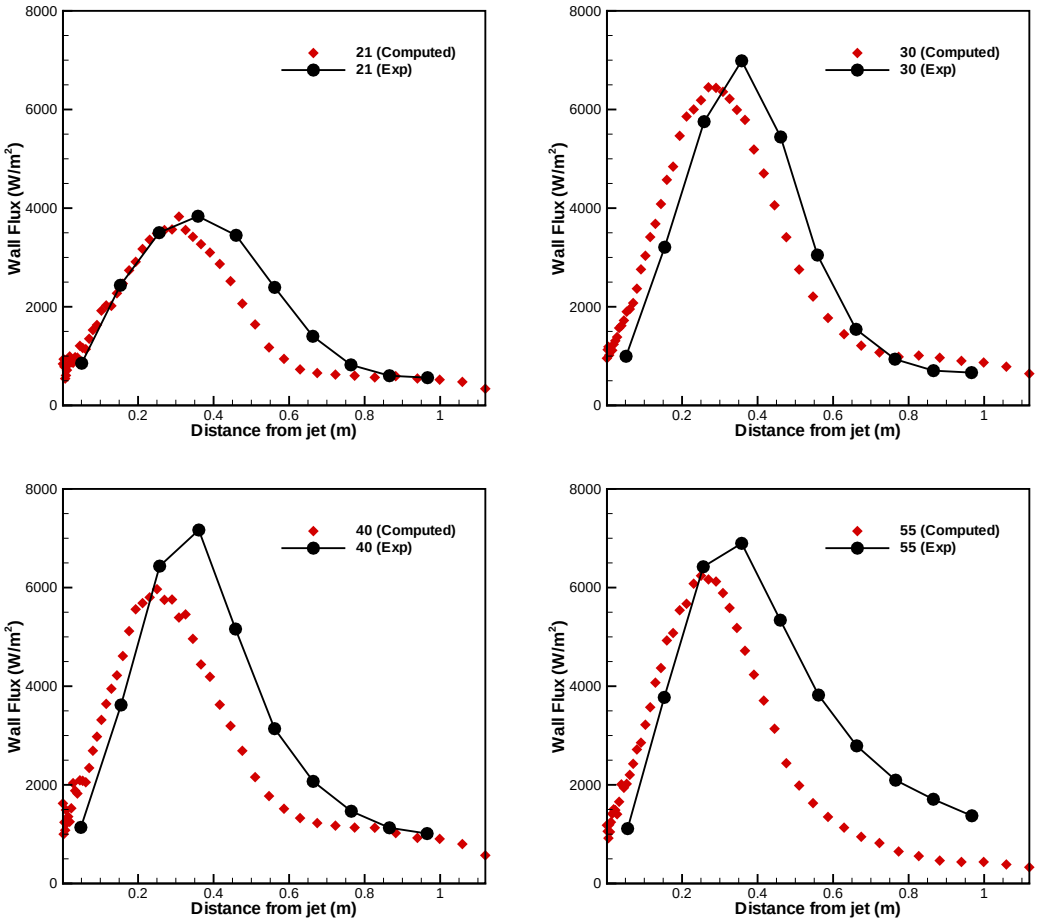

Figure. 6.16 Computed and measured radiative wall flux on the enclosure wall for Flames III–VI.

peak flux is upstream by almost 0.1 m. This also implies that the computed flames are very short and hence have a lower wall flux throughout the downstream region.

Table 6.4 Location of the computed peak wall flux compared with experiment.

Flame	Oxygen Index	Computed Peak Location	Experimental Peak Location	Difference
III	21	0.306	0.360	0.054
IV	30	0.293	0.360	0.067
V	40	0.262	0.360	0.098
VI	55	0.251	0.360	0.109

Table 6.5 Radiant fraction comparison for flames III–VI

Flame	Oxygen Mole Fraction (%)	Experimental	Computed
III	21	0.135	0.154
IV	30	0.195	0.243
V	40	0.217	0.236
VI	55	0.238	0.228

The radiant fraction values for flames III–VI are shown Table 6.5 and plotted with the experimental data in Fig. 6.17. The chemical heat release is calculated based on higher-enthalpies of combustion (i.e., gaseous water-vapor in the products) for methane and ethylene as 50.0 MJ/kg and 47.1 MJ/kg, respectively. The experimental radiant heat fractions increase with increasing oxygen content. However, the computed radiant fractions decrease for flames V and VI due to much smaller flame lengths (and hence hot zones for radiation). It is expected that this problem can be solved by using better chemistry mechanism for the gas-phase chemistry. This is a direct result of increased temperatures with higher oxygen content in the flames. The experimental data is based

on radiative flux measured in a specific spectral range 0.5–12 μm, whereas the computed flux includes the entire spectrum. Although almost 95% of the emission is in this spectral range, there would be some radiative loss outside of this range and that may explain some of the higher computed radiant fractions for flames III and IV. It is possible to filter out the net heat loss from the flame based on spectral range in context of the PMC method that was not done in the current study. In general, the predictions are in very good agreement with the experiments.

The emission from soot in the flames III–VI does not exceed more than 8% of the total emission (soot plus gases). See Chapter 7 for more details about the radiation characeristics of these flames. Thus it is possible that accouting for soot may not affect the radiative flux calculations to a larger extent. The study by Wang [92] shows shortcomings of the P_1 RTE solver in case of oxygen-enhanced propane flames with similar structure as the current flames III-VI. The excellent agreement in the current flames may be partly due to the PMC RTE solver and partly due to a better accounting of TRI. The importance of TRI will be assessed in detail in chapter 7.

6.7 Soot Prediction in Turbulent Flames

In the previous sections, several sooting, turbulent jet flames have been simulated and various predicted quantities compared with experiments. It becomes very clear that even in moderately sooting flames, the accurate prediction of soot is very important as it drives the radiative transfer from the flame, consequently affecting the entire flame structure. Model 32 from Table 5.4 has been used for modeling soot formation in turbulent jet flames. It can be seen that Model 32 over-predicts soot for most of the laminar

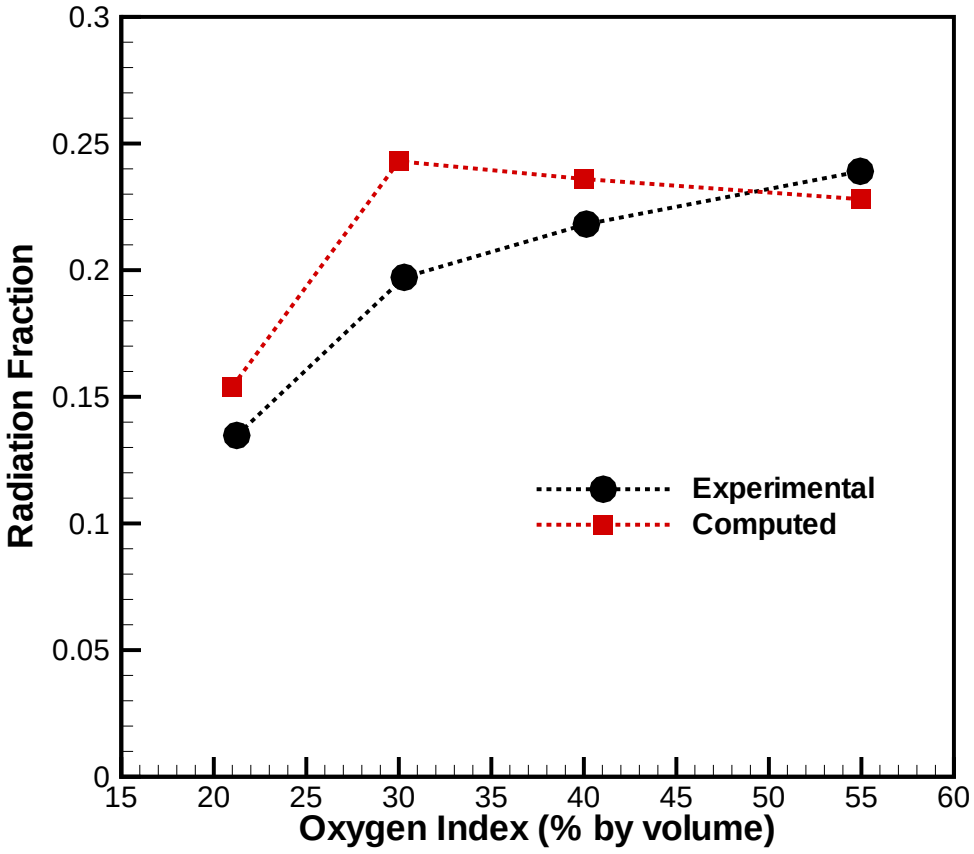

Figure. 6.17 Computed and measured radiant fractions for Flames III–VI.

flames by up to an order of magnitude (at most). However, when applied in turbulent flames the same model seems to predict soot to within a factor of 1.5 for almost all the flames, irrespective of the fuel-type, jet Reynolds number or sooting propensity.

The soot model also assumes conserved surface radicals, which is an extreme case and promotes soot surface growth to a large extent. In spite of this, the soot predictions in all these flames are not too high compared to the experiements. In fact the soot seems to be under-predicted for the most part. The most probable explanation seems to be that soot particles are modeled as spherical particles, with

i. Perfect coagulation: Two spherical particles collide, coalesce completely into a larger spherical particle.

ii. Uniform surface reactions: Surface reactions grow the particles while maintaining spheroidal geometry.

Both these assumptions result in a fixed area-to-volume ratio ($3/4r$) for the soot particles. It is most likely that the soot particles attain nonspherical geometries with much higher area-to-volume ratios. In such a scenario, Model 32 would predict much higher soot volume fractions due to much higher number of surface-reaction sites. This may also explain why the soot models which predict soot accurately in laminar flames seem to under-predict in turbulent flames. Modeling of soot aggregation into nonspherical mass fractals in context of the method of moments [127] shows better agreement in high-pressure laminar flames. The current model can be extended to handle soot aggregation. Another possibility would be to resolve the soot PSDF using methods like the sectional method, thereby accounting for the soot particle surface area more accurately.

6.8 Summary

In this chapter, a transported PDF method coupled with a detailed gas-phase chemistry, soot model and RTE solver has been applied to various jet flames with Reynolds numbers varying from $\sim$ 6700–15100. Two ethylene/air flames and four flames with a blend of methane-ethylene and enhanced oxygen concentration have been simulated. All the model parameters have been kept constant. These include: i) soot submodels like surface-reaction rates; ii) mixing model constant in transported PDF methods; iii) PMC model constants such as rays-per-particle, opening angle etc., and iv) turbulence model constants like those in k-ϵ equations etc. Except for the well-established and relatively simple k-ϵ turbulence model, all other processes are simulated using advanced models for chemistry, TCI, radiative properties and RTE solver.

The results show excellent agreement between experimental and computed temperature levels for most of the flames. For flames II–VI, the peak temperature seems to occur upstream of the experiments, which maybe due to the simple turbulence model, resulting in over-prediction of the jet-spreading rates. Even though the soot model was validated only in ethylene/air flames, it performs reasonably well even in oxygen-enriched methane/ethylene flames. The soot predictions for all the flames considered are within a factor of 1.75 as a most conservative estimate. Radiative flux measurements are only available for flames III-VI and computations show very good agreement with the experiments. This seems to be the combined effect of better radiative property model (line-by-line) and RTE solver (PMC) along with accurate accounting for both emission and absorption TRI.

Chapter 7

Investigation of Turbulence Radiation Interactions

7.1 Introduction

Turbulence-radiation interactions are significant in reacting flows. To capture TRI in simulations means to accurately estimate the left-hand sides of Eqs. (3.4) and (3.6). As discussed in previous chapters, the composition PDF method coupled with PMC represents a significant advance in the state-of-the-art for modeling sooting turbulent jet flames and turbulent combustion in general. Thus it should be possible to obtain rigorous physical insight into various aspects of radiation in sooting flames including i) quantitative importance of TRI, ii) radiation characteristics of the sooting flames (separating importance of soot and gas radiation) and iii) importance of accurately capturing TRI during simulation of sooting combustion.

7.2 Frozen Field Analysis

Radiation is inherent to all reacting flows. It is not possible to separate out the effects of TRI when conducting physical experiments. A very important advantage of physics-based simulation techniques, such as the ones developed here, is the ability to quantify effects of various subprocesses on the over-all flame structure and phenomena of interest. The stochastic solution for transported PDF method is based on the idea that each Lagrangian particle represents a flow simulation. Thus an ensemble of particles

through the entire domain can be viewed as a snapshot of the turbulent flow-field. An appropriate approach to isolate the effects of TRI would be to solve the RTE based on the mean fields (neglecting TRI) and also based on the the particle fields in a statistically steady state (including TRI). The difference between these two solutions is then solely due to TRI.

7.2.1 Separating TRI

To systematically isolate TRI effects, a frozen field study is carried out. Ten spatially uncorrelated particle fields are extracted from the fully-coupled, full-TRI simulation after achieving statistical convergence (or statistically steady state). The PMC method is used in conjunction with the frozen fields by considering full TRI (emission and absorption both include turbulent quantities), partial TRI (only emission is based on turbulent quantities) and no TRI (emission and absorption are both based on cell mean quantities), to estimate the corresponding radiative transfer from the flames. An appropriate metric to gauge the net effect of various TRI modes on the radiative transfer from a flame is to estimate the total emission from the flames evaluated with and without the TRI effects

$$\dot{Q}_{emi} = \int_V q_{\text{emi}} dV \tag{7.1}$$

and net heat loss from the flame evaluated with and without TRI effects.

$$\dot{Q}_{net} = \int_V \nabla \cdot \underline{q_R} dV \tag{7.2}$$

where q_{emi} is the local volumetric radiative emission and $\nabla \cdot \underline{q_R}$ is the local radiative heat loss per unit volume.

The availability of multiple uncorrelated particle snapshots also allows quantification of the statistical uncertainty in various estimates. The results of different TRI treatments on the total emission and the net radiative heat loss for the six flames flames I–VI presented in the previous chapter are shown in Tables 7.1 and 7.2, respectively. The results are obtained based on the snapshots with $100,000$ photon bundles for each trial.

Table 7.1 Emission TRI from flames I–VI based on frozen uncorrelated particle fields (in kW)

Flame	No TRI $\dot{Q}_{emi}$ (kW)	Emission TRI $\dot{Q}_{emi}$ (kW)	$\Delta\dot{Q}_{emi}$ TRI %
I	4.42	6.17 ($\pm$0.45%)	39
II	4.88	7.63 ($\pm$1.75%)	57
III	1.59	2.24 ($\pm$1.2%)	41
IV	2.58	3.41 ($\pm$0.11%)	32
V	2.31	3.32 ($\pm$0.22%)	44
VI	2.18	3.02 ($\pm$0.38%)	38

Net emission increases by $\sim$ 30-60% when accounting for TRI and can be used to quantify emission TRI for these flames. Emission TRI values are in a similar range as those found by Li [46]. Table 7.2 shows the computed net heat loss from the flames by considering full TRI, partial (emission) TRI and no TRI. When considering full TRI, the predicted heat loss is $\sim$ 40-90% higher than that obtained without including TRI. This fact has tremendous implications on the modeling strategies for reacting flows in general. When the radiant fractions as a function of the chemical heat release increase, TRI will

affect the flame structure even more. The net effect of TRI is higher than that found in nonsooting flames with similar Reynolds numbers [46], in which the heat loss increased roughly by 35% when TRI were included. Another important part of determining TRI

Table 7.2 Effect of TRI on the net heat loss from the flames I–VI based on frozen uncorrelated particle fields (in kW)

Flame	No TRI $\dot{Q}_{net}$ (kW)	Partial TRI $\dot{Q}_{net}$ (kW)	$\Delta\dot{Q}_{net}$ Partial TRI %	Full TRI $\dot{Q}_{net}$ (kW)	$\Delta\dot{Q}_{net}$ Full TRI %
I	2.34 (±0.2%)	3.97 (±0.7%)	70	3.95 (±0.67%)	69
II	2.89 (±0.34%)	5.46 (±1.45%)	89	5.45 (±2.26%)	88
III	0.77 (±0.93%)	1.27 (±2.37%)	65	1.25 (±2.95%)	62
IV	1.39 (±0.2%)	2.10 (±0.17%)	52	2.12 (±0.4%)	50
V	1.33 (±0.17%)	2.05(±0.37%)	54	2.05 (±0.59%)	54
VI	1.38 (±0.26%)	2.01(±0.37%)	45	2.00 (±0.8%)	44

is quantification of absorption TRI, or the correlation between the absorption coefficient and incident intensity. Absorption TRI can be separated based on the following equation

$$\underbrace{\langle \kappa I_b \rangle - \langle \kappa G \rangle}_{\text{Full TRI}} = \underbrace{\langle 4\pi\kappa I_b \rangle - \langle \kappa \rangle \langle G \rangle}_{\text{Partial TRI}} - \langle k' G' \rangle \tag{7.3}$$

which results in

$$\underbrace{\langle k' G' \rangle}_{\text{Absorption TRI}} = \underbrace{\langle 4\pi\kappa I_b \rangle - \langle \kappa \rangle \langle G \rangle}_{\text{Partial TRI}} - \underbrace{\langle 4\pi\kappa I_b \rangle - \langle \kappa G \rangle}_{\text{Full TRI}} \tag{7.4}$$

where $G = \int_{4\pi} I d\Omega$ is the net incident radiation integrated over all directions at a given point. The difference in the computed heat loss based on full TRI and partial TRI can be attributed solely to absorption TRI. The separation of absorption TRI is shown in

Table 7.3 as a percentage of the net heat loss with full TRI. It can be seen that the net effect of absorption TRI is negligible for all flames. This is true even for flame II which has the highest peak soot volume fraction. However, the statistical uncertainty in calculating the net heat losses is of the same order as the reported absorption TRI. This implies that there is almost no absorption TRI for any of these flames. It appears that absorption TRI is always negligible for the laboratory-scale flames studied in the current work. Thus, it should be possible to neglect absorption TRI for relatively small flames, irrespective of whether they are sooting flames or not. However, whether or not absorption TRI can be neglected in general remains an open question, which will be addressed later in this chapter.

Table 7.3 Net absorption TRI for flames I–VI. The statistical variance is greater than the computed values of absorption TRI, indicating negligible absorption TRI in all the flames.

Flame	$\Delta\dot{Q}_{net}$ Full TRI	$\Delta\dot{Q}_{net}$ Partial TRI	Absorption TRI (%)	Statistical scatter $\sigma_{std,\Delta\dot{Q}_{net}}$%
I	3.948	3.965	0.44	0.67
II	5.457	5.461	0.07	0.5
III	1.25	1.290	0.32	1.2
IV	2.101	2.121	0.96	0.24
V	2.051	2.054	0.17	0.37
VI	2.000	2.011	0.57	0.6

7.2.2 Gas and Soot Radiation

Analysis of flame radiation without feedback (i.e., based on statistically identical frozen particle fields), has been used to isolate the effects of TRI. A first-order estimate of the importance of soot-radiation for a given flame can be obtained by comparing the

net emission due to soot and due to gases. These values are shown in Table 7.4. It can be seen that soot emission is as high as 46% of the total for flame II and less than 5% for flames III and VI. The increase in soot with enhanced oxygen increases both gas

Table 7.4 Soot and gas emission as fractions of the total emission from the flame

Flame	Total Emission (W)	Soot Emission (%)	Gas Emission (%)	Peak Soot (ppm)
I	6170	39	61	1.4
II	7638	43	57	1.9
III	2242	5	95	0.037
IV	3413	9	91	0.15
V	3324	7	93	0.13
VI	3025	4	96	0.09

emission (due to high temperatures) and soot emission due to higher soot formation. Thus for flame IV, soot emission is close to 10% of total emission.

The frozen field analysis can be used to separate, at least approximately, the net radiative loss due to participating gases and soot. The PMC RTE solver is applied to the converged, statistically steady particle field with soot radiation (both emission and absorption) included and excluded. The participating gases considered are carbon dioxide and water vapor. It is known that gases emit and absorb only across specific bands [1]. Soot radiation, on the other hand, is significant almost over the entire infrared spectrum, absorbing and emitting with a continuous absorption coefficient. With soot excluded from the PMC solution, the calculated emission is only due to gases. If it is further assumed that a relatively very small portion of gas emission is absorbed by soot, and that very little of the continuous spectrum soot emission is absorbed by the gases, then the contribution of soot radiation to the net heat loss from the flame can

be estimated (as they become additive). Table 7.5 shows the estimates of total gas and

Table 7.5 Estimated loss due to gases and soot, assuming negligible spectral overlap between the corresponding spectra

Flame	Gas emission (W)	Estimated loss due to gas emission(W)	% of gas emission lost	Soot emission(W)	Estimated loss due to soot emission(W)	% of soot emission lost
I	3739	1726	46	2431	2240	92
II	4357	2378	55	3282	3039	93
III	2141	1151	54	101	98	97
IV	3117	1821	58	304	296	97
V	3106	1823	59	218	212	97
VI	2902	1887	65	123	121	99

soot emission leaving the domain. It can be seen that only about 45-65% of the gas emission escapes domain. This is due to the fact that combustion gases emit and absorb in specific spectral bands and hence, not all gas emission can leave the flame without attenuation. The estimated loss due to soot emission is very different. It can be seen that more than 90% of soot emission leaves the domain. The main reason for this is the fact that continuum radiation from soot outside of the overlapping gas bands sees a relatively transparent medium and escapes without further attenuation.

The methane-ethylene blend flames (III-VI) show an even larger percentage of soot emission lost, compared to the ethylene flames I and II. This may be due to the fact that increasing temperatures of flames III-VI, shifts the peak Planck function to higher wave numbers, and results in lower overlap between the soot radiation and gas radiation. In addition the lower soot volume fractions for these flames also reduces the self-absorption of the soot emissions. Additional modifications to the PMC code would

enable one to estimate the amount of soot emission absorbed by the soot (self-absorption) and by the combustion gases. Although these cannot be separated in the current study, it seems likely that higher soot volume fractions result in higher soot self-absorption and, hence, a smaller fraction of soot emission is lost to the surroundings. It is an estimate of the author that soot emission absorbed by combustion gases is a very small fraction and potentially can be neglected.

A possible implication of these results (Table 7.5) is the fact that, even a gray soot radiative property model would suffice for predictions within experimental uncertainties. Since the soot models are predictive only within a factor of 1.5 at best, a gray soot model would still result in acceptable model for soot radiation, at least when soot levels are on the order of a few ppm as seen in the current study. A gray soot model can further reduce the effort of incorporating soot radiation into an existing RTE solver, or a PMC method. However, the gases still need to be treated in a nongray fashion to obtain sufficient accuracy.

To further illustrate the effect of soot radiation on the radiative flux distribution from the flame, wall fluxes for flame IV (30% Oxygen index) are plotted with soot included and excluded and compared with experimental data in Fig. 7.1. The net wall fluxes with or without soot radiation are similar downstream due to the fact that only a negligible part of the soot radiation can reach the downstream before leaving the domain. The figure also demonstrates the importance of accurate soot predictions.

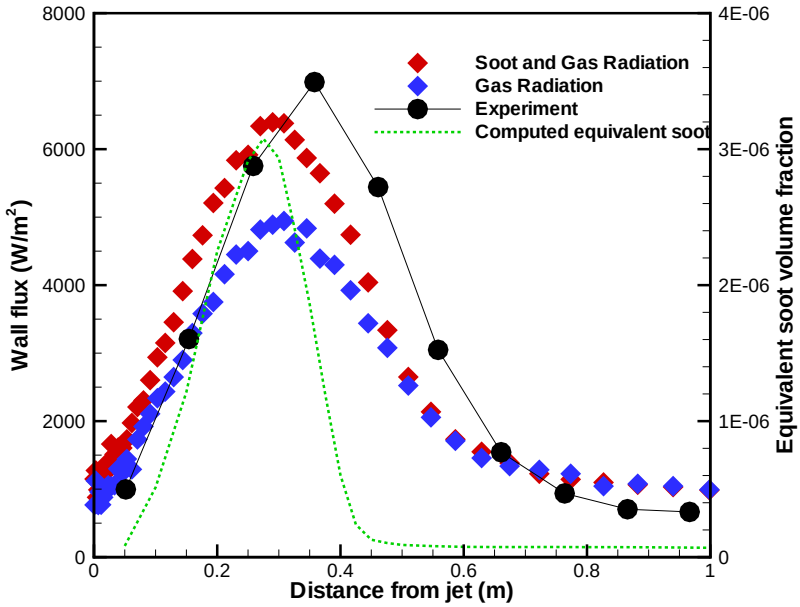

Figure. 7.1 Wall flux for flame IV excluding and including contribution due to soot radiation. Dashed line shows computed equivalent soot volume fractions

7.3 Simulations without TRI

In order to understand the importance of modeling TRI, a few flames are simulated in a fully coupled manner by ignoring TRI and their predictions are compared with those obtained earlier and experimental data whenever available. The fully coupled solution without TRI, also results in a different flame structure which also feeds back into the flow solver through the density field. Radiative properties are evaluated based on cell means of concentrations and temperature and do not account for turbulent fluctuations. All other model parameters are kept the same as those used in simulations with full TRI (Chapter 6).

The axial temperature profile for flame II is shown in Fig. 7.3. Neglecting TRI increases the peak temperature by $\sim$ 70K. The predicted peak axial soot is reduced from

1.2 ppm to just over 0.8 ppm. The soot also oxidizes quicker due to relatively higher temperatures downstream. Other key metrics for flame II, when neglecting TRI, are compared with the simulations including TRI in Table 7.6.

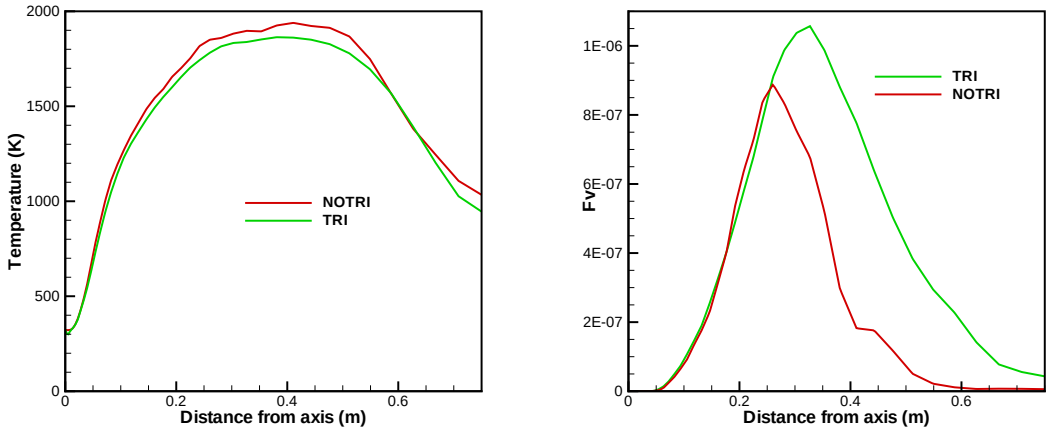

Figure. 7.2 Comparison between model predictions for the axial temperature and soot volume fractions for flame II, with and without TRI.

It can be seen that the overall flame is hotter when TRI is not included. However, the net radiative loss is still much lower as compared to predictions including the full TRI. The net effect of the increased temperatures also appears in the soot predictions. The predicted soot is lower due to two primary effects: i) the soot surface reactivity as modeled is inversely proportional to temperature, and ii) increased temperature also increases the oxidation rates for the soot. Increased temperatures increase the kinetic rates of all reactions, including the soot growth reactions and, hence, the exact effect of increased temperatures on the flame structure and soot yield is generally difficult to predict.

Table 7.6 Comparison of key metrics for flame II with and without TRI

Description	TRI	No TRI
Emission weighted average temperature (K)	1644	1888
Net radiative loss (W)	5450	2473
Peak axial soot volume fraction (ppm)	1.05	0.88
Peak axial temperature (K)	1863	1938

The predicted wall heat flux for flames III-VI without considering TRI are shown in Fig. 7.3. Neglecting the TRI consistently under-predicts the radiative wall heat flux and, consequently the radiative losses from the flame. The axial flame temperatures show an over-prediction by $\sim$ 20-60K for these flames when not considering TRI.

The increased temperatures have a marked effect on the kinetic rates of the chemical reactions as well as soot formation rates. The predicted equivalent soot volume fractions by neglecting TRI for flames III-VI are shown in Fig. 7.4. Flames III-IV (methane/ethylene blend flames) show a different trend when TRI is not included in the computations giving a very strong effect of TRI on soot predictions. The soot is overpredicted when TRI is not included. The over-prediction is as high as a factor of 3.5 in Flame V. This could be due to a number of reasons. One of the possibilities is that the surface reactivity of soot particles decreases with temperature and reaches an asymptotic value at high temperatures above $\sim$ 2100 K. If the surface reactivity factor reaches such a region, then increase in temperature will increase the soot growth instead of decreasing it. Another

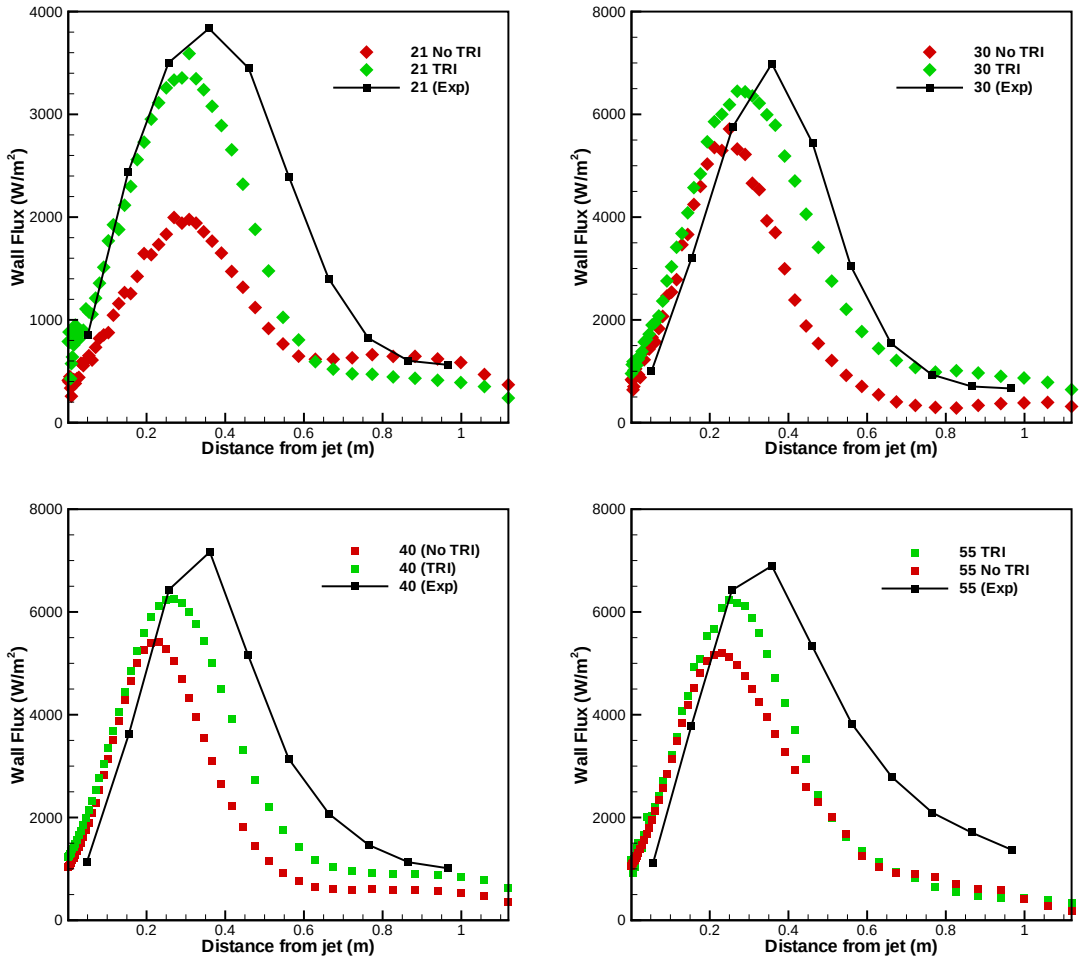

Figure. 7.3 Predicted wall fluxes for Flames III (top left), IV (top right), V (bottom left) and VI (bottom right)

possibility is that the methane chemistry results in local conditions near the flame sheet, such that an increase in temperature increases the net soot growth rates instead of decreasing them. These results also underscore the importance of accurately capturing TRI, when modeling sooting flames.

Some of the key metrics for the oxygen enriched flames III-VI are shown in Table 7.7. The emission weighted average computed temperature defined as

$$T_{\text{emi,av}} = \frac{\int_V k_p \sigma T^5}{\int_V k_p \sigma T^4} \tag{7.5}$$

where k_p is the total Planck-mean absorption coefficient and T is the temperature, is consistently higher when neglecting TRI. The net radiative loss from these flames is $\sim$ 30-50% smaller despite the higher temperatures and soot levels. The computed peak axial temperature is $\sim$ 30-60 K higher when TRI are neglected.

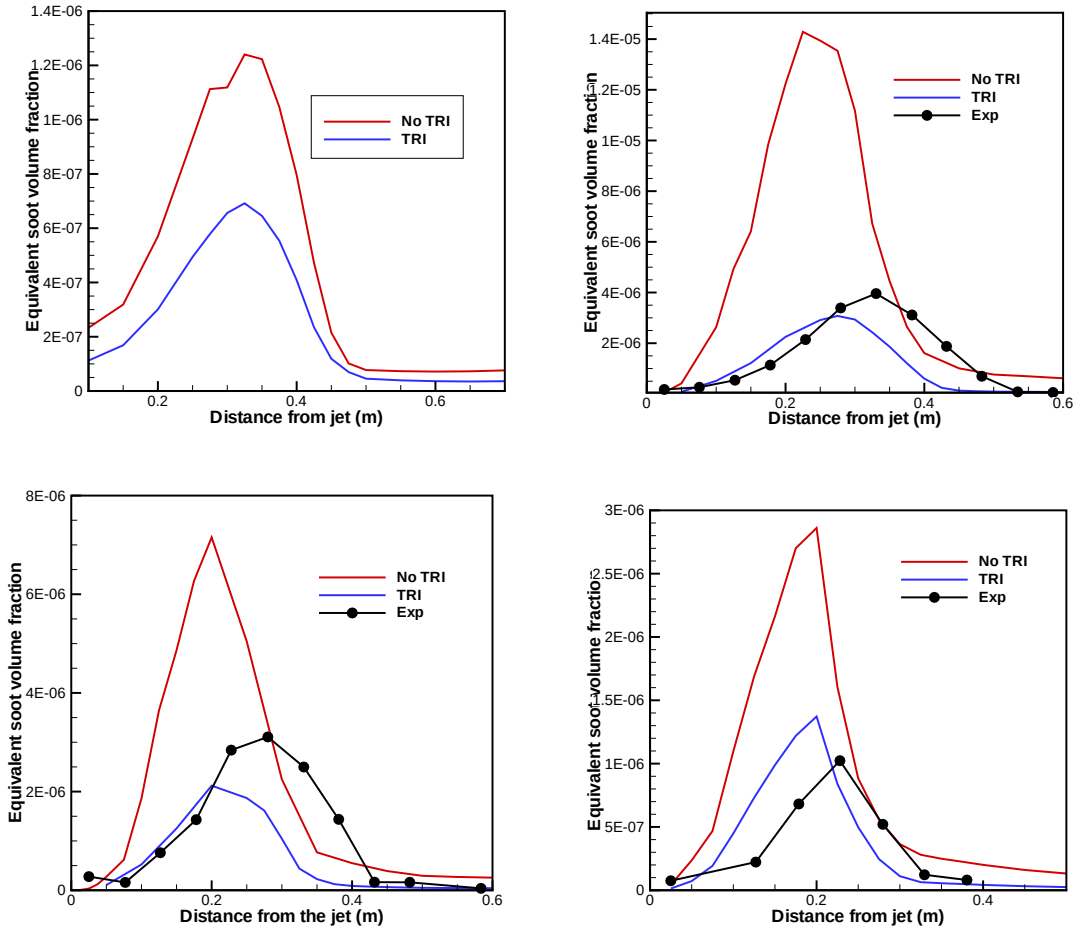

Figure. 7.4 Predicted equivalent soot volume fractions for flames III (top left), IV (top right), V (bottom left) and VI (bottom right)

Table 7.7 Comparison of key metrics for oxygen enriched flames III-VI with and without TRI

	Flame III		Flame IV		Flame V		Flame VI	
Description	TRI	No TRI	TRI	No TRI	TRI	No TRI	TRI	No TRI
Emission weighted average temperature (K)	1296	1381	1586	1682	1709	1783	1922	1978
Net radiative loss (W)	1250	853	2101	1550	2051	1598	2000	1795
Peak equivalent soot volume fraction (ppm)	0.68	1.23	3.6	14.2	2.11	7.09	1.36	2.84
Peak axial temperature (K)	1790	1840	2112	2150	2418	2451	2632	2665

7.4 Modeling a Large Flame: Flame VII

Negligible absorption TRI was reported in Section 7.2.1 for all of the flames studied here. It is expected that absorption TRI will be significant in sufficiently optically thick flames. Since Flame II (KH87) produced maximum soot volume fractions, a scaled-up flame is simulated with jet diameter $d_j = 96$ mm. The jet velocity is maintained at 52.5 m/s, while the dimensions of the mesh are also increased by a factor of 32.

Since this is a purely numerical exercise, caution should be exercised while interpreting the results. The following approximations are used and can affect the computations to a great extent.

- Buoyancy effects are neglected, even though the flame is large enough for buoyancy effects to be significant, as seen in most industrial-scale burners and large fires.

- In general, a ring of small-diameter jets is used in place of one large-diameter jet to facilitate better mixing of the fuel and oxidizer streams. This may result in different flame structure than computed here.

- Large flames exhibit vortex shedding and large unsteady structures, which cannot be captured using the RAS flow model used here.

However, even though the flame characteristics cannot be quantitatively predicted with the turbulence model used here, it is expected that the results will be qualitatively similar to those based on a more accurate model.

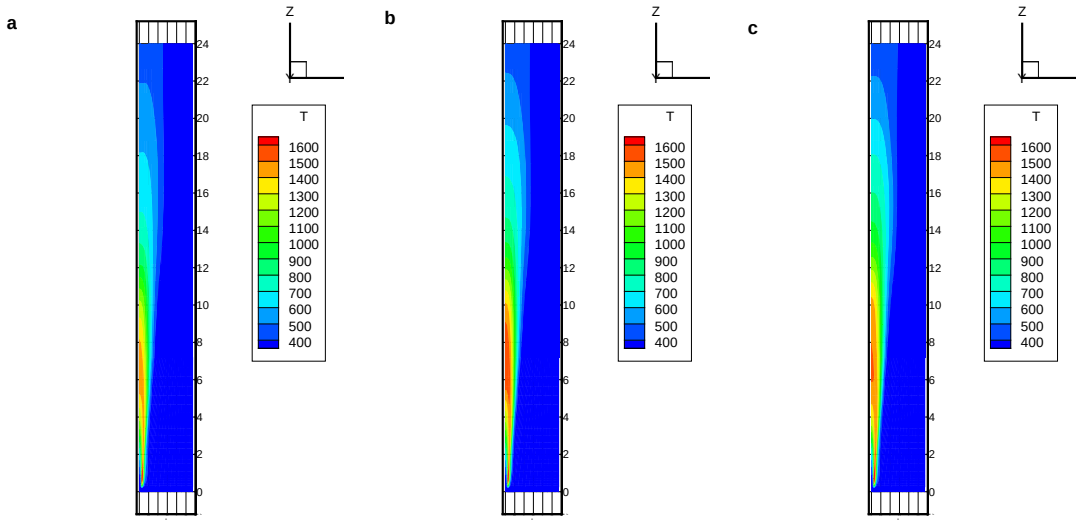

Figure. 7.5 Computed mean temperature contours for Flame-VII with different radiation treatments – a) Full TRI, b) Partial (Only emission) TRI and c) No TRI

Figure 7.5 shows the mean temperature contours of the flame using different TRI treatments with feedback to the flowfield. Figure 7.5a includes all the TRI terms, while Fig. 7.5b neglects absorption TRI. There is a large difference in the temperature distribution between figures 7.5a and 7.5b, which is solely due to a nonnegligible absorption

TRI, feeding back to the flowfield and the overall flame structure. The different models for radiative source terms feeds back to the flow field indirectly through different density fields. This happens via coupling through, temperature field, kinetic reaction rates (flame structure) and species and soot distribution. Eventually the entire solution converges into markedly different mean fields for temperature, soot and species distribution, based on each type of TRI treatment. Figure 7.5c shows temperature contours without considering any TRI. It can be seen that the temperatures are larger compared to a full TRI case. Similar plots for the converged soot volume fraction profiles are shown in Fig. 7.6. It can be seen that the soot predictions are generally different and again, the difference between Fig. 7.6a and 7.6b is entirely due to the effects of absorption TRI, which appears to be significant.

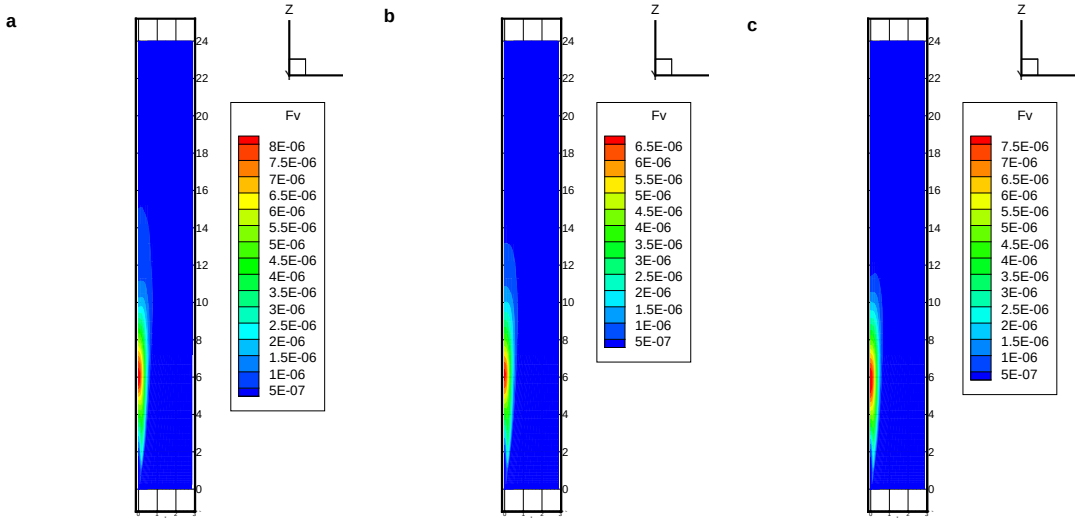

Figure. 7.6 Computed mean soot volume fraction contours for Flame-VII with different radiation treatments – a) Full TRI, b) Partial (Only emission) TRI and c) No TRI

The computed mean centerline temperatures and soot volume fractions with the different radiation treatments are shown in Fig. 7.7. It can be seen that neglecting TRI (red line) over-predicts the temperature along the entire axis. The peak axial temperature is $\sim$ 40 K higher when neglecting TRI. The results with partial TRI (i.e., only emission TRI) show higher tempertaures in some regions, than even the full TRI. It appears that absorption TRI results in an overprediction of temperature; this is discussed later in this section. However, the effects on temperature are a complex combination of soot, species and flowfield predictions Thus the net result of TRI can only be analyzed based on a frozen-field analysis as done for the other flames.

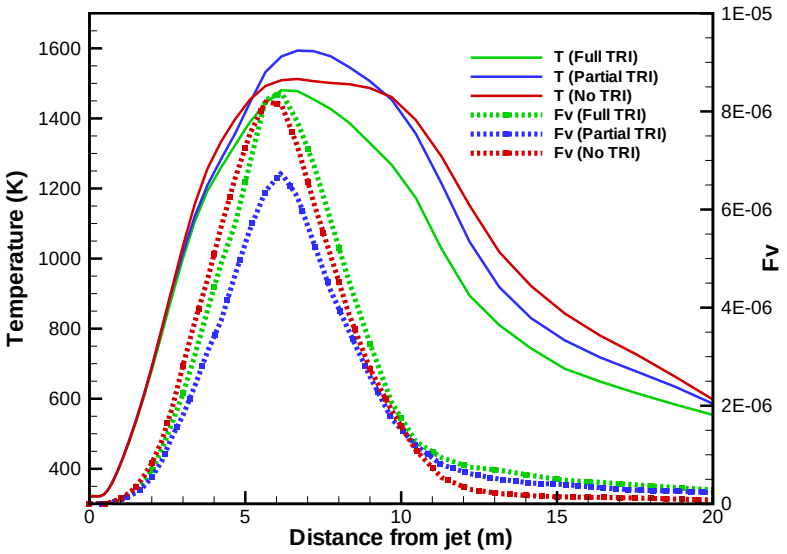

Figure. 7.7 Computed mean centerline profiles of temperature and soot volume fractions with different radiation treatments

7.4.1 Frozen field analysis

A frozen field analysis for the large Flame VII is undertaken, similar to that reported in Section 7.2.1, and global results and predictions of both emission and absorption TRI are shown in Table 7.8. It can be seen that the emission TRI contributes around $\sim 20\%$ to the total emission and this is lower than expected (recall that these values were closer to 30% in the flames studied earlier). At the same time, there is significant absorption TRI and it is negative, which is contrary to what would be expected. On the one hand, these results show that for larger flames, absorption TRI is important and needs to be accounted for. On the other hand, a negative absorption TRI is reported.

Table 7.8 Global emission, absorption and radiative loss values for Flame VII with different TRI treatments and quantitative importance of emission and absorption TRI

	Total Emission (MW)	Total Loss (MW)	Total Absorption (MW)
TRI	27.79	6.13	21.66
Emission TRI	27.79	4.87	22.92
No TRI	22.12	1.89	20.22

Table 7.9 TRI values for Flame VII: global values

	Magnitude (MW)	% based on Full TRI values	Remark
Emission TRI	5.68	20.42	Relatively low
Absorption TRI	-1.26	-5.83	Negative absorption TRI

7.4.2 Gas and Soot Radiation: Flame VII

To understand the negative absorption TRI and importance of gas and soot radiation in the overall radiative losses from the flame, the frozen field analysis is utilized to separate out gas radiation effects from overall radiation. The effects of soot radiation are then estimated by invoking an additive assumption about soot radiation as done in the previous sections.

Table 7.10 Flame VII: Importance of gas and soot emission and absorption

Total Emission (MW)	Total Loss (MW)	Gas Emission (MW)	Loss due to gases(MW)	% of gas emission lost	Soot Emission (MW)	Loss due to soot (estimate)(MW)	% of soot emission lost
27.79	6.09	8.83	1.2	13.63	18.97	4.89	25.76

Table 7.10, shows the breakdown of total radiation into gas and soot contributions. The soot emission is more than twice that of the gas-phase emission. This is in spite of the fact that the soot region is much smaller than that of the participating gases in the domain. Almost 88% of all the gas-phase emission is reabsorbed in the computational domain. This is a significantly higher number compared to a maximum $\sim 50\%$ gas-phase reabsorption in the laboratory-scale flames. Thus the optical thickness of the entire system is much higher than previously encountered. Similarly almost 75% of the soot emission is reabsorbed in the computational domain, compared to a maximum $\sim 10\%$ in laboratory-scale flames. This is mainly due to much higher mean soot volume fractions $\sim$ 10 ppm and hence a very optically thick core region near the centerline. At these optical thicknesses the often used approximations of gray gas, gray soot or optically-thin

approximations would clearly break down and, hence, cannot be used for flames with dimensions larger than Flames I–VI.

To further understand the aspects of absorption TRI, a frozen field analysis for separating TRI is also carried out with and without including soot radiation. Tables 7.11 and 7.12 show the results of separating TRI effects only in the gas-phase radiation. It can be seen that emission TRI increases total emission from the flame gases by almost $\sim 40\%$ compared to the case without considering TRI, which is comparable to values reported in the literature. There is also absorption TRI which is almost 3% of the total absorption. Thus, the absorption TRI in gas-phase radiation can be neglected reasonably. This is indeed a good result, which shows that absorption TRI are generally not important when dealing with gas-phase radiation in reacting flows, even for physcially large flames.

Table 7.11 Frozen field analysis for separating TRI: Gas-phase only

	Total Emission (MW)	Total Loss (MW)	Total Absorption (MW)
TRI	8.83	1.2	7.62
Emission TRI	8.83	1.4	7.42
No TRI	5.43	0.61	4.82

Table 7.12 TRI values for Flame VII: gas-phase radiation only

	Magnitude (MW)	% based on Full TRI values	Remark
Emission TRI	3.4	38.48	
Absorption TRI	0.2	2.6	Positive absorption TRI

Subtracting the values in Table 7.8 from Table 7.11, and invoking an additive radiation approximation, one can estimate similar quantities for the soot only. The

results are shown in Tables 7.13 and 7.14. It can be seen that the emission TRI is only

Table 7.13 Frozen field analysis for separating TRI: Soot-only (estimates)

	Total Emission (MW)	Total Loss (MW)	Total Absorption (MW)
TRI	18.97	4.93	14.04
Emission TRI	18.97	3.47	15.5
No TRI	16.69	1.28	15.4

Table 7.14 TRI values for Flame VII: soot radiation only

	Magnitude (MW)	% based on Full TRI values	Remark
Emission TRI	2.28	12.02	Relatively low emission TRI
Absorption TRI	−1.46	−10.41	Negative absorption TRI

$\sim$ 12% compared to $\sim$ 35% emission TRI seen in almost all the flames studied so far and in the gas-phase radiation seen in the current Flame VII. Negative absorption TRI $\sim$ 10% is reported for the soot. This finding is opposite to the trend seen in the gas-phase radiation. Possible reasons are discussed below.

In the optically thick limit, $\int_\Omega I d\Omega$ goes to $G \Rightarrow 4\pi I_b$, implying that $\kappa G \rightarrow 4\pi\kappa I_b$, and $\kappa' G' \Rightarrow 4\pi\kappa' I_b'$. Thus, in the optically extremely thick situations, absorption TRI must become similar to emission TRI. However, in the optically intermediate domain, when the turbulent eddies are neither optically thin to neglect absorption TRI , nor thick enough to reach the limiting solution, it is difficult to predict the behavior of absorption TRI.

Another strong possibility is that, there are regions in the flame where soot absorption coefficient (due to soot volume fractions) reduces with an increase in temperature

varies in the opposite direction of the temperature. This can happen in relatively oxygen-rich regions, where increased temperatures increase oxidation rates and reduce the soot volume fraction. Also, reduced soot volume fractions will reduce the radiative emission, thereby increasing the temperatures. Such a negative correlation is still not enough to draw emission TRI (for soot only) negative, as the temperature self-correlation more than compensates for the negative correlation. In the end, the net effect is a positive emission TRI, though much smaller than the values seen in gas-phase-only radiation. However, for absorption TRI such a compensating mechanism is not available and hence it follows the negative trend in a stronger fashion. A fruitful direction of research would be to investigate whether modifying the soot model to make it less sensitive to temperature fluctuations changes the resulting absorption TRI.

7.5 Summary

The results presented in this chapter can be summarized as follows:

- In general, turbulence–radiation interactions have strong effects on the net radiative heat loss from sooting flames. For a given temperature, species and soot distribution, TRI increases emission from the flames by 30-60%. Absorption also increases, but primarly due to the increase in emission. The net heat loss from the flame increases by 45-90% when accounting for TRI. This is much higher than the corresponding increase due to TRI in the nonsooting flames and should be noted.

- Absorption TRI was found to be negligible in laboratory-scale sooting flames with soot levels on the order of a few ppm. Modeling absorption TRI is very difficult

and needs RTE solvers like the particle-based PMC. Thus, if one could neglect absorption TRI even in sooting flames to a reasonable degree, other types of RTE solvers like the $P_1$and discrete ordinates (DOM) could be employed as long as emission TRI is properly considered.

- Soot emission was found to be as high as 70% of the total emission from the flames, even though soot is present only over a small part of the entire computational domain. Therefore, accurate soot prediction is critical for correct prediction of radiative losses from sooting flames. For small, laboratory-scale, flames, gas radiation is confined to bands and only 40-60% of gas emission actuallly leaves the domain. On the other hand, in the case of soot, more than 90% of the soot emission left the domain due to the continuum nature of the soot radiation and most of it travels through an almost transparent medium outside of the gas-bands. These results also suggest that gas radiative properties need to capture the nongray nature of absorption coefficient, but it may be possible to model soot radiative properties based on a gray approximation, for flames with lower sooting tendency.

- Simulations of sooting flames carried out without including TRI yield additional insight into the importance of TRI. Even though flames are hotter, in general, they still have smaller heat loss by at least $\sim 20\%$. The most significant effect, however, was found when comparing soot predictions. Soot was over-predicted by a factor of up to 3.5 in methane-ethylene oxygen enriched flames when neglecting TRI, but was under-predicted in the ethylene-air flames studied.

- When simulating a large flame, significant absorption TRI is seen to exist, in addition to emission TRI. Absorption TRI follows expected trends in the gas-phase radiation, and can be reasonably neglected. However there is nonnegligible, absorption TRI $\sim 10\%$ is reported in soot radiation. The net absorption TRI is then determined based on relative importance of soot and gas-phase radiation, respectively. The negative absorption TRI and a lower emission TRI in soot radiation for larger flames, could be due to regions of negative temperature-soot-volume-fraction correlations, particularly in oxygen-rich regions of the diffusion flame. In general however, nongray effects of both gas and soot radiation seem to be important along with the TRI, when modeling industrial-scale diffusion flames.

Chapter 8

Concluding Remarks

8.1 Principal Conclusions

The present work proposes a comprehensive approach for simulating turbulent reacting flows, including sooting flames. All subprocesses involved in a reacting flow are modeled in maximum detail possible today. Turbulent Reynolds stresses are closed using the standard k-ϵ model, while turbulent fluxes are modeled based on a gradient diffusion hypothesis. The composition PDF method, which allows exact closure of highly nonlinear source terms appearing in the species equations, is extended to include soot scalars, which allows an exact turbulent closure for the highly nonlinear soot subprocesses and their interaction with the gas phase. This represents a significant advance in the state-of-the-art of modeling turbulent reacting flows.

A Lagrangian particle Monte Carlo method is used to solve the transported PDF equations, as it can accomodate the high dimensionality of the problem with relative ease. Detailed kinetics are used to accurately model the gas-phase chemistry coupled with the detailed soot model. Radiation is calculated using a particle-based PMC method and is coupled with the transported PDF method and soot model to accurately account for both emission and absorption TRI, using line-by-line databases for radiative properties of CO_2 and H_2O ; soot radiative properties are also modeled as nongray.

To make progress in soot modeling for luminous turbulent flames, reaction mechanisms are validated systematically in configurations where the effects of TCI and TRI are absent. To this end, a comprehensive modeling study of soot formation in laminar flames is performed. The scope was limited to atmospheric-pressure ethylene–air flames and to soot modeling based on a method of moments. Both premixed flames and opposed-flow diffusion flames are considered with variations in gas-phase mechanisms and soot model parameters. The key sensitivities of the soot models allowed identification of certain combinations, which yielded satisfactory results in laminar flames.

The transported PDF method coupled with a detailed gas-phase chemistry, soot model and RTE solver applied to various jet flames with Reynolds numbers varying from $\sim$ 6700 to 15100. Two ethylene–air flames and four flames with a blend of methane–ethylene and enhanced oxygen concentration are simulated. All model parameters are kept constant including those for i) soot submodels, such as surface-reaction rates, ii) mixing model constants in transported PDF methods, iii) PMC model constants, such as rays-per-particle, ray opening angle, etc., iv) turbulence model constants, like those in the k-ϵ equations etc. Except for the well-established turbulence model, all other processes are simulated using advanced models for chemistry, TCI, radiative properties and RTE equation. The results show excellent agreement between experimental and computed temperature levels for almost all the flames. For some flames, computed peak temperature occured upstream of the experiments, which may be due to a relatively inaccurate turbulence model, resulting in over-prediction of jet-spreading rates. Even though the soot model was validated only in ethylene–air flames, it performs very well even in oxygen-enriched flames and with 90% methane in the fuel stream. The soot

predictions for all the flames considered are within a factor of 1.75 as a most conservative estimate. This implies a significant progress in the current soot modeling capabilities for turbulent sooting flames.

Radiative flux computations show very good agreement with the available experimental data. This seems to be the combined effect of better radiative property model (line-by-line) and RTE solver (PMC) along with accurate accounting for both emission and absorption TRI. In general, turbulence–radiation interactions can have a tremendous effect on the net radiative heat loss from sooting flames. For a given temperature, species and soot distribution, TRI increases emission from the flames by 30-60%. Absorption also increases, but primarily due to the increase in emission. The net heat loss from the flame increases by 45-90% when accounting for TRI. This is much higher than the corresponding increase due to TRI in nonsooting flames. Absorption TRI was found to be negligible in the laboratory scale sooting flames with soot levels on the order of a few ppm. Modeling absorption TRI is very difficult and requires high-level RTE solvers like the particle-PMC. If one can neglect absorption TRI even in sooting flames to a reasonable degree, simpler/cheaper RTE solvers like the P_1 and DOM can be employed, as long as emission TRI is properly considered. This would simplify the radiation analysis of reacting flows. As an extension it may be possible to ignore absorption TRI in configurations comparable to the current study. Soot emission was found to be as high as 70% of the total emission, even though soot is present only in a small part of the entire computational domain. Therefore accurate soot modeling is critical for correct prediction of radiative losses from the flame. Gas radiation occurs only across specific bands and only 20-60% of the gas emission actually leaves the domain. In the case of

soot, more than 90% of the soot emission left the domain due to the continuum nature of the soot radiation, in case of laboratory-scale flames, while only about 25% soot emission was lost in case of the larger flame with highly optically thick soot core. The simulations of sooting flames carried out without including the TRI yields additional insight into the importance of TRI. The flames are hotter in general, still underpredicting heat loss by up to $\sim 20\%$. The most significant effect, however, was on soot predictions. Soot was over-predicted by up to a factor of 3.5 in the methane–ethylene oxygen-enriched flames while under-predicted in the ethylene–air flames studied.

8.2 Future Work

There remain avenues for improvements and modifications to the current approach. The most relevant possibilities are now discussed in brief.

8.2.1 Soot Modeling

The method of moments has shown very good predictive characteristics. However, it is based on the assumption of spherical particles and coalescent coagulation. Both these assumptions are used for ease of computations. The method of moments formulation can be extended to include nonspheriodal soot particles charactertized by a modeled "fractal dimension." A key limitation of the method of moments is its inability to account for a bimodal (or multimodal) PSDF. Sectional methods can potentially resolve the entire PSDF based on its discrete approximation. They also have the additional advantage of being able to naturally account for a multimodal PSDF and nonspherical geometries. These can be assessed in laminar flames and then applied to turbulent flames using a

similar approach as in the current study. In fact, the framework developed in the current work is flexible enough to allow for newer soot models to be added with relatively small amount of effort.

8.2.2 Radiation Modeling

The PMC method used in the current study included LBL gas radiative properties. A key limitation of this approach is the fact that the LBL databases occupy almost 95% of the memory (on each processor), while just considering CO_2 and H_2O as the participating gases. Including additional species like CO and fuels like CH_4 and C_2H_4 would make it prohibitively memory-intensive. The effect of these additional gases as participating media also needs to be studied rigorously. A fruitful direction of research would be to create random-number wavenumber relationships for various species and obtaining compact memory storage using various data-reduction, functional approximation techniques for the line-by-line lookup tables. This would pave the way for using LBL accuracy with, a much smaller memory footprint than currently possible.

The PMC based on full-spectrum k-distributions uses almost two orders of magnitude less memory compared to the LBL PMC and can be used when additional species need to be included. Although the PMC based on k-distributions performs statistically similar to the LBL method, it suffers from inaccuracies associated with the FSK method and inhomogeneity (temperature and concentration) of the participating medium. Another direction of research would be to extend the current PMC to incorporate the multigroup, multiscale k-distribution model being developed by Modest and coworkers.

The current PMC method can also trace multiple wavenumbers on a single photon bundle. It should be possible to modify the implementation so that each photon bundle carries one wavenumber for each participating medium. This would increase the time needed to trace each bundle, but also allow a much better resolution of the emission (and absorption) spectrum for the entire flow-field. However, it will simplify the inversion of random-number relationships for each wavenumber as they would now depend on single species instead of species mixtures. This has implications when dealing with problems involving many more radiating species than just the combustion gases. For example in hypersonic re-entry problems, there may be as many as ten participating species. In addition, it would also allow new insight into the radiation characteristics of reacting flows in general.

8.2.3 Turbulent Closure

The k-ϵ model is used here to obtain closure for the turbulent Reynolds stresses and turbulent diffusivity for species and enthalpy. The standard k-ϵ model is known to have limitations when dealing with complex flow configurations and even with axisymmetric jets with strong density changes. More advanced Reynolds stress models (RSM) are computationally expensive, have numerical robustness issues and involve many more "model constants", which are nonintuitive to tune.

Large Eddy Simulation (LES) has become tractable over the past few years with the increasing computing power available to researchers. LES has been highly successful in predicting nonreacting flows in very complex configurations with remarkable accuracy. It has also been successful in the field of reacting flows. The filtered density function

(FDF) method is based on similar principles as the transported PDF method. It can obtain accurate closure with arbitrary chemistry, can be extended to handle soot scalars and seems to be a logical extension for the current state of the art. It may then be possible to handle complex flows like pool fires, unsteady combustion processes and effect of TRI on their evolution, etc.

8.2.4 Pollutant Formation

The influence of soot, radiation, chemistry, etc on various pollutants such as unburned hydrocarbons (UHC), CO and NO_x was not a part of the current study. However, with the current framework, addition of suitable nitrogen chemistry to the gas-phase reaction mechanisms should allow a detailed evaluation of the effect of soot and radiation on NO_x formation and other pollutants. These are also important when dealing with IC engines and can be studied as a part of future work.

8.2.5 Detailed Chemistry

Chemistry calculations consume more than 95% of the computational resources even with a moderate-sized mechanism consisting of 33 species, which was used in the current study. For higher-molecular-weight fuels like propane, heptane, etc., the detailed chemistry mechanisms, when available, are even larger. Large numbers of species and stiffness of the ODE system needed to solve for the species source terms makes it prohibitively expensive to use larger chemistry models in context of the transported PDF methods. Addition of soot scalars makes the problem even more difficult. There are multiple ways to tackle this problem. Accurate reduced chemistry mechanisms can be

developed and validated for applications in turbulent codes. Storage retrieval schemes like DOLFA and ISAT have been used successfully, making the chemistry calculations tractable in complex configurations. However, addition of soot scalars to the lookup tables needs more work. This is due to the fact that soot formation time-scales are different from the chemical time-scales and may not be captured accurately when evaluated based on look-up tables. A different way of achieving faster chemistry calculations would be to use artificial neural networks to obtain the chemical source terms for the particles [167]. A particular class of neural networks, RBF-Nets may be more suitable for use in source term approximation than the conventional sigmoid-transfer-function based networks, which are known to have certain limitations when applied in chemistry acceleration type problems [168]. This is also left as a topic for further research.

Appendix A

Method of Moments Formulation

The time evolution of a particle ensemble is described by population balance equations known as the "Smoluchowski master equations" [109, 110]. These can be written as,

$$\frac{dN_1}{dt} = -\sum_{j=1}^{\infty} \beta_{1,j} N_1 N_j \tag{A.1a}$$

$$\frac{dN_i}{dt} = \frac{1}{2}\sum_{j=1}^{i-1} \beta_{j,i-j} N_j N_{i-j} - \sum_{j=1}^{\infty} \beta_{i,j} N_i N_j \qquad i = 2 \ldots \infty. \tag{A.1b}$$

Here, N_i denotes the number of particles of size i per unit volume: i.e., size i particle number density. N_1 is the number density of the smallest particles and $\beta_{i,j}$ is the collision coefficient between particles of size i and j. In general, then, $\beta_{i,j} = \beta_{i,j}(N_i, N_j, m_i, m_j)$ where m_i is the mass of particle of size i.

The concentration moment of the particle number density function N_i is

$$M_r = \sum_{i=1}^{\infty} m_i^r N_i. \tag{A.2}$$

It can be seen that if $r = 0$, then $M_0 = \sum_{i=1}^{\infty} N_i$ is the total particle number density. For $r = 1$, $M_1 = \sum_{i=1}^{\infty} m_i N_i$ is the total mass of particles per unit volume, so that the volume fraction is given by $f_v = M_1/\rho_s$. Higher order moments may lack a simple physical interpretation but are needed for accuracy. It can be seen that the knowledge of

all integer moments ($r = 0, \ldots, \infty$) is equivalent to the knowledge of the size distribution function itself. However, most of the principal properties for the particle ensemble can be deduced from the first few moments.

Multiplying Eqs. (A.1a) and (A.1b) by m_i^r and summing over all size classes $i = 1, \ldots, \infty$ results in a general form of equations given by [123]

$$\frac{d}{dt}\left[\sum_{i=1}^{\infty} m_i^r N_i\right] = G_r \quad r = 0, \ldots, \infty \tag{A.3}$$

In this case, $G_1 = 0$ since the total mass of the particles does not change during evolution. However when one adds processes such as surface reactions, nucleation etc., this does not remain the case. With an assumption $m_i = im_1$, it can be shown that,

$$G_0 = \frac{1}{2}\sum_{i=1}^{\infty}\sum_{j=1}^{\infty}\beta_{i,j}N_iN_j \tag{A.4a}$$

$$G_r = \frac{1}{2}\sum_{k=1}^{r-1}\binom{r}{k}\left(\sum_{i=1}^{\infty}\sum_{j=1}^{\infty}m_i^k m_j^{r-k}\beta_{i,j}N_iN_j\right) \tag{A.4b}$$

The collision coefficient $\beta_{i,j}$ is nonadditive and its functional form depends on the coagulation regime, which is generally classified based on the Knudsen number, $\mathrm{Kn} = 2\lambda_f/d$, where λ_f is the mean free path (for particle collision) and d is the particle diameter. There are three regimes from a coagulation point of view: the continuum regime with a large d so that $\mathrm{Kn} \ll 1$, the free-molecular regime with a small d where $\mathrm{Kn} \gg 1$, and the transition regime in between. While dealing with soot aggregates,

similar considerations are made using a characteristic length scale instead of d for the aggregate.

A.1 Particle coagulation

Physically, particle coagulation is a process in which small particles (assumed to be spherical) collide with each other and coalesce completely to form larger spherical particles. It has been found in kinetic molecular dynamics (KMD) simulations that small particles are indeed spheroidal and the assumption of spherical particles seems to be reasonable [111, 126]. After a certain size, however, the particles cannot coalesce completely and start to form long chains, which eventually grow into three-dimensional fractal-like structures. This is particle aggregation and will be treated later on.

Particle coagulation can be modeled in the two limits of continuum and free-molecular regimes, i.e., the functional form of $\beta_{i,j}$ can be derived and transformed for use in the moment equations A.4.

A.1.1 Continuum regime

In the limit of $\mathrm{Kn} \ll 1$ the collision coefficient for coalescent collisions of spherical particles is given by [110]

$$\beta_{i,j}^{\mathrm{contm}} = K_c \left(\frac{C_i}{m_i^{1/3}} + \frac{C_j}{m_j^{1/3}} \right) \left(m_i^{1/3} + m_j^{1/3} \right) \tag{A.5}$$

where $K_c = 2k_BT/3\eta$, C is the Cunningham slip correction factor expressed as $C = 1+1.257\text{Kn}$ [127, 169], k_B is the Boltzmann constant and $\eta = 1/\lambda$. Substituting Eq.(A.5) into Eq.(A.4) leads to

$$G_0^{\text{contm}} = K_c \left[M_0^2 + M_{1/3}M_{-1/3} + K_c' \left(M_{-1/3}M_0 + M_{1/3}M_{-2/3} \right) \right], \tag{A.6}$$

where $K_c' = 2.514\lambda(\pi\rho/6)^{1/3}$, λ is the molecular mean free path, ρ is the particle material density and the definition of moments is now extended to any real value r. For convenience, reduced moments of the PSDF are written as

$$\mu_r = M_r/M_0. \tag{A.7}$$

Then Eq.(A.6) can be written as

$$G_0^{\text{contm}} = K_c M_0^2 \left[1 + \mu_{1/3}\mu_{-1/3} + K_c' \left(\mu_{-1/3} + \mu_{1/3}\mu_{-2/3} \right) \right]. \tag{A.8}$$

A similar analysis for arbitrary values r from Eq.(A.4) using $\beta_{i,j}$ from Eq.(A.5) results in [123, 125]

$$\begin{aligned} G_r^{\text{contm}} = \; & K_c M_0^2 \textstyle\sum_{k=1}^{r-1} \binom{r}{k} [2\mu_k\mu_{r-k} + \mu_{k+1/3}\mu_{r-k-1/3} + \\ & \mu_{k-1/3}\mu_{r-k+1/3} + K_c^{'}(\mu_{k-1/3}\mu_{r-k} + \mu_k\mu_{r-k-1/3} + \\ & \mu_{k+1/3}\mu_{r-k-2/3} + \mu_{k-2/3}\mu_{k+1/3})] \end{aligned}$$

The evaluation of fractional-order moments is done by an interpolation scheme within the integer-order moments. Details are given in section A.4.

A.1.2 Free-molecular regime

In the free-molecular regime $Kn \gg 1$, the collision coefficient for the coalescent particles is given by [110]

$$\beta_{i,j}^{\text{free}} = K_f \sqrt{\frac{1}{m_i} + \frac{1}{m_j}} \left(m_i^{1/3} + m_j^{1/3} \right)^2, \tag{A.9}$$

where $K_f = \epsilon\sqrt{6k_BT/\rho}(3/4\pi\rho)^{1/6}$. Here ϵ is the Van Der Waals enhancement factor which should be a function of particle sizes but can be taken as a constant without much loss of accuracy. Introducing this form of $\beta_{i,j}$ into the moment equations is much more difficult due to the nonadditive summations appearing in Eq.(A.4). This difficulty is overcome by utilizing a double interpolation scheme by defining a grid function [125, 127]

$$f_l^{x,y} = \sum_{i=1}^{\infty}\sum_{j=1}^{\infty}(m_i + m_j)^l m_i^x m_j^y (m_i^{1/3} + m_j^{1/3})^2 N_i N_j \tag{A.10}$$

The grid function can be (relatively) easily evaluated when l are integers. However, values at fractional l are needed in the growth rate terms G_r and are interpolated using a scheme detailed later. Then Eq.(A.4) in the free-molecular regime takes the form

$$\begin{aligned} G_0^{\text{free}} &= \tfrac{1}{2} K_f M_0^2 f_{1/2}^{0,0} \\ G_r^{\text{free}} &= \tfrac{1}{2} K_f M_0^2 \textstyle\sum_{k=1}^{r-1} \binom{r}{k} f_{1/2}^{k,r-k}, \quad r = 2, 3, \ldots . \end{aligned}$$

A.1.3 Transition regime

In the transition regime, an approximate coagulation rate is used as the harmonic mean of the limit values so that,

$$G_r^{\text{transition}} = \frac{G_r^{\text{free}} G_r^{\text{contm}}}{G_r^{\text{free}} + G_r^{\text{contm}}} \quad r = 0, 2, 3, \ldots \tag{A.11}$$

The error is generally less than 20% and is deemed satisfactory in most applications [127].

A.2 Particle nucleation

Particle nucleation is the most important step in soot formation and results in generation of the smallest size particles N_1. A general equation for this can be written as [123, 127]

$$\frac{dN_1}{dt} = R_{N_1} - G_{N_1} - \frac{k_s s_1}{\Delta m} N_1 \tag{A.12}$$

where R_{N_1} is the chemical pathway for generating the smallest soot particles, G_{N_1} is the reduction of these particles by coagulation with other particles, and the last term on right-hand-side is the destruction of these particles by surface reactions (oxidation by O_2 and OH molecules) modeled using a reaction rate k_s per unit area and s_1 is the surface area of the smallest particle.

The nucleation rates need to be transformed for use in the moment equations so that the moment equations take the form

$$\frac{dM_r}{dt} = R_r + G_r \tag{A.13}$$

A simpler implementation of this is available in [129, 130] as

$$R_0 = \epsilon\sqrt{\frac{4\pi k_B T}{m_C N C_{\mathrm{PAH}}}} d^2_{\mathrm{PAH}} N_{\mathrm{PAH}} N_{\mathrm{PAH}} \tag{A.14a}$$

$$R_r = 2NC_{\mathrm{PAH}} R_{r-1} \tag{A.14b}$$

where NC_{PAH} is the number of carbon atoms per PAH molecule, m_C is the mass of carbon molecule C_2 and N_{PAH} is the number density of the PAH molecules involved in soot nucleation. The diameter of the PAH molecule and other properties can be calculated. N_{PAH} can be obtained from the molar concentration of the PAH species.

Lindstedt and coworkers [131, 132] assumed a very simple nucleation step given by

$$R_r = 2\frac{N_A}{C_{\mathrm{min}}} k_N(T)[\mathrm{C_2H_2}], \quad r = 0, 2, 3, \ldots, \tag{A.15}$$

where N_A is the Avogadro's constant and C_{min} is the number of carbon molecules in the smallest PAH which coagulates into a dimer to form the incipient soot particle.

Many other nucleation rate models are available but are generally used to solve for the soot volume fraction directly. All these models are empirical and cannot be directly applied in the context of the moment methods considered here.

A.3 Surface reactions: spherical particles

The simplest case is to consider spherical particles so that the surface area is a direct function of the particle diameter. Using the kinetic mechanism of H-abstraction-acetylene-addition [104] shown in Table 4.1, it can be shown that with one surface growth reaction, a mass equivalent to two carbon atoms is added to a (soot) particle. The mass of hydrogen is generally neglected without any serious error in the formulation [104]. Thus $\Delta m = 2m_C$ can be used in Eq.(4.16). The surface area of the particle is calculated with the assumption $m_i = im_1$ so that one obtains [104, 125, 127]

$$W_r^{\text{coag}} = k_{sg} C_g \alpha \chi_s \pi \left(\frac{6m_C}{\pi \rho_s}\right)^{2/3} M_0 \sum_{k=0}^{r-1} \binom{r}{k} \Delta^{r-k} \mu_{r+2/3} \quad r = 1, 2, \ldots, \tag{A.16}$$

where k_{sg} is the kinetic rate coefficient for reaction with gas g, C_g is the molar concentration of the gas species, α is a stearic factor as explained below, χ_s is the nominal number density of surface radical sites, Δ is the number of carbon atoms added/removed from the particle due to reaction with gas g, m_C is the mass of the carbon atom and ρ_s is the density of soot generally taken as 1.8 g/cm^3 [104]. There are a multitude of approximations/assumptions in Eq.(A.16), which are summarized as

- The surface growth is assumed to occur due to the reactions of C_2H_2 with surface radicals, and condensation of PAH on the particle surface, and the surface oxidation due to reactions of O_2 with surface radicals and reactions of OH with the particle surface. These reactions are assumed to be analogous, at each active site on the particle surface, to the corresponding gaseous reactions of large PAH molecules [104].

- k_{sg} is the reaction rate for the modeled reaction of the soot with a participating gaseous species g, which is one of the species on the right-hand-side of reactions shown in Table 4.1.

- C_g is the molar concentration of the gaseous species.

- χ_s is the number density of the surface radical sites, which is determined from the number density of total surface sites, which in turn are estimated to be 2.5×10^{15} cm^{-2} [107]. A kinetic steady-state approximation is then used to obtain the total radical sites available on the particle for reactions with gas-phase species which is given by $\chi_s = K_{\mathrm{steady}} \chi_{\mathrm{all}}$ [104].

- The factor α is the fraction of the surface sites available for chemical reactions, and was introduced into the equations by Frenklach and Wang [107] to account for the difference between the soot surface growth rates in low- and high-temperature flames [15]. It was suggested that α quantifies the changing morphology of the soot particle surface as it travels in the post-flame region and that the extent of this change is dependent on the particle surface temperature. The physical rationale is that α considers the growing soot surface to have "graphitic" edges amenable to chemical reactions, but some parts are comprised of nonreactive basal aromatic planes [15]. The temperature-dependent α-model for surface growth was confirmed by Faeth and coworkers in the postflame regions of laminar premixed flames [116, 117].

- The functional form for α has been evolving over the years starting with constant values [104, 106] to a temperature-dependent value used by Appel et al. [15]

$$\alpha = \tanh[a(T)/\log \mu_1 + b(T)]. \tag{A.17}$$

By comparing experimental results from seven laminar premixed flames from different investigators, they were able to deduce $a(T)$ and $b(T)$ as linear functions of local temperature T.

A.4 Interpolation Schemes

The rate expressions of the moments contain fractional-order moments which are obtained using an interpolation scheme. The positive-order fractional moments can be computed by Lagrange interpolation among the logarithms of integer-order moments i.e., [123, 125]

$$\log \mu_p = L_p(\log \mu_0, \log \mu_1, \ldots, \log \mu_{r\max}) \tag{A.18}$$

where L_p represents Lagrange interpolation with respect to p and $\mu_{r\max}$ is the maximum integer-order moment being solved. The negative-order fractional moments are computed by slight extrapolation of the first three moments in a similar manner. Some of the equations also need a slight extrapolation beyond $r_{\max}$. However, Frenklach [123] reports that the $\log \mu_r$ vs. r dependence is very close to linear above about $r = 3$. Thus the extrapolation is not expected to produce significant errors.

In the equations for the free-molecular regime (see Eqs. (A.9) and (A.10)), there are summations which need to be resolved using a double interpolation scheme. The

grid function Eq.(A.10) can be evaluated exactly in terms of fractional-order moments for integer values of l. This is the first level of interpolation so that $f_l^{x,y}$ can be evaluated for integer l and integer x, y. Then for any fractional value of l, another level of interpolation is made; for example, if $l = 1/2$, then

$$\log f_{1/2}^{x,y} = L_{1/2}(\log f_0^{x,y}, \log f_1^{x,y}, \log f_2^{x,y}) \tag{A.19}$$

where $L_{1/2}$ indicates the Lagrange interpolation polynomial. Frenklach [123] reports a set of parameterization of the grid functions for the five-moment model which gives smaller error, found by trial and error.

Appendix B

Concurrency and Parallelism

B.1 Introduction

In order to attain reasonable turn-around times for CFD simulations, it is imperative to develop programs that can take advantage of multi-processor systems. In this context, two concepts of concurrency and parallelism are of importance. Concurrency is a programming paradigm and is written such that various tasks can potentially be carried out simultaneously. The program executed serially or in parallel must obtain identical results. The execution of concurrent tasks on a multi-processor system is termed parallelism. In general, existence of concurrency in a program model can be exploited to achieve parallelism and hence a performance gain. The parallelism can be achieved in a shared memory model (where all the processing units share the memory) or a distributed memory model. In the current work, we have used the distributed memory model with most of the machines running a Beowulf cluster. The Message Passing Interface (MPI) method is used for inter-process communication. In the current work, the parallelization efforts proceeded from the most expensive to the least expensive, with different algorithms used for best performance gains, compared to single-processor simulations.

B.2 Computing Resources

The simulations were carried out on a variety of machines listed in Table B.1. The last column lists the speed ranking. In addition, LION-XB and LION-XC also use different interconnects – Gigabit ethernet and Infiniband, respectively.

Table B.1 Computing resources used in current study

Name	CPU	Clock (GHz)	L2-Cache (MB) per Proc.	Proc. per Node	Speed Ranking
LION-XC	64-bit	3.0	2.0	4	1
MARA	64-bit	2.0	2.0	8	2
LION-XB	64-bit (Opteron)	2.0	1.0	8	3
LION-XM	32-bit	3.0	0.5	8	4
MICHELLE	32-bit	1.4	0.5	2	5

MARA is quad-core, dual processor, Intel XEON machine and as such all the computing cores reside on the same node. The MPI efficiency is studied on MARA for up to 8 processors. Similar performance was observed on all the compute clusters with slightly more performance degradation when run on CPUs hosted on physically different nodes, mainly due to network latency. The breakdown of computing resource requirement for various tasks in the simution and parallelization algorithms is discussed in the following sections.

B.3 Parallel Implementation

The task breakdown for reacting flow simulations in the context of composition PDF methods used in the current work is shown in Table B.2. The mean velocity field

is obtained using the code AC-FluX and includes the k-ϵ turbulence model. The total effort for the flow solution is less than 0.5% of the total computing time on a single processor and, hence, it was not parallelized. This limits the use of the current code on mesh sizes, such that they can fit in the memory on a single node. .

Table B.2 Task breakdown in reacting flow simulations

Description	Parallel Implementation	Remark
Flow Solution	No	Limited to meshes that can fit on single node
Chemical Reactions	Yes	Embarassingly parallel algorithm possible
Photon Monte Carlo	Yes	Efficient parallel algorithm posisble
Mixing model (EMST)	Yes	Adaptive parallel algorithm
Particle tracking	No	Future work

Modeling chemical reactions in context of the PDF methods is one of the most computationally expensive sections of the code. The pre-existing algorithm relied on dividing the FV cells serially onto different processors. The particles in those cells were also communicated to the corresponding cells and chemistry calculations were carried out on each processor. However, for jet-flame configurations this approach yields lower efficiency than possible by loading fewer processors with relatively high tempereature cells. A new algorithm was implemented, in which particles are assigned to the processors in a round-robin fashion. This resuls in a complete load balancing with almost linear speed up.

The details of PMC parallelization are given by Wang [96]. All the particles' compositions and positions need to be available on all the processors and are communicated at the start of each PMC iteration. This is followed by a uniform random assignment of particles to the processors. Each processor traces rays emitted from the corresponding particles. The net enthalpy change for all particles is collected over all the processors at the end of each ray-tracing step.

The EMST mixing model is relatively expensive (by ~ 3 orders of magnitude) compared to the CD model (Chapter 2). The computing time needed to evaluate micro-mixing using EMST in a cell is a strong function of i) size of composition space, ii) number of particles in a cell and iii) turbulent frequency/time-scale (k/ϵ) in the cell. For a turbulent jet-flame configuration, the turbulent time-scales are smallest in a narrow region near the jet exit. The cells in and near these high turbulent frequency regions dominate the overall computing times needed for mixing. Dividing FV cells equally across all processors does not result in performance improvement, due to concentration of the high-turbulent-frequency cells over fewer processors than available. In the current work a new algorithm for parallelizing the mixing model was implemented. The algorithm can be summarized as follows

1. Collect time needed for calculating EMST in each FV cell. This is achieved by either a serial implementation or a unifrom cell distribution.

2. Build a (discrete) cumulative distribution function (CDF) of the time needed for computing EMST for all the FV cells involved.

Table B.3 Parallelization efficiency for various modules in the code

Processors	Reactions		MCRT	
	Time	$\epsilon_{\text{parallel}}$	Time	$\epsilon_{\text{parallel}}$
1	222.64	1.000	72.11	1.00
2	111.76	0.996	36.76	0.98
4	56.10	0.992	18.86	0.96
8	27.99	0.994	9.84	0.92
	Mixing		Other	
	Time	$\epsilon_{\text{parallel}}$	Time	$\epsilon_{\text{parallel}}$
1	7.5	1.000	1.54	1.00
2	3.84	0.98	1.57	0.49
4	2.53	0.74	1.55	0.25
8	1.27	0.74	1.55	0.12
	Total Simulation			
	Time		$\epsilon_{\text{parallel}}$	
1	304.14		1.00	
2	155.36		0.98	
4	79.47		0.96	
8	41.14		0.92	

3. The cells are divided such that approximately $1/N_p$ of the CDF from the previous timestep is allocated to each processor, where N_p is the number of processors used in the computations.

The parallelization efficiency can be defined as

$$\epsilon_{\text{parallel}} = \frac{T_1}{N_p \times T_p}. \tag{B.1}$$

where T_i indicates cpu time when using i processors. Table B.3 lists the parallel efficiency of various parts of the current code, as reported on MARA. Since all processors are on the same physical machine, it is likely that network latency does not affect the efficiency on these machines. Chemistry constitutes more than 70% of the effort in presence of

a high PMC effort and more than 90% of the total effort in the presence of a low-to-moderate PMC load. An almost embarassingly parallel efficiency of more than 99% is possible for the chemistry due to a round-robin parallelization algorithm. The PMC shows good parallelization properties resulting in a good over-all performance gain using multiple processors.

The overall efficiency was seen to degrade on the clusters using the 1 giga-bit interconnect. However, most of the clusters at The Pennsylvania State University now use the Infiniband interconnect and provide almost similar speed-up values as those reported here. It should be possible to linearly extrapolate these curves to 32 processors, but caution should be used beyond that.

Bibliography

[1] M. F. Modest, *Radiative Heat Transfer* (2nd Edn), Academic Press, New York (2003).

[2] I. M. Kennedy, Models of Soot Formation and Oxidation, *Progr. Energy Combust. Sci.* 23, 95–132 (1997).

[3] D. Veynante and L. Vervisch, Turbulent Combustion Modeling, *Progr. Energy Combust. Sci.* 28, 193–266 (2002).

[4] G. M. Faeth, J. P. Gore, S. G. Chuech and S. M. Jeng, Radiation from Turbulent Diffusion Flames, In *Annual Review of Numerical Fluid Mechanics and Heat Transfer*, Vol. 2, pp. 1–38. Hemisphere, Washington, D.C. (1989).

[5] M. E. Kounalakis, J. P. Gore and G. M. Faeth, Mean and Fluctuating Radiation Properties of Nonpremixed Turbulent Carbon Monoxide/Air Flames, *J. Heat Transfer* 111, 1021–1030 (1989).

[6] J. P. Gore and G. M. Faeth, Structure and Spectral Radiation Properties of Turbulent Ethylene/Air Diffusion Flames, *Proc. Combust. Inst.* 21, 1521–1531 (1986).

[7] P. J. Coelho, Numerical simulation of the interatction between turbulence and radiation in reactive flows, *Progr. Energy Combust. Sci.* 33(4), 311–383 (2007).

[8] T.H. Song and R. Viskanta, Interaction of Radiation with Turbulence: Application to a Combustion System, *J. Thermoph. Heat Transfer* 1, 56–62 (1987).

[9] R. J. Hall and A. Vranos, Efficient Calculations Of Gas Radiation From Turbulent Flames, *Int. J. Heat Mass Transfer* 37(17), 2745–2750 (1994).

[10] S. Mazumder and M. F. Modest, A PDF Approach to Modeling Turbulence–Radiation Interactions in Nonluminous Flames, *Int. J. Heat Mass Transfer* 42, 971–991 (1999).

[11] G. Li and M. F. Modest, Investigation of Turbulence–Radiation Interactions in Reacting Flows Using a Hybrid FV/PDF Monte Carlo Method, In *Proceedings of the ICHMT 3rd International Symposium on Radiative Transfer* (Edited by M. P. Mengüç and N. Selçuk), Antalya, Turkey (2001).

[12] G. Li and M. F. Modest, Numerical simulation of turbulence-radiation interactions in turbulent reacting flows, In *Modelling and Simulation of Turbulent Heat Transfer* (Edited by B. Sunden and M. Faghri), WIT Press, Southampton, England (2004).

[13] M. F. Modest and R. S. Mehta, Modeling Absorption TRI in Optically Thick Eddies, In *Proceedings of Eurotherm 78 - Computational Thermal Radiation in Participating Media II*, Elsevier,Poitiers, France (5–7 April, 2006).

[14] A. Wang and M. F. Modest, Spectral Monte Carlo models for nongray radiation analyses in inhomogeneous participating media, *Int. J. Heat Mass Transfer* 50(19-20), 3877–3889 (2007).

[15] J. Appel, H. Bockhorn and M Frenklach, Kinetic Moldeing of Soot Formation with Detailed Chemistry and Physics: Laminar Premixed Flames of C_2 Hydrocarbons, *Comb. Flame* 121, 122–136 (2000).

[16] D. C. Haworth and T. J. Poinsot, Numerical Simulations of Lewis Number Effects in Turbulent Premixed Flames, *Comb. Flame* 104, 111–137 (1996).

[17] A. Juneja and S. B. Pope, A DNS study of turbulent mixing of two passive scalars, *Phys. Fluids* 8, 2161–2184 (1996).

[18] M. Ulitsky, C. Ghenaï, I. Gökalp, L. P. Wang and L. R. Collins, A comparison of a spectral EDQNM model for premixed turbulent flame propagation to DNS and experiments, *Combust. Theory and Modeling* 4, 241–264 (2000).

[19] I. Celik, I. Yavuz and A. Smirnov, Large-eddy simulations of in-cylinder turbulence for IC engines: A review, *International J. Engine Res.* 2, 119–148 (2001).

[20] A. J. Chandy, D. J. Glaze and S. H. Frankel, Assessment of subgrid-scale mixing models for large eddy simulation using the filtered density function approach, In *Proceedings of Fourth Joint Meeting of the U.S. Sections of the Combustion Institute*, Philadelphia, PA (20–23 March 2005).

[21] F. Gao and E. E. O'Brien, A Large-Eddy Simulation Scheme for Turbulent Reacting Flows, *Phys. Fluids* 5, 1282–1284 (1993).

[22] L. Y. M. Gicquel, P. Givi, F. A. Jaberi and S. B. Pope, Velocity filtered density function for large eddy simulation of turbulent flows, *Phys. Fluids* 14, 1196–1213 (2002).

[23] V. Singh, Study of turbulence-radiation interactions using LES of planar channel flow, Master's thesis, The Pennsylvania State University, Department of Mechanical Engineering, University Park, PA (2005).

[24] S. B. Pope, PDF Methods for Turbulent Reactive Flows, *Progr. Energy Combust. Sci.* 11, 119–192 (1985).

[25] P. A. Libby and F. A. Williams, *Turbulent Reacting Flows*, Academic Press, San Diego (1994).

[26] S. R. Turns, *An Introduction to Combustion: Concepts and Applications* (2nd Edn), McGraw-Hill, (2000).

[27] J. Warnatz, U. Maas and R. W. Dibble, *Combustion*, Springer-Verlag, (2001).

[28] W. Rodi, Progress in Turbulence Modeling for Incompressible Flows, In *Proceedings of the Nineteenth AIAA Aerospace Sciences Meeting*, St. Louis, Missouri (January 1981).

[29] Jones W. P., Models for Turbulent Flows with Variable Density and Combustion, In *Prediction Methods for Turbulent Flows*, Hemisphere Publishing Corp., London (1980).

[30] R. Borghi, Turbulent combustion modeling, *Progr. Energy Combust. Sci.* 14(4), 245–292 (1988).

[31] W. P. Jones and Whitelaw J. H., Calculation Methods for Reacting Turbulent Flows: A Review, *Comb. Flame*, 1–26 (1982).

[32] M. S. Anand, S. B. Pope and H. C. Mongia, PDF calculations for swirling flow, *AIAA Paper, No. 93-0106*, (1993).

[33] K. K. Kuo, *Principles of Combustion*, Wiley Interscience, New York (1986).

[34] P. Givi, Model-Free Simulations of Turbulent Reactive Flows, *Prog. Energy Combust. Sci.* 15, 1–107 (1989).

[35] C. Dopazo and E. E. O'Brien, Functional Formulation of Non-isothermal Turbulent Reactive Flows, *Phys. Fluids* 17, 1968–1975 (1974).

[36] W. Kollmann, The PDF Approach to Turbulent Flow, *Theor. Compt. Fluid Dyn.* 1, 249–285 (1990).

[37] C. Dopazo, Recent developments in PDF methods, In *Turbulent Reacting Flows*, pp. 375–474. Academic Press, (1994).

[38] S. Mazumder, *Numerical Study of Chemically Reactive Turbulent Flows with Radiative Heat Transfer*, PhD thesis, The Pennsylvania State University, University Park, PA, (1997).

[39] S. Mazumder and M. F. Modest, PDF Modeling of Turbulence Radiation Interactions, In *1997 National Heat Transfer Conference, Baltimore, MD*, ASME (1997).

[40] C. Dopazo, Relaxation of initial probability density function in the turbulent convection of scalar fields, *Phys. Fluids* 22, 20–30 (1979).

[41] L. Valino and C. Dopazo, A binomial Langevin model for turbulent mixing, *Physics of Fluids A* 3, 3034 (1991).

[42] S. B. Pope, *Turbulent Flows*, Cambridge University Press, Cambridge (2000).

[43] S. B. Pope and Y. L. Chen, The Velocity-Dissipation Probability Density Function Method for Turbulent Flows, *Phys. Fluids A* 2(8), 1437–1449 (1990).

[44] Y. Z. Zhang and D. C. Haworth, A general mass consistency algorithm for hybrid particle/finite-volume PDF methods, *J. Comp. Phys.* 194, 156–193 (2004).

[45] Y. Z. Zhang, E. H. Kung and D. C. Haworth, A PDF method for multidimensional modeling of HCCI engine combustion: Effects of turbulence/chemistry interactions on ignition timing and emissions, *Proceedings of The Combustion Institute* 30, 2763–2771 (2005).

[46] G. Li, *Investigation of Turbulence–Radiation Interactions By a Hybrid FV/PDF Monte Carlo Method*, PhD thesis, The Pennsylvania State University, University Park, PA, (2002).

[47] J. Janicka, W. Kolbe and W. Kollmann, The Solution of a PDF-Transport Equation for Turbulent Diffusion Flames, In *Proceedings of 1978 Heat Trans. Fluid Mech. Inst., Stanford University*, (1978).

[48] S. Subramaniam and S. B. Pope, A Mixing Model for Turbulent Reactive Flows based on Euclidean Minimum Spanning Trees, *Comb. Flame* 115, 487–514 (1998).

[49] B. Merci, B. Naud and D. Roekaerts, Interaction between chemistry and micromixing modeling in transported PDF simulations of tubulent nonpremixed flames, *Comb. Sci. Tech.* 179(1–2), 153–172 (2007).

[50] T. Vaithiananthan, M. Ulitsky and Collins L. R., Comparison between a spectral and probability density function model for turbulent reacting flows, *Proceedings of the Combustion Institute* 29, 2139–2146 (2002).

[51] P. Jenny, S. B. Pope, M. Muradoglu and D. A. Caughey, A Hybrid Algorithm for the Joint PDF Equation of Turbulent Reactive Flows, *J. Comp. Phys.* 166, 218–252 (2001).

[52] M. Muradoglu, P. Jenny, S. B. Pope and D. A. Caughey, A Consistent Hybrid Finite Volume/Particle Method for the PDF Equations of Turbulent Reactive Flows, *J. Comp. Phys.* 154, 342–371 (1999).

[53] S. V. Subramaniam and D. C. Haworth, A PDF Method for Turbulent Mixing and Combustion on Three-Dimensional Unstructured Deforming Meshes, *Intern'l. J. Engine Research* 1, 171–190 (2000).

[54] M. Muradoglu, S. B. Pope and D.A. Caughey, The hybrid method for the PDF equations of turbulent reactive flows: Consistency conditions and correction algorithm, *J. Comp. Phys.* 172, 841–878 (2001).

[55] J. Xu and S. B. Pope, Assessment of Numerical Accuracy of PDF/Monte Carlo Methods for Turbulent Reacting Flows, *J. Comp. Phys.* 152, 192–230 (1999).

[56] S. B. Pope, On the relationship between stochastic Lagrangian models of turbulence and second-moment closures, *Phys. Fluids* 6, 973–985 (1994).

[57] G. Li and M. F. Modest, Application of composition PDF methods in the investigation of turbulence–radiation interactions, *J. Quant. Spectrosc. Radiat. Transfer* 73(2–5), 461–472 (2002).

[58] S. Subramaniam and D. C. Haworth, A PDF Method for Turbulent Mixing and Combustion on Three-Dimensional Unstructured Deforming Meshes, *International Journal of Engine Research* 1, 171–190 (2000).

[59] V. P. Kabashnikov and G. I. Myasnikova, Thermal Radiation in Turbulent Flows—Temperature and Concentration Fluctuations, *Heat Transfer-Soviet Research* 17(6), 116–125 (1985).

[60] J. W. Hartick, M. Tacke, G. Fruchtel, E. P. Hassel and J. Janicka, Interaction of Turbulence and Radiation in Confined Diffusion Flames, In *Twenty-Sixth Symposium (International) on Combustion*, pp. 75–82, The Combustion Institute (1996).

[61] R. S. Mehta, Modeling of Absorption Coefficient–Intensity Correlations for Optically Thick Eddies in Turbulent Reacting Flows Using Hybrid Finite Volume/PDF Monte Carlo Methods, Master's thesis, The Pennsylvania State University, Department of Mechanical Engineering, University Park, PA (2005).

[62] T. H. Song and R. Viskanta, Interaction of Radiation with Turbulence: Application to a Combustion System, *J. Thermoph. Heat Transfer* 1(1), 56–62 (1987).

[63] W. Krebs, R. Koch, L. Eigenmann and S. Wittig, Effect of Temperature and Concentration Fluctuations on Radiative Heat Transfer in Turbulent Flames, *Proc. Combust. Inst.* 26, 2763–2770 (1996).

[64] S. Mazumder and M. F. Modest, A PDF Approach to Modeling Turbulence–Radiation Interactions in Nonluminous Flames, *Int. J. Heat Mass Transfer* 42, 971–991 (1999).

[65] S. Mazumder and M. F. Modest, Turbulence–Radiation Interactions in Nonreactive Flow of Combustion Gases, *J. Heat Transfer* 121, 726–729 (1999).

[66] G. Li and M. F. Modest, A PDF method to capture sharp gradients in turbulent heat transfer, In *Proceedings of the 2000 National Heat Transfer Conference*, ASME, Pittsburgh, PA (2000).

[67] G. Li and M. F. Modest, A PDF Scheme to Capture Sharp Gradients in Hybrid Finite Volume/PDF Monte Carlo Methods, In *Proceedings of the 2000 IMECE*, ASME, Orlando, FL (2000).

[68] G. Li and M. F. Modest, Importance of Turbulence–Radiation Interactions in Turbulent Diffusion Jet Flames, *J. Heat Transfer* 125, 831–838 (2003).

[69] V. Raman, R. O. Fox and A. D. Harvey, Hybrid finite-volume/transported PDF simulations of a partially premixed methane–air flame, *Comb. Flame* 136, 327–350 (2004).

[70] L. Tessé, F. Dupoirieux, B. Zamuner and J. Taine, Radiative transfer in real gases using reciprocal and forward Monte Carlo methods and a correlated-k approach, *Int. J. Heat Mass Transfer* 45, 2797–2814 (2002).

[71] L. Tessé, F. Dupoirieux and J. Taine, Monte Carlo modeling of radiative transfer in a turbulent sooty flame, *Int. J. Heat Mass Transfer* 47, 555–572 (2004).

[72] B. Zamuner and F. Dupoirieux, Numerical Simulation of Soot Formation in a Turbulent Flame with a Monte-Carlo PDF Approach and Detailed Chemistry, *Comb. Sci. Tech.* 158, 407–438 (2000).

[73] A. Wang and M. F. Modest, Monte Carlo simulation of radiative heat transfer and turbulence interactions in methane/air jet flames, *J. Quant. Spectrosc. Radiat. Transfer* 109, 269–279 (2007).

[74] A. Wang and M. F. Modest, Photon Monte Carlo Simulation for Radiative Transfer in Gaseous Media Represented by Discrete Particle Fields, *J. Heat Transfer* 128(10), 1041–1049 (2006).

[75] L. Tessé, F. Dupoirieux and J. Taine, Monte Carlo modeling of radiative transfer in a turbulent sooty flame, *Int. J. Heat Mass Transfer* 47, 555–572 (2004).

[76] J.-M. Hartmann, R. Levi Di Leon and J. Taine, Line-by-Line and Narrow-Band Statistical Model Calculations for H_2O, *J. Quant. Spectrosc. Radiat. Transfer* 32(2), 119–127 (1984).

[77] L. S. Rothman, C. P. Rinsland, A. Goldman, S. T. Massie, D. P. Edwards, J.-M. Flaud, A. Perrin, C. Camy-Peyret, V. Dana, J.-Y. Mandin, J. Schroeder, A. McCann, R. R. Gamache, R. B. Wattson, K. Yoshino, K. V. Chance, K. W. Jucks, L. R. Brown, V. Nemtchinov and P. Varanasi, The HITRAN Molecular Spectroscopic Database and HAWKS (HITRAN Atmospheric Workstation): 1996 Edition, *J. Quant. Spectrosc. Radiat. Transfer* 60, 665–710 (1998).

[78] L. S. Rothman, C. Camy-Peyret, J.-M. Flaud, R. R. Gamache, A. Goldman, D. Goorvitch, R. L. Hawkins, J. Schroeder, J. E. A. Selby and R. B. Wattson, HITEMP, the High-Temperature Molecular Spectroscopic Database, (2000), available through `http://www.hitran.com`.

[79] S. A. Tashkun, V. I. Perevalov, A. D. Bykov, N. N. Lavrentieva and J.-L. Teffo, Carbon Dioxide Spectroscopic databank (CDSD), available from ftp://ftp.iao.ru/pub/CDSD-1000, (2002).

[80] M. K. Denison and B. W. Webb, The Spectral-Line Weighted-Sum-of-Gray-Gases Model for H_2O/CO_2 Mixtures, *J. Heat Transfer* 117, 788–792 (1995).

[81] A. Y. Snegirev, Statistical modeling of thermal radiation transfer in buoyant turbulent diffusion flames, *Comb. Flame* 136, 51–71 (2004).

[82] P. Rivière, D. Scutaru, A. Soufiani and J. Taine, A New $c - k$ Data Base Suitable from 300 to 2500 K for Spectrally Correlated Radiative Transfer in CO_2–H_2O Transparent Gas Mixtures, In *Tenth International Heat Transfer Conference*, pp. 129–134, Taylor & Francis (1994).

[83] M. F. Modest, Narrow-band and full-spectrum k-distributions for radiative heat transfer—correlated-k vs. scaling approximation, *J. Quant. Spectrosc. Radiat. Transfer* 76(1), 69–83 (2003).

[84] M. F. Modest and H. Zhang, The Full-Spectrum Correlated-k Distribution and its Relationship to the Weighted-Sum-of-Gray-Gases Method, In *Proceedings of the IMECE 2000*, Vol. HTD-366-1, pp. 75–84, ASME, Orlando, FL (2000).

[85] M. F. Modest and H. Zhang, The Full-Spectrum Correlated-k Distribution For Thermal Radiation from Molecular Gas–Particulate Mixtures, *J. Heat Transfer* 124(1), 30–38 (2002).

[86] M. F. Modest and R. J. Riazzi, Assembly of Full-Spectrum k-Distributions from a Narrow-Band Database; Effects of Mixing Gases, Gases and Nongray Absorbing Particles, and Mixtures with Nongray Scatterers in Nongray Enclosures, *J. Quant. Spectrosc. Radiat. Transfer* 90(2), 169–189 (2004).

[87] G. Pal and M. F. Modest, Multi-group, Multi-scale Full Spectrum k-Distribtuions, Proceedings of CHT-08, ICHMT International Symposium on Advances in Computational Heat Transfer,May 11–16, 2008, Marrakech, Morocco, (2008).

[88] A. Wang and M. F. Modest, High-accuracy, compact database of narrow-band k-distributions for water vapor and carbon dioxide, *J. Quant. Spectrosc. Radiat. Transfer* 93, 245–261 (2005).

[89] H. Chang and T. T. Charalampopoulos, Determination of the wavelength dependence of refractive indices of flame soot, *Proceedings of the Royal Society (London) A* 430(1880), 577–591 (1990).

[90] P. J. Coelho, O. J. Teerling and D. Roekaerts, Spectral radiative effects and turbulence/radiation interaction in a non-luminous turbulent jet diffusion flame, *Comb. Flame* 133, 75–91 (2003).

[91] P. J. Coelho, Detailed numerical simulation of radiative transfer in a nonluminous turbulent jet diffusion flame, *Comb. Flame* 136, 481–492 (2004).

[92] Liangyu Wang, *Detailed Chemistry, Soot and Radiation Calculations in Turbulent Reactive Flows*, PhD thesis, The Pennsylvania State University, University Park, PA, (2002).

[93] J. Yang and M. F. Modest, High-Order *P-N* Approximation for Radiative Transfer in Arbitrary Geometries, In *Proceedings of Eurotherm Seminar 78*, Elsevier, Poitiers, France (April 2006).

[94] J. Yang and M. F. Modest, Elliptic PDE Formulation of High-Order *P-N* Approximations for Radiative Transfer, *Int. J. Heat Mass Transfer*, (April 2006), submitted for publication.

[95] K. D. Deshmukh, M. F. Modest and D. C. Haworth, Application of High Order P_N to DNS, Proceedings of CHT-08, ICHMT International Symposium on Advances in Computational Heat Transfer,May 11–16, 2008, Marrakech, Morocco, (2008).

[96] A. Wang, *Investigation of Turbulence–Radiation Interactions in Turbulent Flames Using a Hybrid Finite Volume/Monte Carlo Approach*, PhD thesis, The Pennsylvania State University, (2007).

[97] M. F. Modest, The Monte Carlo Method Applied to Gases with Spectral Line Structure, *Numer. Heat Transfer B* 22(3), 273–284 (1992).

[98] J. T. Farmer and J. R. Howell, Monte Carlo Prediction of Radiative Heat Transfer in Inhomogeneous, Anisotropic, Nongray Media, *J. Thermoph. Heat Transfer* 8(1), 133–139 (1994).

[99] H. Bockhorn, *Soot Formation in Combustion*, Springer Verlag, New York (1994).

[100] R. J. Santoro, T. T. Yeh, J. J. Horvath and H. G. Semerjian, The Transport and Growth of Soot Particles in Laminar Diffusion Flames, *Combust. Sci. Tech.* 53, 89–115 (1987).

[101] R. J. Santoro and H. G. Semerjian, Soot Formation in Diffusion Flames; Flow Rate, Fuel Species and Temperature Effects, *Proc. Comb. Inst.* 20, 997–1010 (1984).

[102] B. S. Haynes and H. G. Wagner, Soot Formation, *Progr. Energy Combust. Sci.* 7, 229–273 (1981).

[103] H. F. Calcote, Mechanism of Soot Nucleation in Flames - A Critical Review, *Comb. Flame* 42(3), 215–242 (1981).

[104] M. Frenklach and H. Wang, Detailed Mechanism and Modeling of Soot Particle Formation, In *Soot Formation in Combustion: Mechanisms and Models* (Edited by H. Bockhorn), Springer-Verlag, New York (1994).

[105] H. Wang and M. Frenklach, A Detailed Kinetic Modeling Study of Aromatics Formation in Laminar Premixed Acetylene and Ethylene Flames, *Comb. Flame* 110, 173–221 (1997).

[106] M. B. Colket and R. J. Hall, Successes and Uncertainties in Modeling Soot Formation in Laminar, Premixed Flames, In *Soot Formation in Combustion: Mechanisms and Models* (Edited by H. Bockhorn), Springer-Verlag, New York (1994).

[107] M. Frenklach and H. Wang, Detailed Modeling of Soot Particle Nucleation and Growth, *Proc. Combust. Inst.* 23, 1559–1566 (1991).

[108] M. Frenklach, Reaction mechanism of soot formation in flames, *Phys. Chem. Chem. Phys.* 4, 2028–2037 (2002).

[109] N. A. Fuchs, *The mechanics of aerosols*, Dover, Mineola, NY (1989).

[110] J. H. Seinfeld and S. N. Pandis, *Atmospheric chemistry and physics. From air pollution to climate change*, Wiley, New York, NY (1998).

[111] P. Mitchell and M. Frenklach, Particle aggregation with simultaneous surface growth, *Physical Review E* 67, (2003).

[112] S. J. Harris and A. M. Weiner, Chemical Kinetics of Soot Particle Growth, *Ann. Rev. Phys. Chem* 36, 31–52 (1985).

[113] P. B. Sunderland, Ü. Ö. Köylü and G. M. Faeith, Soot Formation in Weakly Buoyant Acetylene-Fueled Laminar Jet Diffusion Flames, *Comb. Flame* 100, 310–322 (1995).

[114] R. Puri, T. F. Richardson, R. J. Santoro and R. A. Dobbins, Aerosol Dynamic Processes of Soot Aggregates in a Laminar Ethene Diffusion Flame, *Comb. Flame* 92(3), 320–333 (1993).

[115] D. F. Kronholm and H. B¿ Howard, Analysis of soot surface growth pathways using published plug-flow reactor data with new particle size distribution measurements and published premixed flame data, *Proc. Combust. Inst.* 28, 2555–2561 (2000).

[116] F. Xu, P. B. Sunderland and G. M. Faeth, Soot formation in laminar premixed ethylene/air flames at atmospheric pressure, *Comb. Flame* 108(4), 471–493 (1997).

[117] F. Xu, K. C. Lin and G. M. Faeth, Soot formation in laminar premixed methane/oxygen flames at atmospheric pressure, *Comb. Flame* 115(1–2), 195–209 (1998).

[118] F. Xu and G. M. Faeth, Soot Formation in Laminar Acetylene/air Diffusion Flames at Atmospheric Pressure, *Comb. Flame* 125(1-2), 804–819 (2001).

[119] H. Wang, D. X. Du, C. J. Sung and C. K. Law, Experiments and Numerical Simulation on Soot Formation in Opposed-jet Ethylene Diffusion Flames, *Proc. Combust. Inst.* 26, 2359–2368 (1996).

[120] K. G. Neoh, J. B. Howard and A. F. Sarofim, In *Particulate Carbon: Formation During Combustion* (Edited by Siegla D.C. and G.W. Smith), p. 261. Plenum, New York (1981).

[121] I. M. Kennedy, W. Kollmann and J. Y. Chen, A Model for Soot Formation in Laminar Diffusion Flame, *Comb. Flame* 81(1), 73–85 (1990).

[122] K. M. Leung, R. P. Lindstedt and W. P. Jones, A Simplified Reaction Mechanism for Soot Formation in Nonpremixed Flames, *Comb. Flame* 87, 289–305 (1991).

[123] M. Frenklach, Mehod of Moments With Interpolative Closure, *Chemical Engineering Science* 57, 2229–2239 (2002).

[124] M. Balthasar and M. Kraft, A stochastic approach to calculate the particle size distrbution function of soot particles in laminar premixed flames, *Comb. Flame* 133, 289–298 (2003).

[125] M. Frenklach and S. J. Harris, Aerosol Dynamics Modeling Using the Method of Moments, *Journal of Colloid and Interface Science* 118(1), 252–261 (1987).

[126] M. Balthasar and M. Frenklach, Detailed kinetic soot modeling of soot aggregate formation in laminar premixed flames, *Comb. Flame* 140, 130–145 (2005).

[127] A. Kazakov and M. Frenklach, Dynamic Modeling of Soot Particle Coagulation and Aggregation: Implementation With the Method of Moments and Application to High-Pressure Laminar Premixed Flames, *Comb. Flame* 114, 484–501 (1998).

[128] Hai Wang, *Detailed Kinetic Modeling of Soot Particle Formation in Laminar Premixed Hydrocarbon Flames*, PhD thesis, The Pennsylvania State University, University Park, PA, (1992).

[129] N. Brown, K. Revzan and M. Frenklach, Detailed Kinetic Modelin of Soot Formation in Ethylene/Air Mixtures Reacting in a Perfectly Stirred Reactor, *Proc. Combust. Inst.* 27, 1573–1580 (1998).

[130] K. L. Revzan, N. J. Brown and M. Frenklach, Code for method of moments, http://www.me.berkeley.edu/soot/codes/codes.html, (2002).

[131] P. Lindstedt, Simplified Soot Nucleation and Surface Growth Steps for Non-Premixed Flames, In *Soot Formation in Combustion: Mechanisms and Models* (Edited by H. Bockhorn), Springer-Verlag, New York (1994).

[132] R. P. Lindstedt and S. A. Louloudi, Joint-scalar transported PDF modeling of soot formation and oxidation, *Proc. Combust. Inst.* 30, 775–783 (2005).

[133] C. M. Sorensen, Light Scattering by Fractal Aggregates: A Review, *Aero. Sci. Tech.* 35, 648–687 (2001).

[134] G. M. Faeth and Ü. Ö. Köylü, Soot Morphology and Optical Properties in Non-premixed Turbulent Flame Environments, *Comb. Sci. Tech.* 108, 207–229 (1995).

[135] K. C. Smyth and C. R. Shaddix, The Elusive History of $\tilde{m} = 1.57 - 0.56i$ for the Refractive Index of Soot, *Comb. Flame* 107, 314–320 (1996).

[136] H. Chang and T. T. Charalampopulos, Determination of Wavelength Dependence of Refractive-Indexes of Flame Soot, Vol. 430, pp. 577–591. Proceedings of the Royal Society of London Series A- Mathematical Physical and Engineering Sciences, (1990).

[137] H. Pitsch, E. Riesmeier and N. Peters, Unsteady Flamelet Modeling of Soot Formation in Turbulent Diffusion Flames, *Comb. Sci. Tech.* 158, 389–406 (2000).

[138] F. Zheng, Thermophoresis of spherical and non-spherical particles: a review of theories and experiments, *Advances in Colloid and Interface Science* 97, 255–278 (2002).

[139] M. Balthasar, F. Mauss, A. Knobel and M. Kraft, Detailed Modeling of Soot Formation in a Partially Stirred Plug Flow Reactor, *Comb. Flame* 128, 395–409 (2002).

[140] Z. Qin, V. V. Lissianski, H. Yang, W. C. Gardiner, S. G. Davis and H. Wang, Combustion Chemistry of Propane: A Case Study of Detailed Reaction Mechanism Optimization, *Proc. Combust. Inst.* 28, 1663–1669 (2000).

[141] C. K. Law, Comprehensive Description of Chemistry in Combustion Modeling, *Comb. Sci. Tech.* 177, 845–870 (2005).

[142] Online Resource, http://garfield.chem.elte.hu/Combustion/mechmod.htm.

[143] Online Resource, http://www-mae.ucsd.edu/ combustion/cermech/.

[144] S. C. Li, B. Varatharajan and F. A. Williams, The chemistry of ethylene ignition for application in pulse detonation engines, *AIAA paper 2000-3475*, (2000).

[145] H. Richter and J. B. Howard, Formation of polycyclic aromatic hydrocarbons and their growth to soot – a review of chemical reaction pathways, *Progr. Energy Combust. Sci.* 26, 565–608 (2000).

[146] R. J. Kee, J. F. Grcar, M.D. Smooke and J. A. Miller, A Fortran Program for Modeling Steady Laminar One-dimensional Premixed Flames, Technical Report SAND85-8240, Sandia National Laboratories, (1985).

[147] A. E. Lutz, R. J. Kee, J. F. Grcar and F. M. Rupley, OPPDIF: A Fortran Program for Computing Opposed-Flow Diffusion Flames, Technical Report SAND96-8243, Sandia National Laboratories, (1996).

[148] R. J. Kee, G. Dixon-Lewis, J. Warnatz, M. E. Coltrin and J. A. Miller, A Computer Code Package For Evaluation of Gas-Phase, Multicomponent Transport Properties, Technical Report SAND86-8246, Sandia National Laboratory, (1986).

[149] R. J. Kee, F. M. Rupley and J. A. Miller, CHEMKIN-II: A Fortran Chemical Kinetics Package for the Analysis of Gas-Phase Chemical Kinetics, Technical Report SAND89-8009B, Sandia National Laboratories, (1989).

[150] B. Zhao, Z. Yang, J. Wang, M. V. Johnston and H. Wang, Analysis of Soot Nanoparticles in a Laminar Premixed Ethylene Flame by Scanning Mobility Particle Sizer, *Aero. Sci. Tech.* (37), 611–620 (2003).

[151] J. Y. Hwang and S. H. Chung, Growth of Soot Particles in Counterflow Diffusion Flames, *Comb. Flame* 125, 752–762 (2001).

[152] J. Singh, R. I. A. Patterson, M. Kraft and H. Wang, Numerical simulation and sensitivity analysis of detailed particle size distribution function in laminar premixed ethylene flames, *Comb. Flame* (145), 117–127 (2006).

[153] Online Resource, http://www.ca.sandia.gov/TNF/abstract.html.

[154] A. C. Eckberth, *Laser Diagnostics for Combustion Temperature and Species*, Turnbridge Wells, Kent and Cambridge, Massachusetts (1988).

[155] A. Coppalle and D. Joyeux, Temperature and Soot Volume Fraction in Turbulent Diffusion Flames: Measurements of Mean and Fluctuating Values, *Comb. Flame* 96, 275–285 (1994).

[156] J. H. Kent and D. Honnery, Modeling sooting turbulent jet flames using an extended flamelet technique, *Comb. Sci. Tech.* 54, 383–397 (1987).

[157] N. E. Endrud, Soot, Radiation and Pollutant Emissions in Oxygen-Enhanced Turbulent Jet Flames, Master's thesis, The Pennsylvania State University, University Park, PA (2000).

[158] V. Saxena and S. B. Pope, PDF Simulations of Turbulent Combustion Incorporating Detailed Chemistry, *Comb. Flame* 117, 340–350 (1999).

[159] R. S. Mehta, D. C. Haworth and M. F. Modest, An Assessment of Gas-Phase Reaction Mechanisms and Soot Models for Laminar Atmospheric-Pressure Ethylene-Air Flames, *Proc. Combust. Inst.* 32, (2008), To appear.

[160] R. S. Mehta, A. Wang, M. F. Modest and D. C. Haworth, Modeling of a Turbulent Ethylene/Air Flame Using Hybrid Finite Volume/Monte Carlo Methods, Proceedings of CHT-08, ICHMT International Symposium on Advances in Computational Heat Transfer,May 11–16, 2008, Marrakech, Morocco, (2008).

[161] M. Kalal and K. A. Nugent, Abel Inversion Using Fast Fourier Transforms, *Apptl. Opt.* 27, 1956–1959 (1988).

[162] R. Said, A. Garo and R. Borghi, *Comb. Flame* 108, 71–86 (1997).

[163] R. Borghi, Turbulent Combustion Modelling, *Progr. Energy Combust. Sci.* 14, 245–292 (1988).

[164] L. Wang, N. E. Endrud, S. R. Turns, M. D. D'Agostini and A. G. Slavejkov, A Study of the Influence of Oxygen Index on Soot, Radiation, and Emission Characteristics of Turbulent Jet Flames, *Comb. Sci. Tech.* 178(8), 45–72 (2002).

[165] R. V. Bandaru, *Experimental Studies of the Emission Characteristics of Non-premixed Gas-Air Flames of Various Configurations.*, PhD thesis, The Pennsylvania State University, University Park, PA, (2000).

[166] S. C. Lee and C. L. Tien, Optical Constants of Soot in Hydrocarbon Flames, *Proc. Combust. Inst.* 18, 1159–1166 (1989).

[167] G. Cerri, V. Michelassi, S. Monacchia and S. Pica, Kinetic combustion neural modeling integrated into computational fluid dynamics, *Journal of Power and Energy* 217(2), 185–192 (2003).

[168] N. Sundararajan, P. Saratchandran and L. Y. Wei, *Radial Basis Function Neural Networks with Sequential Learning: MRAN and its applications*, World Scientific, (1999).

[169] S. E. Pratsinis, Simultaneous nucleation, condensation, and coagulation in aerosol reactors, *Journal of Colloid and Interface Science* 124, 416–427 (1988).

Vita

Ranjan S. Mehta

Ranjan Mehta was born in the city of Pune, India on February 27^{th} 1979. He attended the University of Pune and received his Bachelor of Engineering in Mechanical Engineering in 2000. He worked in a software development firm, Cognizant Technology Solutions (NASDAQ: CTSH) as a Programmer Analyst. In August 2002, he joined The Pennsylvania State University as a graduate research assistant in the Department of Mechanical and Nuclear Engineering. He also served as a graduate teaching fellow in Spring 2007. During his years at Pennstate, he worked on numerical modeling of combustion, soot formation and radiation. He also developed a keen interest in stochastic modeling, in general. He then joined CFD Research Corporation (CFDRC) as a research engineer in the combustion division.